REPORT DOCUMENTATION PAGE

1. REPORT DATE *(DD-MM-YYYY)* 5/31/2012	2. REPORT TYPE FINAL	3. DATES COVERED *(From - To)* 2/1/2009-5/31/2012

4. TITLE AND SUBTITLE Optimal constellation design for maximum continuous coverage of targets against a space background		5a. CONTRACT NUMBER
		5b. GRANT NUMBER FA9550-09-1-0227
		5c. PROGRAM ELEMENT NUMBER
6. AUTHOR(S) Dr. Belinda Marchand, and Andrew Takano, PhD Student		5d. PROJECT NUMBER
		5e. TASK NUMBER
		5f. WORK UNIT NUMBER

7. PERFORMING ORGANIZATION NAME(S) AND ADDRESS(ES) Dr. Belinda Marchand The University of Texas at Austin 210 E. 24th St., Austin, TX 78712	8. PERFORMING ORGANIZATION REPORT NUMBER

9. SPONSORING / MONITORING AGENCY NAME(S) AND ADDRESS(ES) Dr. KentL.Miller Program Manager,AFOSR/NE 875 N. Randolph St., Suite 3112 Arlington, VA 22203	10. SPONSOR/MONITOR'S ACRONYM(S)
	11. SPONSOR/MONITOR'S REPORT NUMBER(S) AFRL-OSR-VA-TR-2012-0511

12. DISTRIBUTION / AVAILABILITY STATEMENT

Distribution A.

13. SUPPLEMENTARY NOTES

14. ABSTRACT

Modern space situational awareness is focused on the detection, tracking, identification, and characterization of passive and active resident space objects. In the past, this process relied primarily on ground-based sensors. However, difficulties arise when smaller, more distant, or otherwise dim objects are considered. Space based sensors may help alleviate some of these difficulties. The work funded under this award has focused primarily on optimal design for a constellation of space based sensors to support the goals of space situational awareness. To that end, the work leverages concepts from computer graphics to analyze sensor coverage strictly from a numerical perspective, enabling a unique design approach that is adaptable to any sensor network for situational awareness applications.

15. SUBJECT TERMS

space situational awareness, constellation design, optimization, polygon clipping

16. SECURITY CLASSIFICATION OF:			17. LIMITATION OF ABSTRACT	18. NUMBER OF PAGES	19a. NAME OF RESPONSIBLE PERSON Belinda Marchand
a. REPORT U	b. ABSTRACT U	c. THIS PAGE U	SAR	80	19b. TELEPHONE NUMBER *(include area code)* 512-627-4785

Final Report for Grant #FA9550-09-1-0227
Optimal constellation design for maximum continuous coverage of targets against a space background.

PI: Dr. Belinda Marchand
The University of Texas at Austin

May 31st, 2012

Abstract

Modern space situational awareness is focused on the detection, tracking, identification, and characterization of passive and active resident space objects. In the past, this process relied primarily on ground-based sensors. However, difficulties arise when smaller, more distant, or otherwise dim objects are considered. Space based sensors may help alleviate some of these difficulties. The work funded under this award has focused primarily on optimal design for a constellation of space based sensors to support the goals of space situational awareness. To that end, the work leverages concepts from computer graphics to analyze sensor coverage strictly from a numerical perspective, enabling a unique design approach that is adaptable to any sensor network for situational awareness applications.

1 Executive Summary

As near-Earth space becomes increasingly crowded with spacecraft and debris, the need for improved space situational awareness (SSA) has become paramount. Modern SSA is concerned with the detection, tracking, identification, and characterization (DTI&C) of passive (e.g. debris) and active (i.e. maneuverable) resident space objects (RSOs), at all altitudes, with known accuracy and precision. Modern advances in technology miniaturization, and the growing capabilities of nano- and pico-satellite platforms, have raised many new and exciting technical challenges in this area. Contemporary ground-based systems, such as the space surveillance network (SSN), are oftentimes unable to resolve small, distant, or otherwise faint objects. In these instances, space-based sensors may be beneficial to augment existing SSA capabilities for enhanced DTI&C.

In this study SSA goals are primarily accomplished through a constellation of space based sensors, though the approach also allows for the inclusion of ground based sensors.[3] The constellation is designed to provide optimal above-the-horizon (ATH) coverage. This is fundamentally different from more classical optimal constellation coverage problems, which focus on optimizing coverage of ground-based targets. The latter is typically referred to as the below-the-horizon (BTH) coverage problem. The 'horizon,' in this case, is defined as a line drawn from the satellite and tangent to the surface of a fictitious sphere, one concentric with the Earth but of equal or greater radius. This reference tangent height sphere is simply a convenient construct that may be used, for instance, to represent the bounds of the atmosphere. From a three-dimensional perspective, this line traces a cone that is tangent to this reference sphere. RSO's that exist above this cone are said to be viewed against a space background. Thus, a sensor concerned with such targets is said to provide ATH coverage.

Aside from being primarily interested in RSO's that exist above the horizon, the present study is further interested in objects that evolve within some prescribed three-dimensional region of space that exists above the horizon. The goal of this effort is to identify a generalized numerical process by which to accomplish the optimal design of a constellation of orbiting sensors that meet a specific collective objective for ATH coverage. This includes consideration of non-coplanar elliptical orbits, arbitrary sensor region's of regard, and dynamical effects. The modeling approach selected considers each sensor's region of regard and any imposed visibility constraints as time varying and dynamic surfaces. Thus, the coverage provided by the constellation

1

can be thought of as a time-varying volume, which is subsequently defined as the cost-index for an optimization process. The calculation of this time-varying volume of coverage is accomplished by performing a series of boolean operations between the reference surfaces at each time step during the simulation.

As an initial step, the first year of this award focused on investigating the preliminary aspects of the simpler planar constellation design problem. A two-pronged approach was selected, one focusing on a strictly numerical approach, and another focusing on devising a closed form expression for constellation coverage that could be used in an optimal constellation design process. Investigating possible numerical techniques initially revealed polygon clipping algorithms as a suitable starting point. Relevant numerical methods were surveyed, studied, evaluated, implemented, and validated against publicly available analytical examples for the single satellite ATH coverage problem. The analytical approach focused on investigating the mathematical preliminaries involved in a purely geometric approach.

In the second year of this effort, the ATH coverage provided by planar constellations was investigated in depth from both the numerical and analytical perspectives. The analytical approach focused on the mathematical aspects involved in addressing coverage multiplicities.[1,2] The numerical approach focused on the development of a numerical process, based on polygon clipping techniques, to numerically analyze planar constellations for ATH coverage of any desired multiplicity (i.e. number of satellites that can observe a given region simultaneously).[3] The numerical approach uses sequences of Boolean operations to determine the multiple overlap of polygons representing the in-plane sensor coverage regions of each satellite and the target region. The advantage of restricting the investigation, at least initially, to planar constellations of satellites sensing in regions symmetric across the orbit plane is that the in-plane ATH coverage region is proportional to volumetric ATH coverage. Thus, by addressing the 2D problem one indirectly addresses the 3D problem as well. The numerical ATH coverage algorithm was applied to several example design constellation problems using a Non-Linear Programming (NLP) solver to illustrate how it may be used in a constellation design process.

The final year of this award initially focused on closing out the planar analysis to begin the transition to the full three-dimensional problem. During that time, the analytical constellation analysis methods[2] devised were successfully employed in validating the numerical process. To further demonstrate the integration of the numerical coverage calculation with an on-line optimization process, a Mixed Integer Non-Linear Programming (MINLP) algorithm was applied to several example constellation design problems, expanding the types of planar constellation optimization problems that may be addressed.[4]

As implemented, extensions to the three-dimensional case entail discretizing volumes representing coverage and target regions into a prescribed number of planar cross-sections of uniform separation. The coverage area within each of the planar cross-sections is evaluated using the previously developed planar analysis algorithm, and is subsequently multiplied by the cross-section plane separation distance. This approximates the volume in each 'layer,' that is summed with the volume of every other layer of a desired coverage multiplicity to approximate the coverage volume. This necessitates a method to generate the cross-sections of the coverage volumes, which is straightforward for the omni-directional sensor profile case. This new approach is applied to several example problems demonstrating volumetric ATH coverage evaluation of constellations of non-coplanar omni-directionally sensing satellites. Since the results of all related initial investigations, during the first two years of this award, have already been published in conference articles, graduate theses, or are pending submission to specific archival journals, the present report offers only a relevant summary of those activities but otherwise focuses, in later sections, to the details of the three-dimensional extension.

2 Accomplishments/New Findings

All optimization processes require that a cost index or performance metric be pre-defined. Typically, such metrics are defined as exact or closed form expressions, an element that is certainly required in any numerical solution process. That is, perhaps, the most difficult aspect of the problem investigated during the course of this study. The results of this work led to the design of a numerical process that allows for the coverage volume provided by a constellation to be systematically computed numerically. The process treats the region of regard of each satellite, the region of interest, and the visibility constraints as a series of surfaces. The coverage volume is identified through a series of boolean operations between the reference surfaces in the constellation. The methodology is integrated with various optimization methods to demonstrate the

integrated process by which the optimal orbital design is accomplished. The innovation, in this case, is not in the optimization process itself. Rather, it is in generalized numerical process designed to address the calculation of the cost index.

The results of this work can be applied in many contexts, from constellation design to close-proximity operations. Thus, far, the results of this work have been published in two conference papers, two MS theses. Two journal articles are currently in preparation for submission to the AIAA Journal of Spacecraft and Rockets. The grant also partially funded the initial year of a follow-on PhD level research. The publications previously listed are summarized below:

- A.T. Takano and B.G. Marchand, "Optimal Constellation Design for Space Based Situational Awareness Applications," AAS/AIAA Astrodynamics Specialists Conference, Girdwood, AK, August 2011. Paper No. AAS11-543

- A.D. Biria and B.G. Marchand, "Constellation Design for Space-Based Situational Awareness Applications: An Analytical Approach," 2011 AAS/AIAA Astrodynamics Specialists Conference, Girdwood, AK, August, 2011. Paper No. AAS11-538.

- Numerical Analysis and Design of Satellite Constellations for Above the Horizon Coverage, Andrew Takano, MS Thesis, Advisor: Dr. Belinda Marchand, December 2010.

- Analytical Approach to the Design of Optimal Satellite Constellations for Space-Based Space Situational Awareness, MS Thesis, Advisor: Dr.Belinda Marchand, December 2011.

The numerical methodology devised has been validated with an analytical approach,[1,2] also devised during this investigation under a simplified set of assumptions. The analytical approach, however, is only applicable to the case of planar constellations, where satellites are collocated along the same circular orbit. The level of complexity associated with the general three-dimensional case, however, is best addressed by the numerical process devised during this study. The numerical approach has been successfully demonstrated in the solution of a MINLP optimization problem in the planar case, where the goal was to determine the optimal number of satellites in the constellation. Also, the numerical process has been demonstrated in a volumetric coverage example for non-coplanar elliptical orbits of non-collocated satellites. At the time of the conclusion of this grant, only omni-directional sensors could be considered in the full three-dimensional case. However, non-omnidirectional sensors were successfully addressed in the two-dimensional case during the first two years of this award. Extending the generalized numerical process to accommodate non-omnidirectional sensors in the three-dimensional case, as well as relative attitude, and other complexities, is a subject that requires further study. Another aspect that requires further study is the numerical efficiency of the overall process. A parallelized structure that leverages GPU's is envisioned as a possible follow-up path that would allow for a more computationally efficient process that could effectively address these added complexities.

3 Project Background

The problem of interest in this investigation pertains to optimal sensor coverage of targets against a space background as provided by a generalized network of orbiting sensor platforms. As a whole, the constellation offers a dynamic heterogeneous network of sensors, each contributing a unique set of capabilities. A candidate optimal design process may seek to optimize over a set of sensor specific parameters, a set of orbital parameters, or both. In this work, the cost metric employed is the overall coverage provided by the constellation within the region of interest. In the modeling approach selected, the sensor coverage, the region of interest, and all related visibility constraints are modeled as dynamically evolving three-dimensional surfaces.

Earlier studies, by Marchand and Kobel,[5] considered a simplified version of this problem. Specifically, for a single satellite, their goal is to maximize sensor visibility of targets against a space background when the region of interest is bounded between an upper and lower target altitude. The results of this study are critical to the present investigation because they establish a meaningful and easily verifiable baseline for comparison.

The goal of this effort was to devise a generalized numerical approach that would enable the optimal design and analysis of constellations aimed at providing some measure of above-the-horizon coverage. This process should allow for consideration of heterogeneous sensors arbitrarily distributed among a series of non-coplanar elliptical orbits. Naturally, this is a very broad specification that adds an immense degree of complexity to the problem. Attempting to identify a closed form solution under these circumstances is simply not feasible. This motivates the numerical approach proposed.

In implementing the numerical approach, it is assumed that the region of regard of any given sensor in the network can be represented as an arbitrary three-dimensional sensor volumetric mesh (SVM). One advantage of this approach is that the user need not have any a priori knowledge of the actual sensor hardware. Consider, then, that each satellite in a constellation contributes at least one SVM to the network. Furthermore, the attitude of each satellite in the constellation may not necessarily be fixed in relation to the reference frame of interest. Thus, the SVM is possibly both translating and rotating in relation to the region of interest. Subsequently, as a given satellite orbits along its path, its SVM may or may not overlap with the ATH region of interest. Determining the collective coverage provided by the constellation at any given instant of time, then, is reduced to the following questions:

- Which of the satellites in the constellation are passing through or are near the region of interest at that time?

- Of those satellites, how many SVM's are properly positioned and oriented so as to intersect the region of interest?

- What is the volume of the intersection of each SVM with the region of interest?

- What is the combined volume provided by the union of these SVM intersections with the region of interest?

- What is the overlap volume (if any) between neighboring SVM's within the region of interest?

- Is the entire region of interest covered by these satellites? or are there gaps in coverage?

- If gaps are present, how can the constellation parameters, or the attitude of the vehicles, be adjusted such that coverage is maximized?

These questions are all addressed at each instant of time during a simulation or optimization process since the SVM's of each satellite are dynamically evolving in position and attitude. Optimizing the constellation, then, may involve the identification of orbital parameters that maximize the coverage of that area over time. Alternatively, it may require that one determine the minimum number of satellites required, and their orbital characteristics, to achieve the coverage requirements of that region.

To demonstrate the above process, a generalized algorithm for numerically estimating the coverage provided by a constellation was formulated and validated. Since analytical results are only available in the

simplified two-dimensional case, the validation was restricted to those examples before proceeding to incorporate three-dimensional extensions of the work. The validation was based on the results published by Marchand and Kobel[5] and Marchand and Biria.[2] These earlier studies focused on identifying analytical expressions, based on geometrical arguments, for the coverage area as a function of altitude. The region of interest was bounded by an upper and lower target altitudes. Strictly to introduce the general notation employed in this report, Figure 1 illustrates a cross-sectional view of the single satellite dual-altitude band ATH coverage problem.[5] In this figure, the upper and lower target altitude shells are labeled UTAS and LTAS, respectively. The satellite is identified as point S. The horizon is defined relative to the tangent height shell, labeled THS. Both of these earlier investigations specifically focused on omnidirectional sensors. This is represented in Figure 1 as a circular cross section centered at the satellite. The intersections of the tangent lines and the sensor range are all labeled on the figure as well. The regions shaded in yellow represent the ATH region covered by the satellite at its current altitude, and that area is a piece-wise differentiable function of the satellite altitude.[5] Of course, in the generalized case, where the sensors are not omni-directional and the satellites in the constellation are unevenly distributed among multiple non-coplanar orbits, an analytical solution is not available. This motivates the numerical approach that is the focus of this effort.
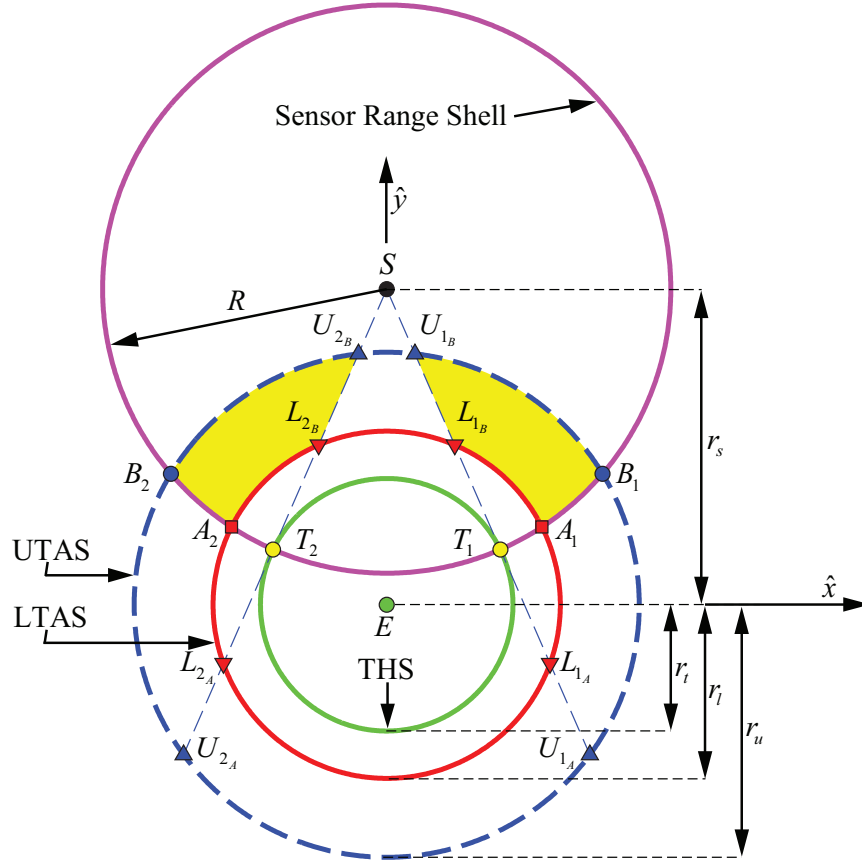

Figure 1: Dual-Altitude Band Above-the-Horizon Problem

4 Planar Constellation Analysis

During the initial phase of this effort, a generalized numerical approach is devised for the calculation of ATH coverage with any desired level of coverage multiplicity.[3] The approach described involves discretization (into polygons) of in-plane satellite coverage regions and regions of interest (assumed to be a dual-altitude band shell bounded above and below by prescribed altitudes). The interactions between these polygons are analyzed by performing different sequences of polygon clipping operations (the computational method used to perform Boolean operations between coplanar polygons), yielding a result polygon that represents the region exhibiting the desired coverage multiplicity bounded by the region of interest. When the enclosed area of this result polygon is computed, it provides an effective measure of in-plane ATH coverage for a given constellation configuration.

The necessary sequences of polygon clipping operations for this analysis are first developed using set notation with a focus on efficiency by avoiding unnecessary polygon clipping operations. These efficient ATH coverage algorithms are then implemented using several different polygon clipping implementations which are compared by their performance. The error introduced by approximating curvilinear regions with finite-resolution polygons is extensively analyzed, and relationships guiding appropriate polygon resolution selection for a desired accuracy are developed.

Several example problems are then solved that illustrate how the numerical ATH coverage algorithms can be incorporated into a satellite constellation design problem. Using a parameter optimization code, the coverage algorithms are first used as objective functions to maximize ATH coverage, then as constraints requiring a target ATH coverage amount be achieved. Simple though they may be, these examples demonstrate the utility of the numerical ATH coverage algorithms in the design of constellation configurations for ATH coverage.

It is worth emphasizing the generality this methodology allows in the analysis of ATH coverage. First, the sensor cross-sections can be of any shape, and can even be unique to each satellite in a constellation. Secondly, the analysis can be used in both time-invariant and time-varying analyses – the only two time-varying parameters necessary are the locations and in-plane attitudes of each satellite at a given time. Lastly, although the study only considers the dual-altitude band shell as the region of interest, it is possible to analyze coverage in regions of interest that are of any desired planar form. For instance, the region of interest could be fixed above a certain location on the central body, i.e. to analyze for ATH coverage specifically above a prescribed geographic region.

A basic example of planar sensor region and region of interest discretization is presented in Section 4.1. Following that, set notation expressions defining the sequences of Boolean operations are developed in Sections 4.2, 4.3, and 4.4. These methods determine regions of single, double, and arbitrarily defined multiplicity of overlap among the sensor regions within the region of interest.

4.1 Discretization of Sensor Regions and Region of Interest

Omni-directional satellite sensor profiles are the simplest possible scenario, and are a straightforward assumption to implement in the planar case. Each satellite is assumed to have sensor visibility within a prescribed radius. However, the sensors are also assumed to only be capable of observing targets that are against a space background from the perspective of the satellite. Thus, any portion of the sensor region in the direction of the Earth must be omitted from consideration (it is a blind spot). The resulting effective ATH coverage region (RS_E) provided by a single satellite is shown in Figure 2a. The omni-directional sensor assumption is not necessary to analyze problems using the methods developed in this study.[3] It does, however, allow for a significantly more straightforward presentation, and is consequently maintained in the current discussion.

The target region, or region of interest (AS), in the current discussion is assumed to be a dual-altitude band region, as shown in Figure 2b. Lower and upper bounds in altitude are prescribed that define the range of altitudes where ATH coverage is of interest. As in the case of the assumed omni-directional satellite sensor profiles, this assumption is not due to a limitation of the methods developed in this study, but is selected to simplify the present discussion. The region of interest can be of any planar form, although the time invariance of the problem is lost in the general case.

Without loss of generality, the assumed forms of RS_E and AS shown in Figure 2 are used to illustrate the coverage expressions developed in Sections 4.2, 4.3, and 4.4.

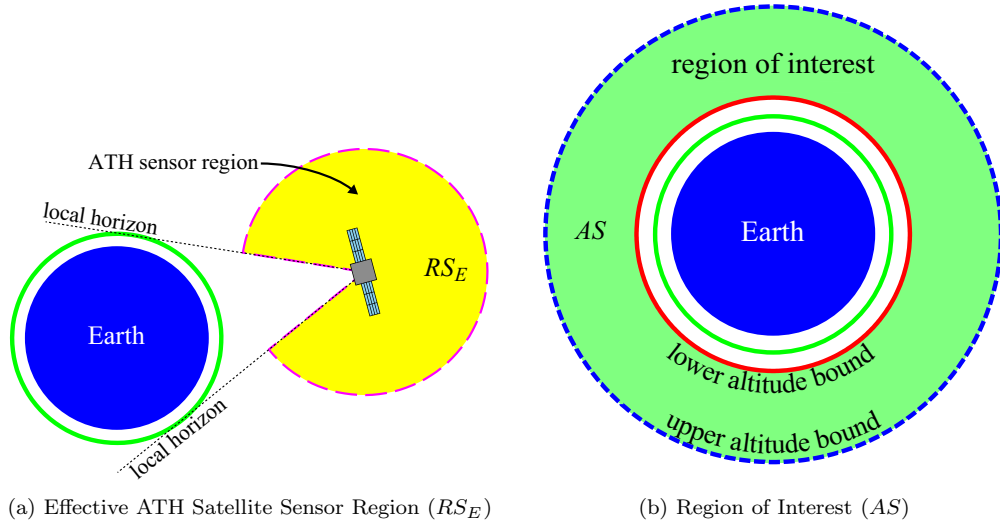(a) Effective ATH Satellite Sensor Region (RS_E) (b) Region of Interest (AS)

Figure 2: Sensor Region and Region of Interest

4.2 Single Coverage

Once the individual satellite ATH coverage regions and region of interest are discretized into polygons, the total region of single coverage within the region of interest can be determined using n Boolean operations (performed using polygon clipping). This process is illustrated in Figure 3. Figures 3a-3i show how the total effective ATH coverage region is formed using $n-1$ union operations. Subsequently, the total effective ATH coverage region is intersected with the region of interest, as shown in Figures 3j-3l, yielding the region of ATH coverage in the region of interest, $C_{1\times}$. The area of this polygon region is readily determined numerically,[6] and can be used as a constraint or objective function in a parameter optimization problem.[3]

The process illustrated in Figure 3 is expressed in the set notation expression:

$$C_{1\times} = \left(\bigcup_{i=1}^{n} RS_{E_i} \right) \cap AS. \tag{1}$$
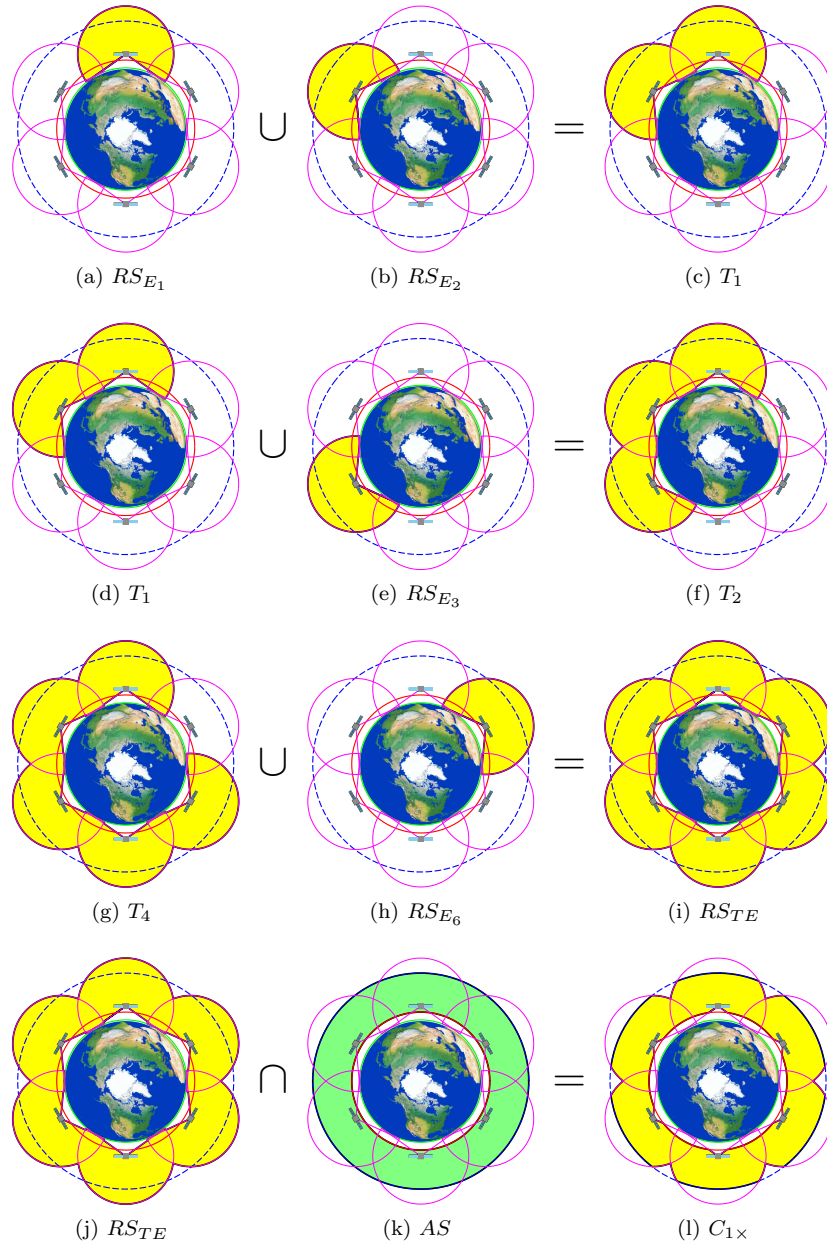
Figure 3: Single Coverage Illustration – 6 Satellite Constellation

4.3 Double Coverage

The general approach to the double coverage case is similar to the single coverage case in that the regions of double coverage are joined by union operations to form a total effective coverage region that is intersected with the region of interest. In the single coverage case, each effective sensor coverage region itself exhibits the desired coverage multiplicity. In contrast, regions of double coverage are determined by performing intersection operations between unique and valid pairs of effective coverage regions. The pairs must be unique in the sense that, for example, comparing satellites A and B for overlap is equivalent to checking satellites B and A (i.e. avoid permutations of pairs that have already been checked because they only offer redundant information). Similarly, analyzing for overlap between satellites A and A is also an invalid comparison because a satellite cannot provide double coverage on its own.

Figure 4 illustrates the sequence of Boolean operations necessary to determine the region of double coverage in the region of interest, $C_{2\times}$. Figures 4a-4c and Figures 4d-4f illustrate the identification by Boolean intersection of two unique regions exhibiting double coverage between neighboring satellites. These two unique regions are then combined using a union operation, as shown in Figures 4g-4i. As more regions of double coverage are identified, they are also joined until the total effective ATH coverage region, RS_{TE}, is identified, shown in Figure 4j. RS_{TE} is then intersected with AS to form $C_{2\times}$, the region of double ATH coverage within the region of interest, as shown in Figure 4l. The upper bound on the number of Boolean operations involved in this process is $(n^2 - n)/2$.[3]

The sequence of Boolean operations can be expressed in set notation as:

$$C_{2\times} = \left(\bigcup_{i_1=1}^{n-1} \bigcup_{i_2=i_1+1}^{n} \left(RS_{E_{i_1}} \cap RS_{E_{i_2}} \right) \right) \cap AS, \tag{2}$$

where the indices on the finite union operators are specifically chosen to avoid invalid or redundant satellite pair comparisons.[3]
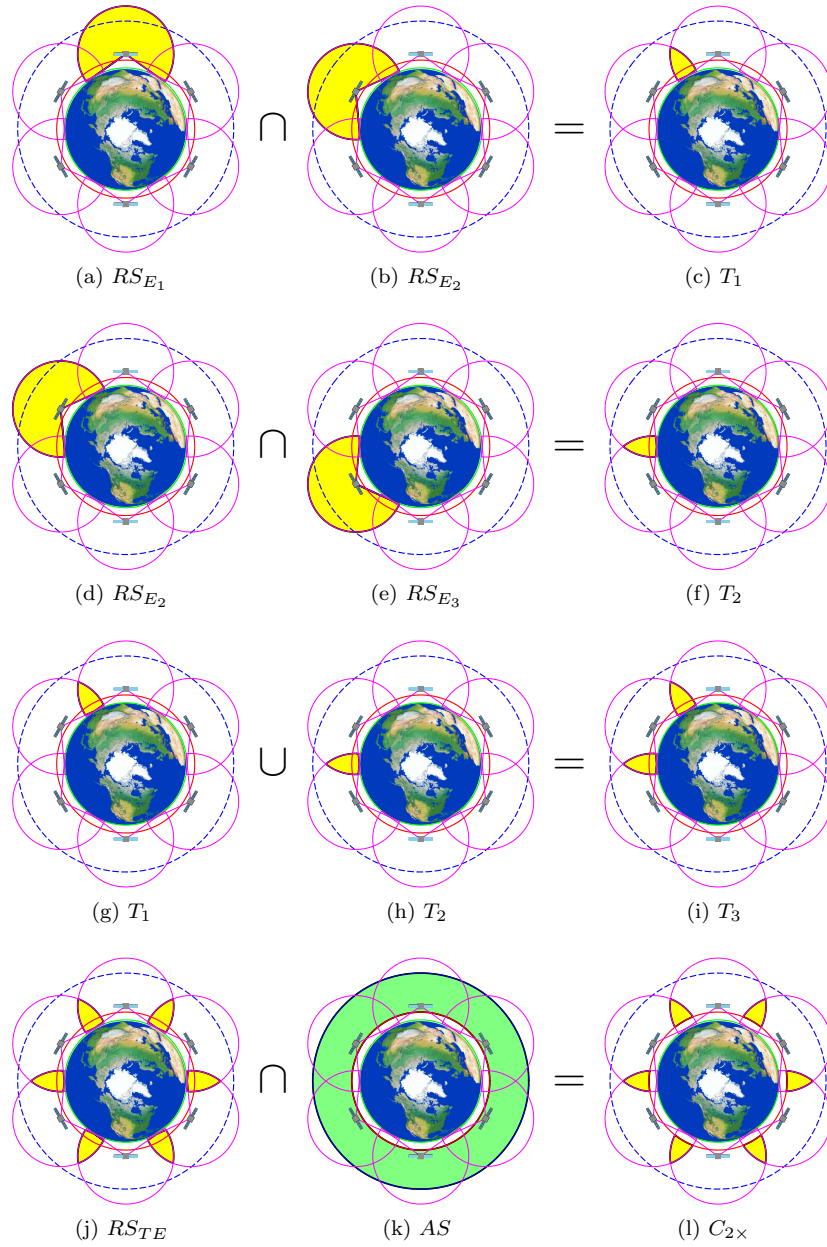
Figure 4: Double Coverage Illustration – 6 Satellite Constellation

4.4 Arbitrary Coverage Multiplicity

Investigation into the single, double, and triple[3] coverage cases leads to a generalized expression to efficiently identify regions of any desired coverage multiplicity, denoted by p (integer). The sequence of Boolean operations is compactly described in set notation as:

$$C_{p\times} = \left(\bigcup_{i_1=1}^{n-p+1} \bigcup_{i_2=i_1+1}^{n-p+2} ... \bigcup_{i_{p-1}=i_{p-2}+1}^{n-1} \bigcup_{i_p=i_{p-1}+1}^{n} \bigcap_{j=1}^{p} RS_{E_{i_j}} \right) \cap AS. \tag{3}$$

The primary complexity in developing this expression is in determining the appropriate indices on the finite union operators to avoid redundant or invalid p-tuplets.[3] For values of $p = 1, 2$, Equation 3 simplifies to the

cases shown in Equations 1 and 2.

4.5   Implementation

The set notation expressions developed in Sections 4.2-4.4 are completely implemented in both MATLAB
and C++. The development process and resulting algorithms are extensively documented,[3] with an emphasis
on analysis of the accuracy of discretized region approximation, and algorithm performance. Using those
results, given a required relative accuracy of the discretized region, an appropriate polygon resolution may be
selected and algorithm runtime can be estimated for both the MATLAB and C++ implementations (runtime
increases linearly with polygon resolution).[3]

The MATLAB implementation utilizes the General Polygon Clipping Library,[7] written in C. Via a
MEX gateway, the MATLAB implementation performs polygon clipping operations using the compiled
binary. Because polygon clipping is by far the most computationally intensive component of the analysis,
performance of the MATLAB implementation is only slightly slower than its C++ counterpart. The C++
implementation is found to operate approximately 4 times faster than the MATLAB implementation, and
should be used for any large scale problems that require a large number of function evaluations to solve.[3]
However, for most investigations, that are typically smaller in scale, the MATLAB implementation is used
exclusively for convenient access to the available MATLAB visualization capabilities. In contrast to the
MATLAB/C implementation, the C++ implementation has yet to be extended to the volumetric case, as
will be discussed in Section 6

5 Planar Analysis Example Problems

The examples presented in this section demonstrate the application of the planar constellation analysis methodology developed in the previous section to simple constellation optimization problems. Simple time-invariant models are optimized first, followed by several time-varying models of greater complexity.

5.1 Time-Invariant Problems – Grid Search

Cases where the distances between the satellites and target regions remain fixed may be considered time-invariant. That is, the amount of ATH coverage remains constant as the satellites in the constellation evolve along their orbit. Based on this assumption, the following examples demonstrate the use of the discussed methodology in optimal constellation design. The first example presents the minimum number of satellites required, over a range of constellation altitudes, to achieve 99.9% single, double, and triple coverage over a range of altitudes. The second example expands on this by also considering the omni-directional sensor range as a design parameter.

5.1.1 Example 1: A Single Independent Variable Case

A planar constellation providing ATH coverage to an Earth-centered annular target region is considered. The n omni-directional sensor platforms are equally distributed in a single circular orbit. Constellation altitudes between 100 and 6000 km are considered at 1 km resolution. The remaining problem parameters are defined in Table 1. At each altitude, the minimum constellation populations providing at least 99.9% single, double, or triple coverage are determined with a simple grid search, the results of which are shown in Figure 5 and Table 2. Just as coverage area is computed numerically, so is the area of the target region. Due to roundoff and truncation error, the two computed areas may not be the same, despite representing the exact same regions. To prevent this from causing an erroneous result, 99.9% coverage is considered rather than 100%. The minimum-altitude constellation configurations providing single, double, and triple coverage are shown in Figures 6a-6c.
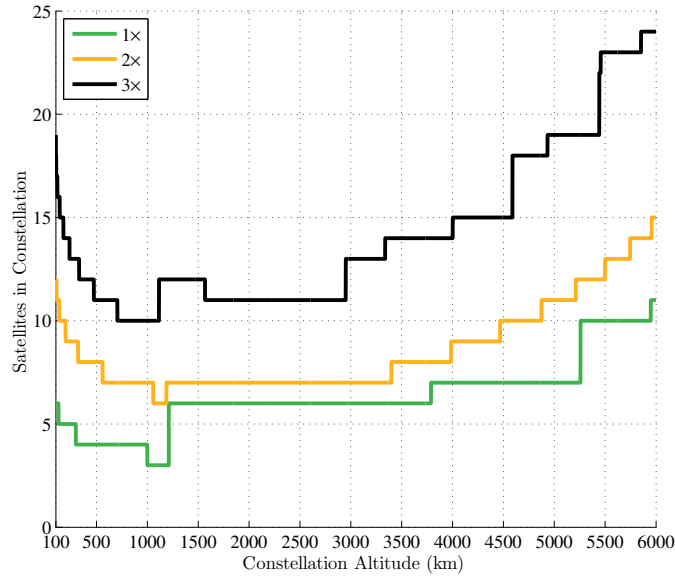

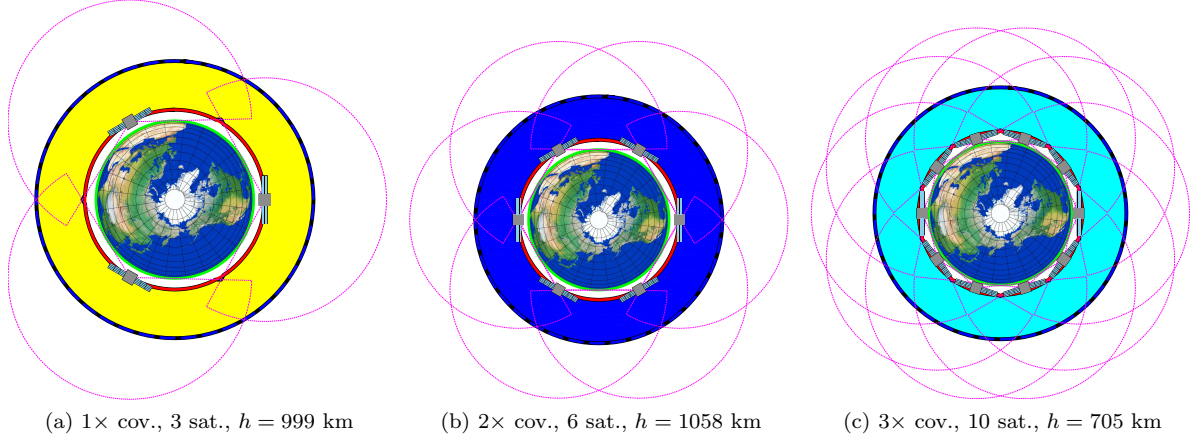Figure 5: Minimum Constellation Population vs. Altitude

(a) 1× cov., 3 sat., $h = 999$ km   (b) 2× cov., 6 sat., $h = 1058$ km   (c) 3× cov., 10 sat., $h = 705$ km

Figure 6: Smallest Constellations Providing at Least 99.9% ATH Coverage at Different Multiplicities

Table 1: Example 1 Parameters

Parameter	Description	Value
h_t	tangent height	100 km
h_l	lower target altitude	1000 km
h_u	upper target altitude	5000 km
R	omni-directional sensor range	10000 km
m	initial polygon resolution	100 PPC

Table 2: Example 1 Optimal Solutions

Coverage Mult.	Optimal Pop.	Altitude Range
1×	3 satellites	$999 - 1210$ km
2×	6 satellites	$1058 - 1187$ km
3×	10 satellites	$705 - 1113$ km

13

5.1.2 Example 2: A Two Independent Variable Case

Expanding upon the problem in Example 1, in addition to varying circular orbit altitude (19500-36000 km), variation in omni-directional sensor range (17000-30000 km) is considered in a 400×400 grid. Typically, sensor range is a fixed quantity depending upon available hardware. However, such an analysis may be useful during a trade study to determine the minimum sensor performance required to achieve coverage subject to other constraints. The problem parameters are shown in Table 3. The minimum number of satellites required to achieve at least 99.9% single coverage across the phase space is shown in Figure 7.
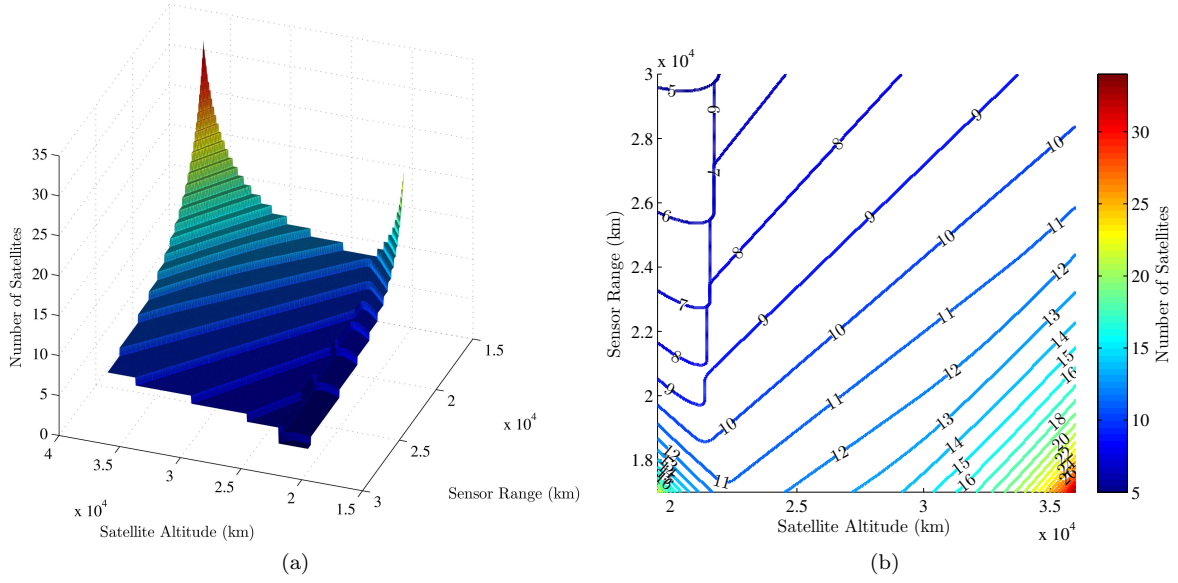
Figure 7: Minimum Constellation Size For 99.9% Single Coverage vs. Altitude and Sensor Range

Table 3: Example 2 Parameters

Parameter	Description	Value
h_t	tangent height	100 km
h_l	lower target altitude	20000 km
h_u	upper target altitude	36000 km
m	initial polygon resolution	100 PPC

5.2 Time-Invariant Problems – Non-Linear Programming

To illustrate the utility of the numerical ATH coverage models, several example problems are solved using a Non-Linear Programming solver (MATLAB's *fmincon*).[8] Prior to this, a simple continuously differentiable financial model describing constellation deployment cost is developed for use as both an objective function and a constraint function. Example 3 considers minimization of deployment cost subject to a constraint on minimum acceptable ATH coverage. Example 4 illustrates the use of an arbitrary sensor profile in a constellation design problem, maximizing single ATH coverage subject to a constraint on deployment cost.[3]

5.2.1 Simple Financial Model

The design problems described in this section involve constraining or minimizing financial cost, while simultaneously maximizing or constraining (respectively) some amount of coverage at a specified coverage

multiplicity. Models estimating program cost for a satellite or constellation are used throughout government and industry (see Wertz).[9] These models are highly complex with a staggering amount of parameters involved. Additionally, these exhaustive models can behave discontinuously in many regions, i.e. when a payload of several satellites becomes too massive for one launch vehicle, necessitating another.

The objective of the examples in this section is not to illustrate these complex cost estimation relations, but to illustrate how the numerical ATH coverage models briefly described in section 4 can be used as part of a constellation design process. Consequently, a much simpler financial model is desirable, one that is continuous, easily described to the reader, and easily implemented by the investigator.

The model developed here focuses on two parameters as cost drivers behind constellation deployment – the mass of each spacecraft, and their circular orbit altitude. The current study focuses on constellations composed of satellites arranged in a single circular orbit. The time-invariant nature of this set of problems allows them to be far more tractable using the limited computational resources available.

Constellation Deployment Cost According to Gordon,[10] the mass of a sensor or antenna can be crudely described as proportional to the square of its design range. Using this relationship, spacecraft mass can be approximated by

$$m = a + bR^2. \tag{4}$$

The parameter a is the base satellite mass (i.e. if no sensor were installed at all), and b represents the mass/sensor-range coefficient. The total cost of constellation deployment is then described by

$$\Gamma = n(e + cm + dm(h - h_{\mathrm{ref}})^2). \tag{5}$$

A linear relationship between the number of satellites, n, and deployment cost Γ is assumed. The parameter e represents a base cost for each launch system, c represents the additional cost per unit mass to achieve the reference circular orbit at an altitude of h_{ref}. The cost of increasing satellite altitude (h) from the reference altitude is assumed to increase quadratically, thus the coefficient d describes the cost per unit mass vs. the square of the increase in altitude. This assumption of quadratic behavior with respect to altitude variation is made to create a more interesting deployment cost model, i.e. not just quadratic in R, but also in h. In all analyses presented here, h_{ref} is considered to be the lower bound on permissible satellite altitude.

Mass and altitude are the originally intended cost drivers; however, by Equation 4, R is used in place of mass as a model parameter.

Parameter Values All but one of the parameters used in the deployment cost model remain the same in both Examples 1 and 2. However Example 2 considers a satellite sensor profile of arbitrary shape, where the mass/sensor-range coefficient is reduced by a factor of four. This assumption is made because, as will be seen in Section 5.2.4, the arbitrary region encompassed in RS_{arb} is much smaller than in an omni-directional case using the same value of R. The resulting financial costs computed using these parameters are not necessarily correlated to real world dollars, and are only intended as a means of comparison between the solutions and problems presented here. They are, however, selected with the aim of obtaining results on the same order-of-magnitude as a more exhaustive analysis.[9] These parameters are summarized in Table 4.

Table 4: Financial Model Parameters (see Equations 4, 5)

Parameter	Value	Description
a	500 kg	base satellite mass
b_{OD}	6×10^{-5} kg/km^2	mass/sens-range coefficient (OD sensors)
b_{arb}	1.5×10^{-5} kg/km^2	mass/sens-range coefficient (arb. sensors)
c	1×10^{-4} \$M/kg	cost-per-kg at reference altitude
d	1×10^{-9} \$M/kg-km^2	cost-per-kg vs. squared altitude increase
e	10 \$M	base launch vehicle cost
h_{ref}	188 km	satellite reference altitude

5.2.2   Non-Linear Programming

The examples presented in this section are simple constellation design problems, and their solutions are easily obtained by parameter optimization. The problems are parameterized in terms of a finite set of variables that fully define a unique state of the system. The solution, or optimal values of these variables create some optimal condition of the system in whatever sense the investigator defines (by finding the states providing minimal or maximal values of some performance index). Although the examples in this section are simple enough to be analyzed based on clever plots alone, the same method of parameter optimization can be readily scaled to more complex problems, for which visualization of the phase space becomes impossible.

The parameter optimization code used here is provided in the MATLAB Optimization Toolbox – *fmincon*,[8] which is a package of several different non-linear programming (NLP) packages. Loosely defined, NLP is a process by which some objective function is extremized subject to equality and/or inequality constraints, all dependent upon a finite set of optimization variables. Additionally, the objective function and the constraints could both exhibit non-linear behavior (NLP can be considered a superset of linear programming – linear programming can be used only when the objective and constraint functions are linear). Specifically, the sequential quadratic programming (SQP) algorithm (see Powell)[11] in *fmincon* is used to obtain solutions to the example problems in this section. The general problem solved by NLP is as follows:

$$\text{minimize } J = F(\mathbf{x}_p), \tag{6}$$
$$\text{subject to } \mathbf{c}_{\text{eq}}(\mathbf{x}_p) = \mathbf{0}, \tag{7}$$
$$\mathbf{c}(\mathbf{x}_p) \leq \mathbf{0}, \tag{8}$$

keeping in mind that maximizing a function is equivalent to minimizing its negative.

5.2.3   Example 3 – Min. Budget with an Area Constraint

The constellation designed in this example must provide single coverage to at least 99.9% of the total area enclosed in the dual-altitude band shell. This value, rather than 100%, is arbitrarily chosen to avoid numerical issues associated with roundoff and truncation error (however small they may be). The parameters describing the tangent height shell (THS) and the dual-altitude band shell, AS, are shown in Table 5 along with the computed area inside AS.

Table 5: Example 3 Parameters

Parameter	Value	Description
R_E	6378.14 km	assumed Earth radius
h_t	100 km	tangent height altitude
h_l	1000 km	lower target altitude
h_u	5000 km	upper target altitude
m	100 PPC	initial polygon resolution
A_{AS}	235,307,769 km^2	total area in AS

Assume that the satellites are equally distributed in a single circular orbit, and are equipped with omni-directional sensors. Under these assumptions, the satellite sensor range, R, and the satellite altitude, h, are sufficient to fully define a unique state of the system. The two-dimensional set of variables populates the parameter vector

$$\mathbf{x}_p = \begin{bmatrix} R & h \end{bmatrix}. \tag{9}$$

The performance index that is minimized with respect to $\mathbf{x}_p$ (deployment cost, according to the model developed in Section 5.2.1) is given by

$$J = \Gamma(R, h, n). \tag{10}$$

Additionally, three inequality constraints are present as follows:

$$\mathbf{c} = \begin{bmatrix} A_{\min} - A_{1\times} \\ -R \\ h_{\text{ref}} - h \end{bmatrix} \leq \mathbf{0}, \tag{11}$$

16

where the inequality is understood to apply element-wise between vectors **c** and **0**.

The parameters and solution to the 3 satellite case are shown in Table 6.

Figure 8a shows the area constraint (the solution must lie inside or on the dotted boundary). From inspection of Figure 8c, it is clear to see that the converged solution does correspond to a constrained minimum in deployment cost. The configuration of the converged solution, shown in Figure 9b, illustrates that the sensor range corresponds to the intersection between neighboring satellite sensor range shells and the upper target altitude shell (UTAS), as expected by intuition.

Table 6: Example 3 – Parameters and Solution

Parameter	Value	Description
n	3	number of satellites
$A_{\min}$	$0.999A_{AS}$	area constraint
R_0	1000 km	initial guess, R
h_0	1000 km	initial guess, h
R_{opt}	9889.940 km	converged cost-optimal R
h_{opt}	1038.909 km	converged cost-optimal h
Γ_{opt}	234.893 \$M	converged cost at solution
$A_{1\times_{\text{opt}}} - A_{\min}$	-1.095×10^{-2} km^2	coverage area surplus

5.2.4   Example 4 – Arbitrary Sensor Profile

This problem illustrates how arbitrary sensor profiles can be used with the numerical ATH coverage models developed in Section 4 to design constellations. The satellite sensor cross-section considered here is by no means based on any real-world hardware. Prior to addressing the actual design problem, a brief discussion is presented that illustrates how the effective satellite range shell, RS_E is obtained, starting from a simple sketch.

Defining the Arbitrary Effective Range Shell   One of the fundamental advantages of the numerical analysis of ATH coverage is that investigations are not restricted simply to the omni-directional sensor case, or any case where an analytical geometric representation of the sensor cross-section can be derived. Consider the case shown in Figure 10. This sketch represents half of an in-plane sensor cross-section, and was manually drawn by the investigator. There are no exact mathematical equations governing the path, making it 'arbitrary' for the purposes of this discussion.

Upon importation of the drawing via digital scanner, it is slightly adjusted using a graphics program to smooth the boundary and correct the angle at the end of the curve, making it perpendicular to the x direction (as intended). The resulting image is then analyzed using a figure analysis software package,[12] producing a series of (x, y) coordinates describing the half-curve. In MATLAB, the half-curve is imported, the sharp tip is moved to the origin, and the lower half is generated by replicating the (x, y) coordinates in reverse, while changing the y coordinates to their negative reciprocals. The coordinates are then scaled to produce a teardrop-shaped sensor cross-section that is of unit length, with a maximum width of 0.6. The sharp tip is centered on the spacecraft, as shown in Figure 11. This curve can then be scaled to any length, R, simply by multiplying all (x, y) coordinates by R (prior to any coordinate translation, of course).

Further, an in-plane attitude of the spacecraft (which is now a parameter, as the sensor is no longer omni-directional), α can be defined. This angle is defined relative to the plane that is orthogonal to the satellite position vector. Traditionally, this plane is referred to as the local horizon. However, in this study, 'horizon' refers to a circular boundary around the Earth, and the two concepts should not be confused. In-plane attitude is shown in Figure 12. Due to the symmetry about the satellite look-axis, denoted by the arrow on the satellite body in Figure 12, in-plane attitude is constrained by

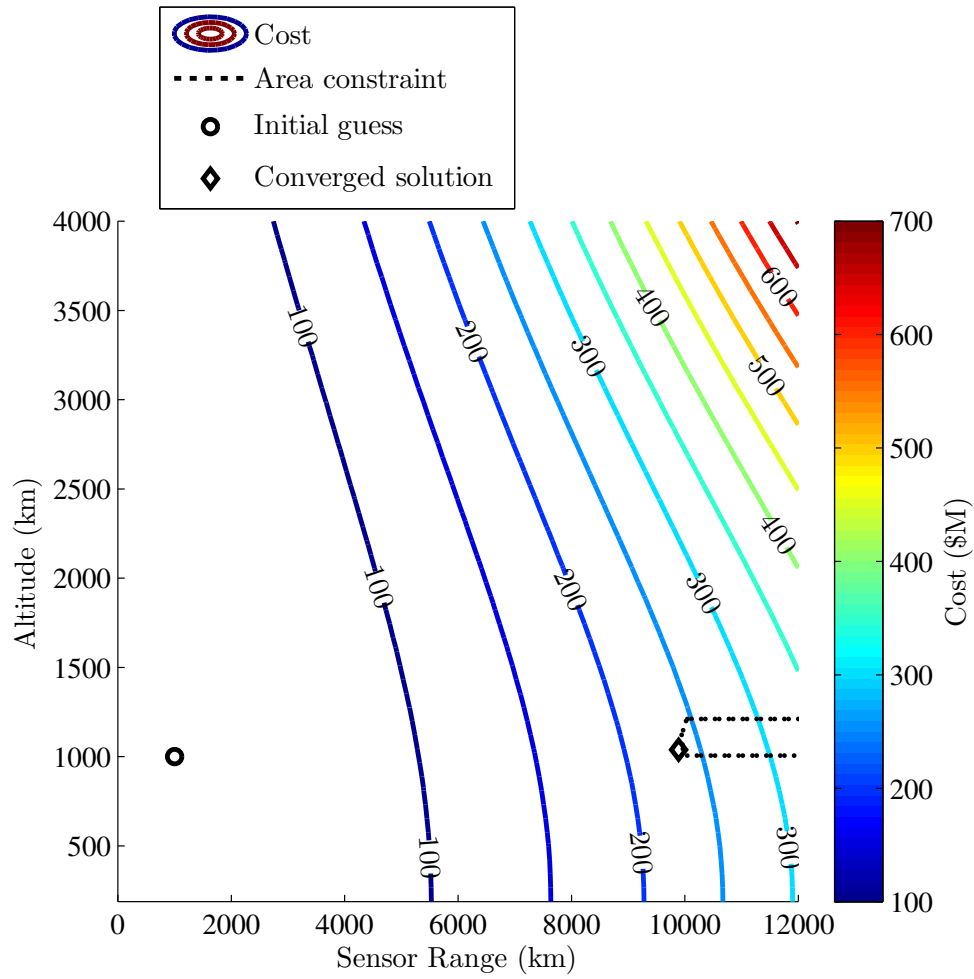$$-\frac{\pi}{2} \le \alpha \le \frac{\pi}{2}. \tag{12}$$

Once scaled, translated, and rotated as necessary, this arbitrarily shaped cross-section represents the sensor range shell, RS_{arb}.

17
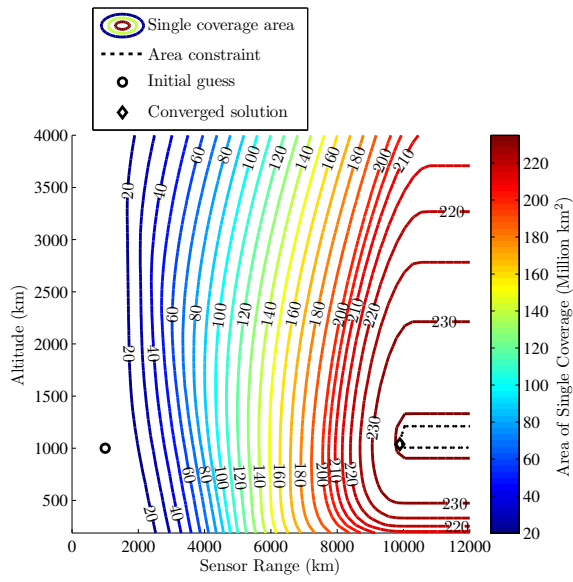
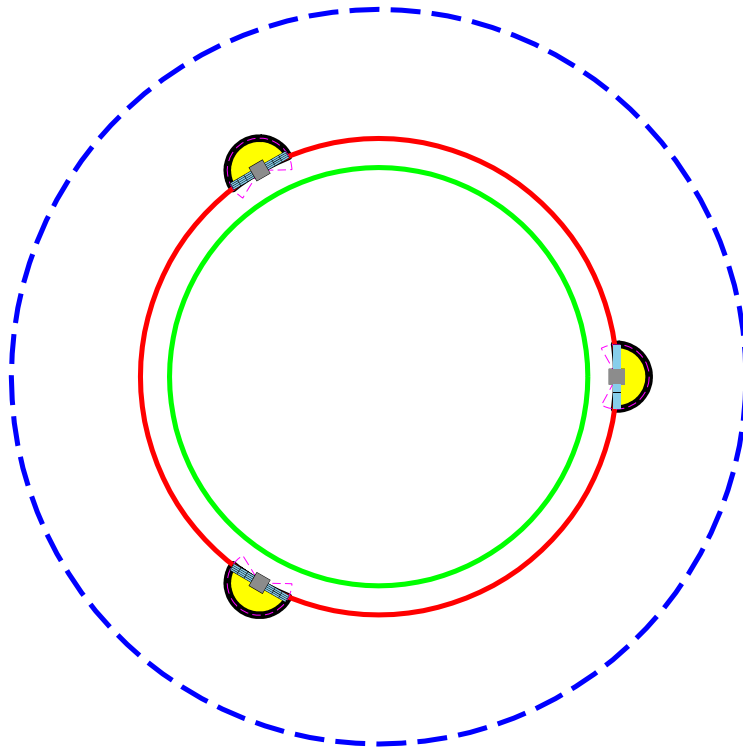(a) Constraint Function (Single Coverage Area)
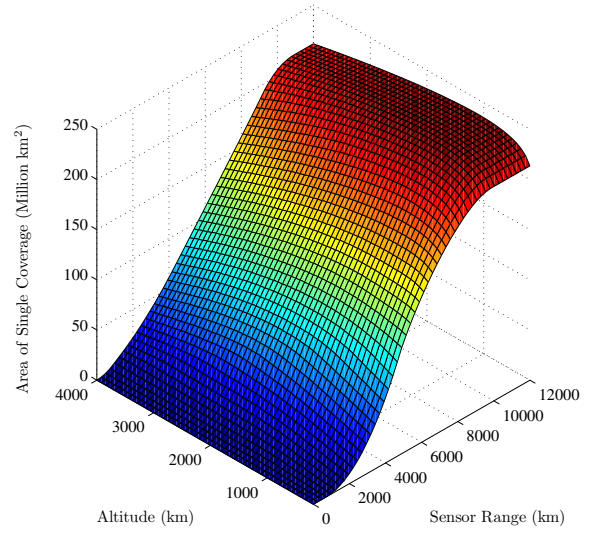
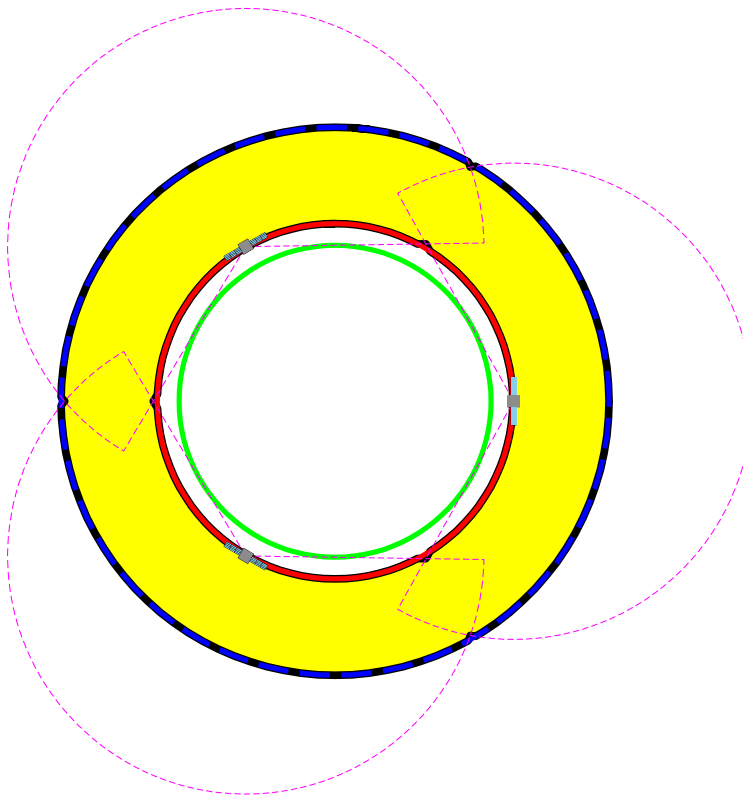
(b) Constraint Function (Single Coverage Area)

(c) Objective Function (Financial Cost)

Figure 8: Example 3 – Constraint and Objective Contours

18

(a) Initial Guess

(b) Converged Solution

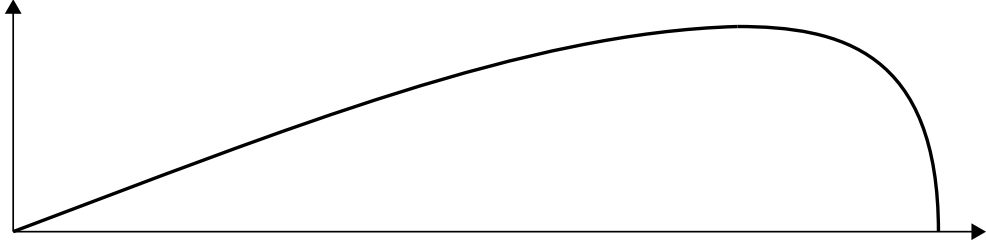Figure 9: Example 3 – Initial Guess and Converged Solution

Figure 10: Example 4 – A 'Back of the Envelope' Arbitrary Sensor Cross-Section
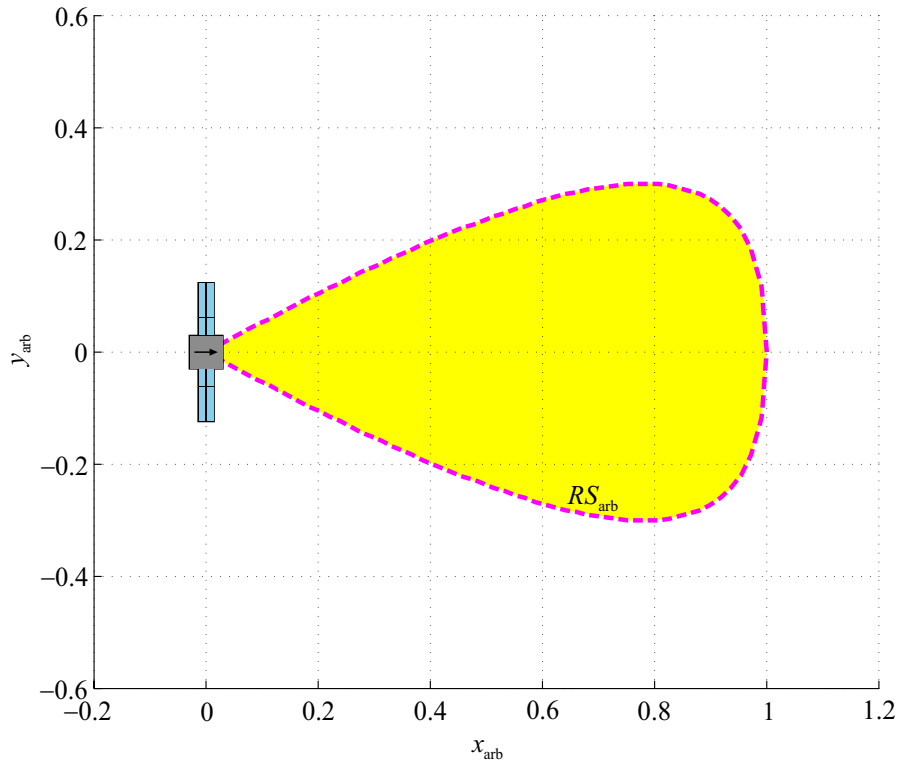

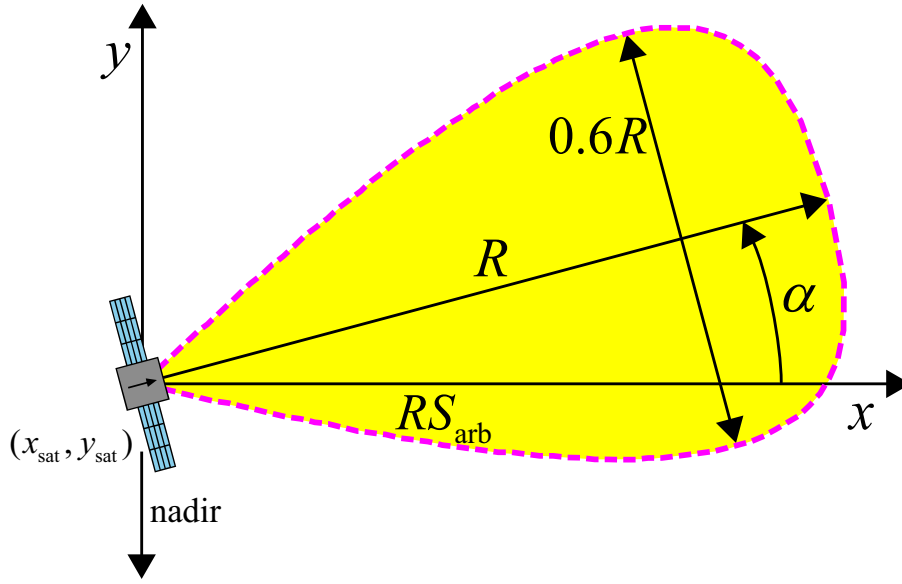Figure 11: Example 4 – Arbitrary Sensor Cross-Section Imported to MATLAB

Figure 12: Example 4 – Arbitrary Sensor Cross-Section Notation

Although this arbitrary sensor cross-section represents a tear-drop shape, *any* shape could be used, and placed anywhere in relation to the spacecraft. The only caveat is that the sensor region must be assumed to possess some form of symmetry across the orbit-plane such that ATH coverage measured in-plane somehow corresponds to ATH coverage in a three-dimensional volumetric sense.

Having defined the arbitrary range shell, RS_{arb}, the region corresponding to the tangent height triangle (THT) is removed in order to form the arbitrary *effective* range shell, RS_E. This involves the formation of a polygon representing the THT, that is used to perform the polygon clipping operation $RS - \mathrm{THT} = RS_E$. The two far-side vertices of the THT can be determined by simple geometry, and the third vertex is coincident with the satellite. The clipping operation is illustrated in Figure 13, where the THT is represented by the dashed triangle, and the shaded region represents the effective range shell, RS_E. The extent of the THT need only exceed the maximum extent of RS_{arb} to ensure there are no leftover regions beyond the THT after the clipping operation. In this example, the distance to the far side of the THT (along the look-axis) is chosen to be $1.1R$.

Possessing the means to generate the arbitrary effective range shells, it is then straightforward to utilize the numerical ATH coverage models developed in Section 4 to evaluate the coverage they provide.

Problem Statement and Solution   The problem solved in this example is maximization of single ATH coverage subject to a deployment constraint for an arbitrarily shaped sensor cross-section. It is important to note that the financial model parameters are slightly modified for this example, as shown in Table 4, where b_{arb} is used. This parameter is adjusted from b_{OD} to reflect the reduced coverage area relative to the sensor range, R.

First, the parameter vector is formed, similarly to Example 1, but with the addition of the in-plane attitude, α (uniform across the constellation):

$$\mathbf{x}_p = [R \quad h \quad \alpha]. \tag{13}$$

Next, the objective function is defined as

$$J = -A_{1\times}(R, h, \alpha, n), \tag{14}$$

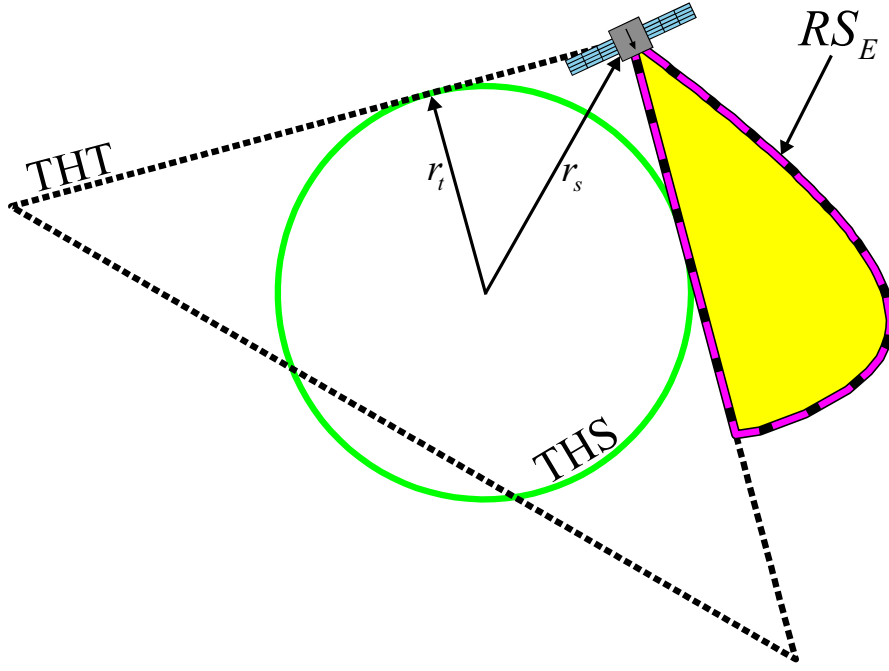which is to be minimized (to maximize single coverage). This problem is subject to five inequality constraints

21

Figure 13: Example 4 – Clipping the THT From RS_{arb} to Form RS_E

that are written in vector form as

$$
\mathbf{c} = \begin{bmatrix} \Gamma(R, h, n) - \Gamma_{\max} \\ -R \\ h_{\mathrm{ref}} - h \\ \alpha - \frac{\pi}{2} \\ \frac{\pi}{2} - \alpha \end{bmatrix} \leq \mathbf{0}. \tag{15}
$$

Note that the financial model, described in Section 5.2.1, does not depend upon in-plane attitude, α.

The parameters used in this problem are shown in Table 7. The initial guess is intentionally chosen to be far away in all three variables from the expected (by intuition) solution. Also note that although 100 PPC is the polygon resolution used for the altitude shell, the arbitrary range shell as generated in MATLAB consists of 110 vertices. This is purely an artifact of the curve generation process, and an order-of-magnitude similarity is considered acceptable.

Table 7: Example 4 – Parameters

Parameter	Value	Description
R_E	6378.14 km	assumed Earth radius
h_t	100 km	tangent height altitude
h_l	1000 km	lower target altitude
h_u	5000 km	upper target altitude
m	100 PPC	initial polygon resolution
n	7	number of satellites
$\Gamma_{\max}$	250 \$M	deployment cost constraint
R_0	1000 km	initial guess, R
h_0	4000 km	initial guess, h
α_0	45°	initial guess, α

After 41 SQP iterations, the optimizer converges to the solution shown in Table 8. In order to visualize this three degree-of-freedom problem, contours at the solution are produced holding one variable fixed, creating a pair of contour plots for ATH coverage area and deployment cost. Figure 14 depicts overall and detail contours when holding in-plane attitude constant at the solution. Note that the detail contour (Figure 14b) uses a rescaled color map, and the colors do not correspond to the colors in the overall contour (Figure 14a). These figures illustrate that coverage area only decreases in any feasible direction in R or h (i.e. not across the constraint boundary). Similarly, holding h fixed at the solution yields the contours shown in Figure 15. Just as in the case of constant in-plane attitude, any variation in R and α in a feasible direction results in a decrease in ATH coverage area. As with earlier examples constrained by deployment cost, because of the quadratic behavior of the cost function in both R and h, the solution must fall on or to the left of the constraint boundary.

While these contour illustrations are by no means sufficient condition to declare optimality of the solution, the SQP optimizer in *fmincon* does return a flag indicating that it has found a constrained locally optimal solution. The MATLAB SQP implementation utilizes a variation of the Karush-Kuhn-Tucker (KKT) conditions[13] as one of several criteria to determine optimality. Generally, KKT is only a necessary condition for optimality. However, for continuously differentiable and convex objective and constraint functions (as is the case in this problem), KKT also provides sufficient condition for optimality.[14]

Table 8: Example 4 – Solution

Parameter	Value	Description
R_{opt}	11396.402 km	converged area-optimal R
h_{opt}	897.559 km	converged area-optimal h
α_{opt}	$-5.937°$	converged area-optimal α
$A_{1\times_{\mathrm{opt}}}$	214,239,724 km^2	single coverage area at solution
$\Gamma_{\mathrm{opt}} - \Gamma_{\mathrm{max}}$	0 \$M	budget overrun

5.3 Time-Varying Problems

In cases with elliptical orbits, more complex target regions, or even constellations with populations distributed across multiple circular and/or elliptical orbits (in the same plane), the ATH coverage amount is time-varying in general. The overlap between sensor coverage and target regions varies continuously.

Time-varying problems may be analyzed using the techniques developed in this study by performing instantaneous coverage evaluations at specified times throughout a time interval of interest. Figure 18 shows the ATH coverage provided by a planar constellation of 6 sensor platforms in arbitrarily prescribed orbits with arbitrarily defined sensor profiles over a prescribed time interval. A sufficiently long time interval, and a sufficiently short time-step must be selected to ensure the analysis adequately characterizes the behavior of the system. In a system with periodic behavior, an appropriate time interval is one period. However, non-periodic cases such as that shown in Figure 18 are more difficult to analyze because the judgment of the analyst must dictate an appropriate time interval. The case shown in Figure 18, and animated in the accompanying video file, features 6 satellites with arbitrary sensor profiles in arbitrarily chosen coplanar elliptical orbits. Each sensor platform maintains a fixed (and prescribed) attitude with respect to the local horizon at all times. The target region is an Earth-fixed dual-altitude band region bounded in longitude.

Using this numerical approach, constellation design problems can be addressed using various parameter optimization techniques.

5.3.1 Example 5 – Analysis of Coverage by Elliptical Orbits

As in the time-invariant problems, an annular target region is considered. However, due to the time-invariant nature of the target region itself, a time-invariant solution is optimal, as is demonstrated in this example.

The problem is posed as a Mixed-Integer Non-Linear Programming (MINLP) problem and solved using MIDACO.[15] MIDACO is a zeroth order heuristic solver and uses an ant colony optimization (ACO) approach.[16] Because ACO is a heuristic approach to MINLP, there are no analytical optimality criteria for non-convex problems such as this, thus the algorithm is allowed to run until it ceases improvement upon the solution.

A constellation composed of two elliptical orbits with opposite periapsis directions is considered. Each orbit is initially populated by three satellites, each group with dissimilar omni-directional sensor performance. Within each orbit the satellites are equally spaced in mean anomaly. The objective is the minimize the total population of the constellation, while ensuring continuous single coverage of the target region. The formulation allows for one or both orbits to have zero population (although zero population in both orbits results in an obvious violation of the continuous coverage constraint). Problem parameters are summarized in Table 9.

Table 9: Example 5 – Parameters

Parameter	Description	Value
h_t	tangent height	100 km
h_l	lower target altitude	1000 km
h_u	upper target altitude	10000 km
k	number of distinct orbits in constellation	2 orbits
R_1	omni-directional sensor range of sats. in orbit 1	5000 km
R_2	omni-directional sensor range of sats. in orbit 2	10000 km
m	initial polygon resolution	100 PPC

Table 10 shows the start point and solution after 300 seconds (682 function evaluations). From an infeasible start point (coverage gaps), as seen in Figure 19-a, a feasible 12 satellite state is identified by the 15th function evaluation. By the 98th function evaluation, the solution presented in Figure 19-b is converged upon. With 6 satellites distributed in a single circular orbit, the solution is time-invariant when only concerned with the quantity of coverage, as expected.
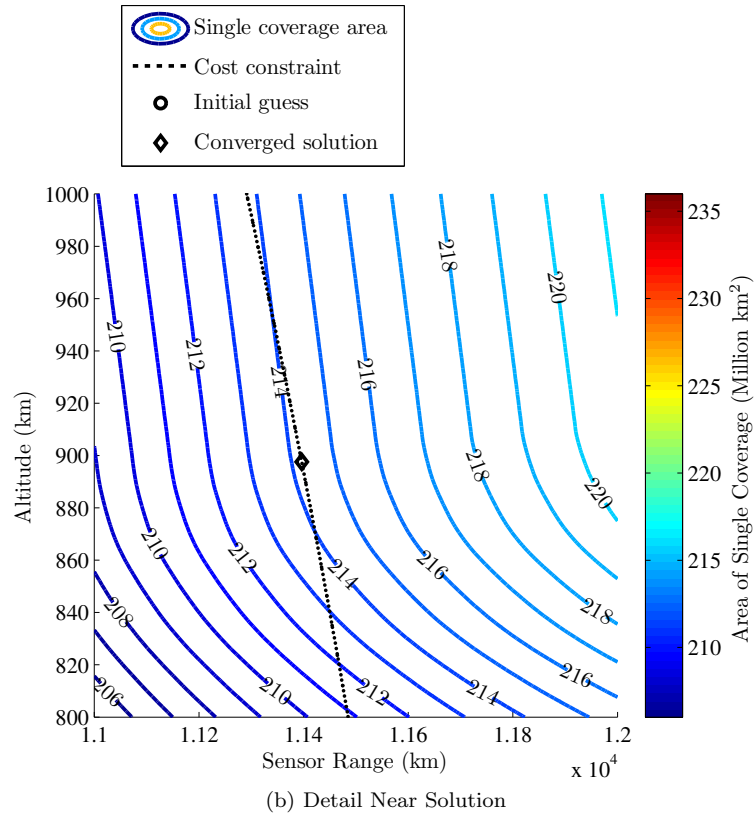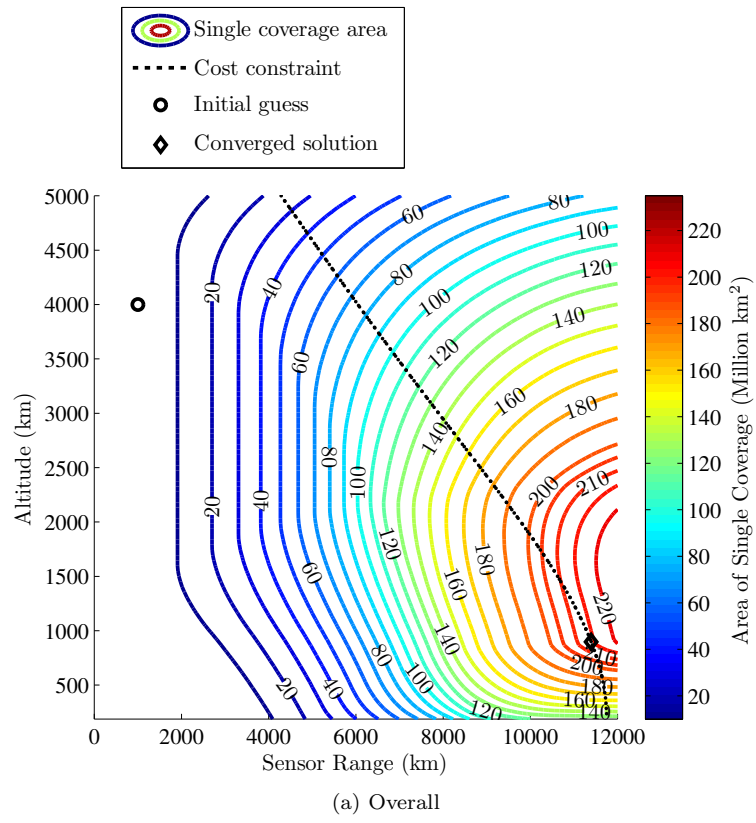
(a) Overall

(b) Detail Near Solution

Figure 14: Example 4 – Objective Function (Single Coverage Area, Constant $\alpha = -5.937°$ at Solution)

(a) Overall
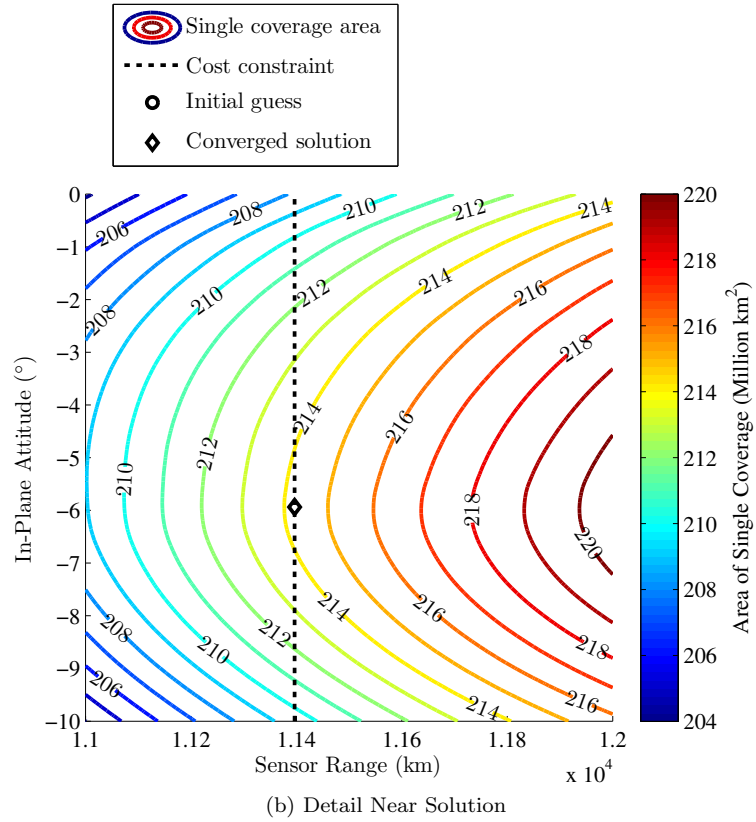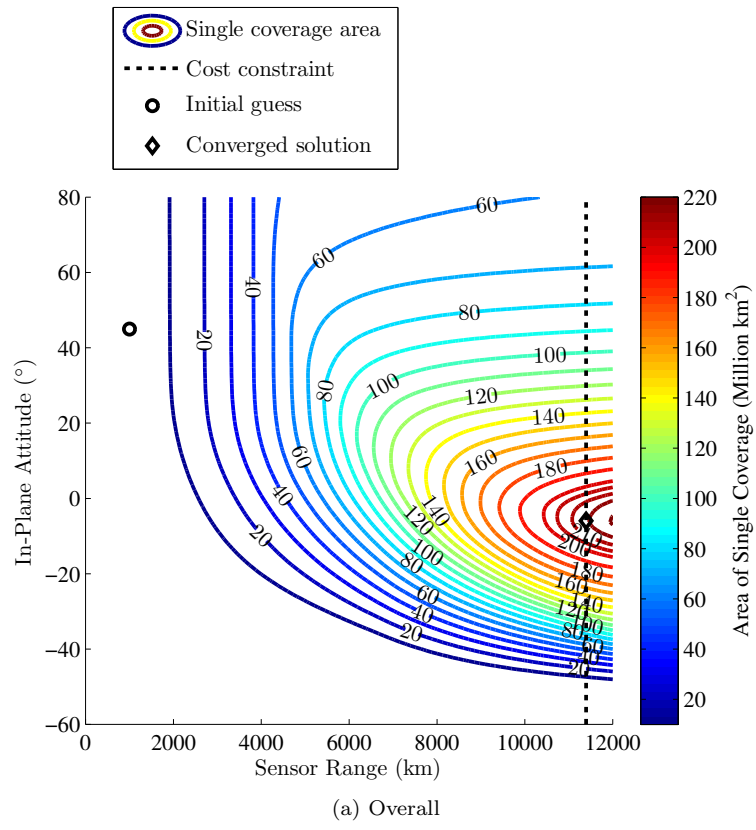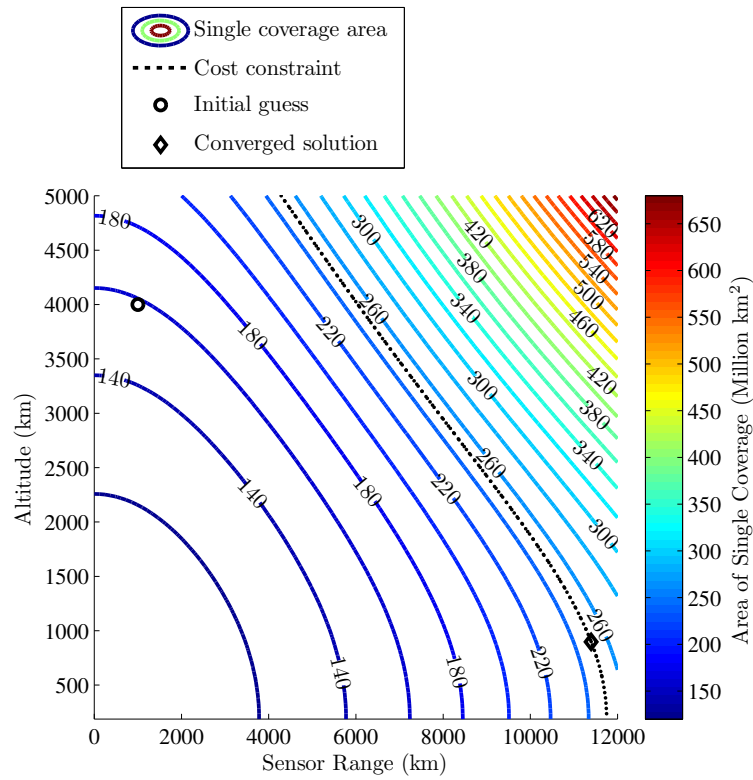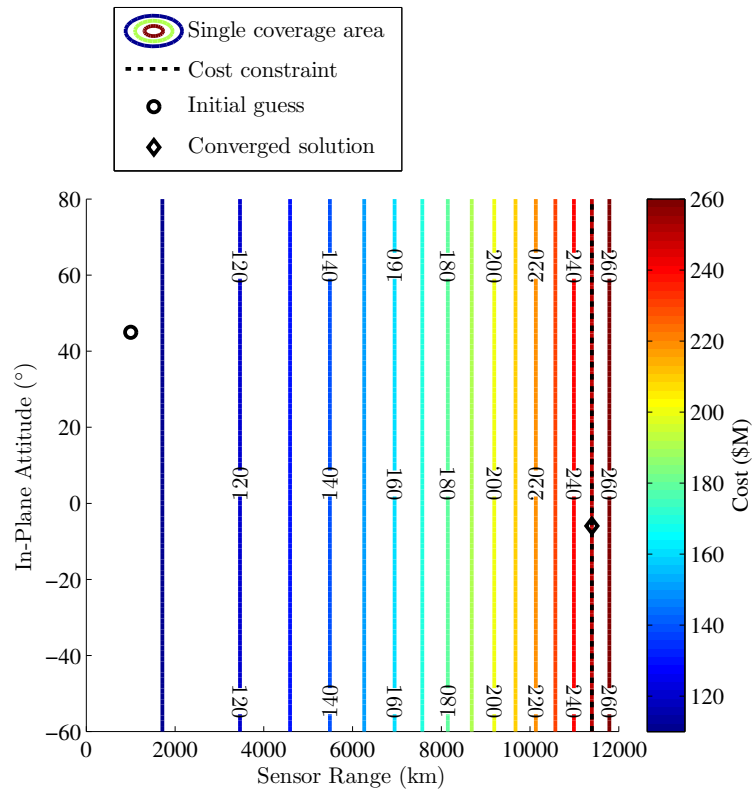

(b) Detail Near Solution

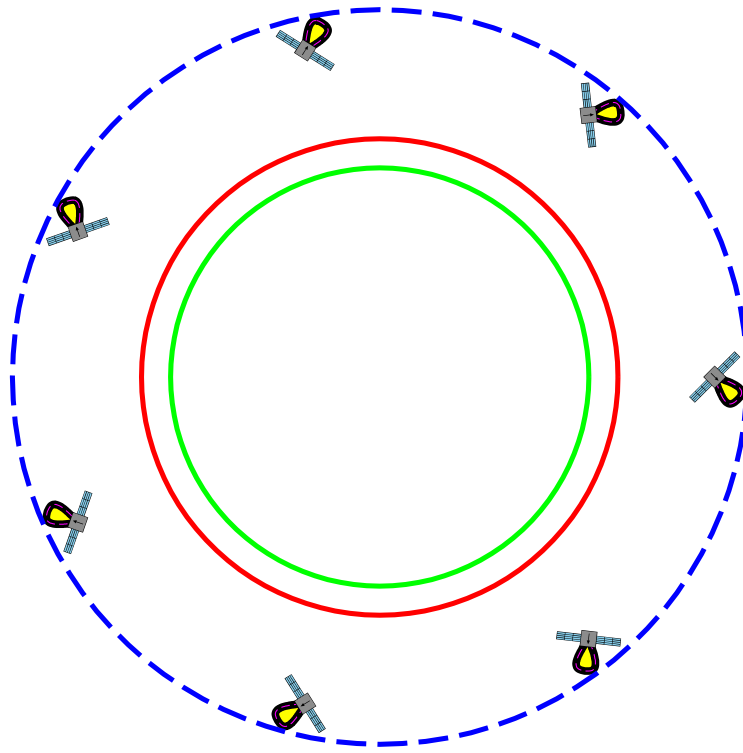Figure 15: Example 4 – Objective Function (Single Coverage Area, Constant $h = 897.559$ km at Solution)
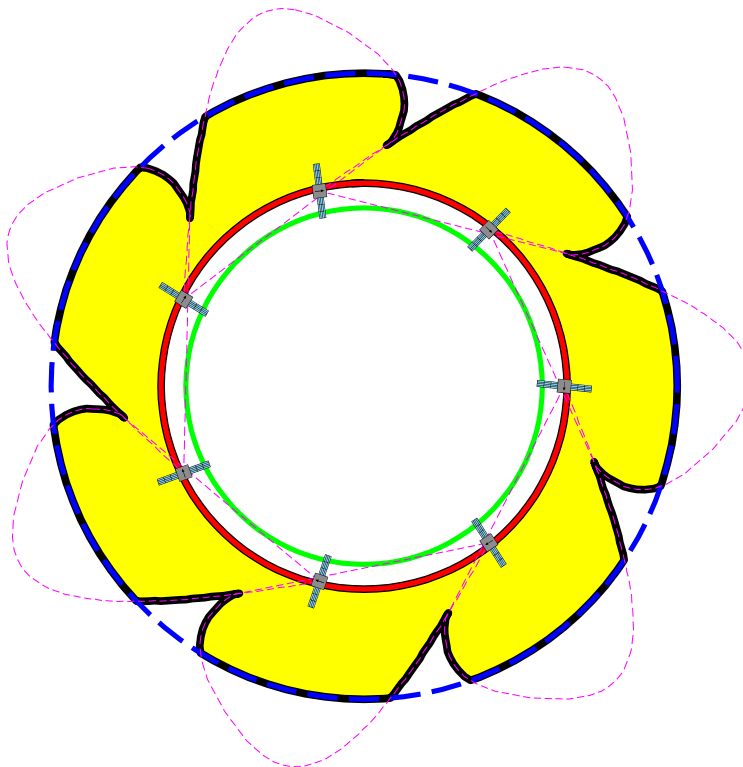
(a) Constant $\alpha = -5.937°$ at Solution

(b) Constant $h = 897.559$ km at Solution

Figure 16: Example 4 – Constraint Function (Deployment Cost)

(a) Initial Guess

(b) Converged Solution

Figure 17: Example 4 – Initial Guess and Converged Solution

28
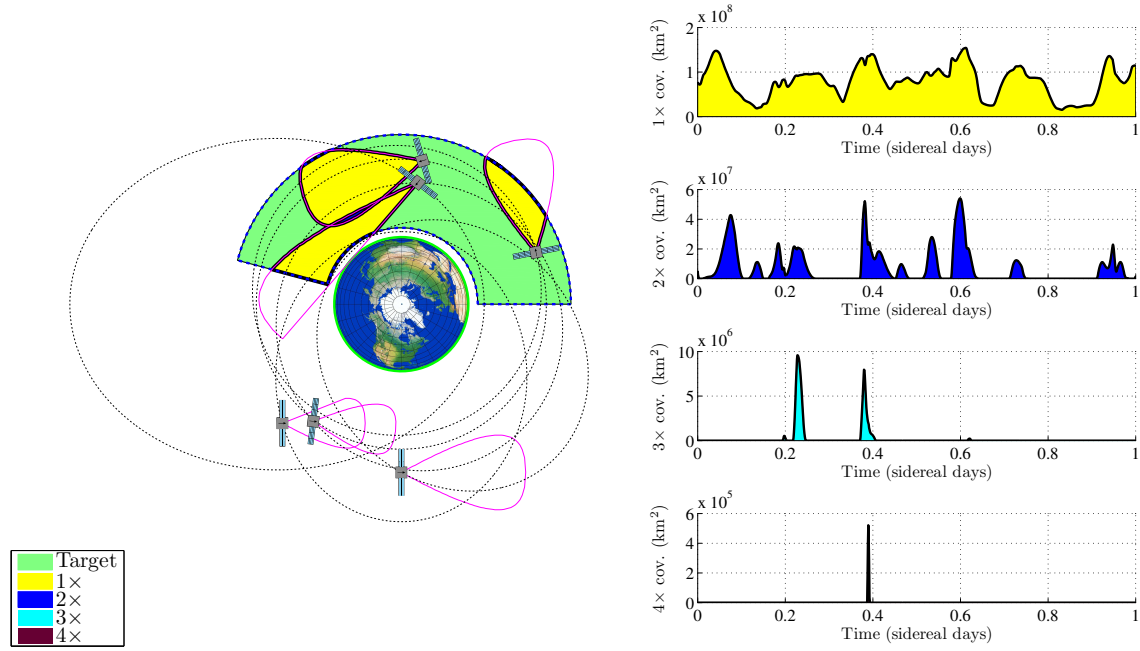
Figure 18: ATH coverage over time – arbitrary sensor profiles, asymmetric target region (see accompanying video #1)

Table 10: Example 5 – Start Point & Solution (682 func. evals, 300s)

Decision Variable	Description	Start Point	Solution
a	semi-major axis (both orbits)	10000 km	8588.0
e	eccentricity (both orbits)	0.25	0
M_{2_0}	M at epoch for lead sat. in orbit 2	0 rad	0 rad
n_1	orbit 1 population	3 satellites	0 satellites
n_2	orbit 2 population	3 satellites	6 satellites
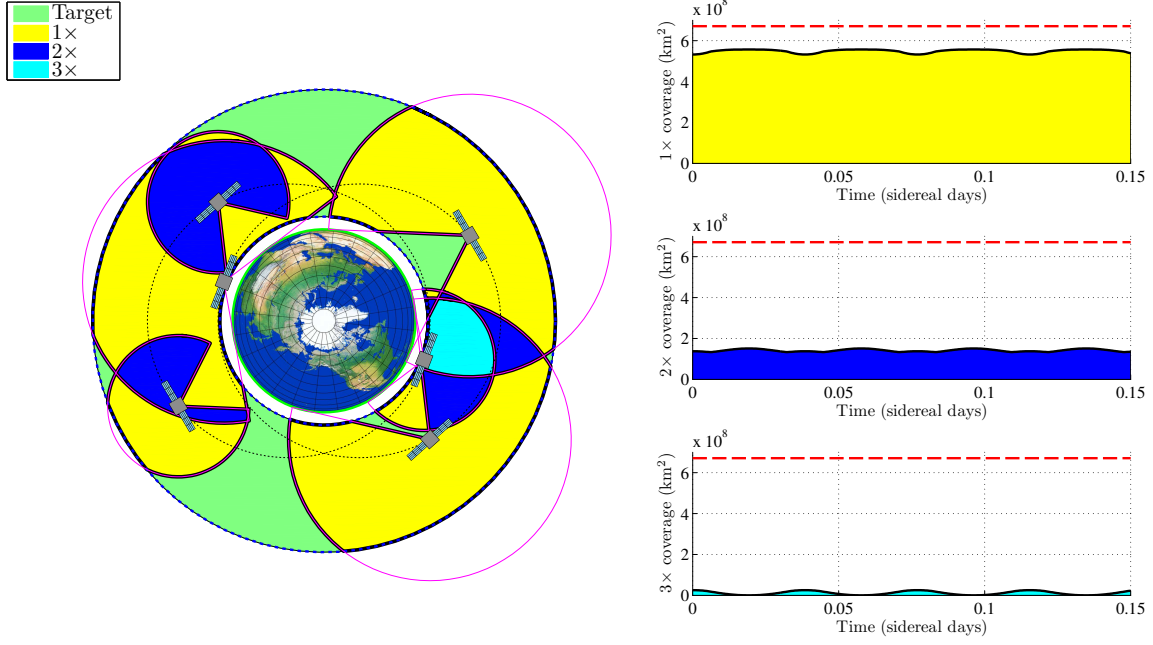
(a) Start Point
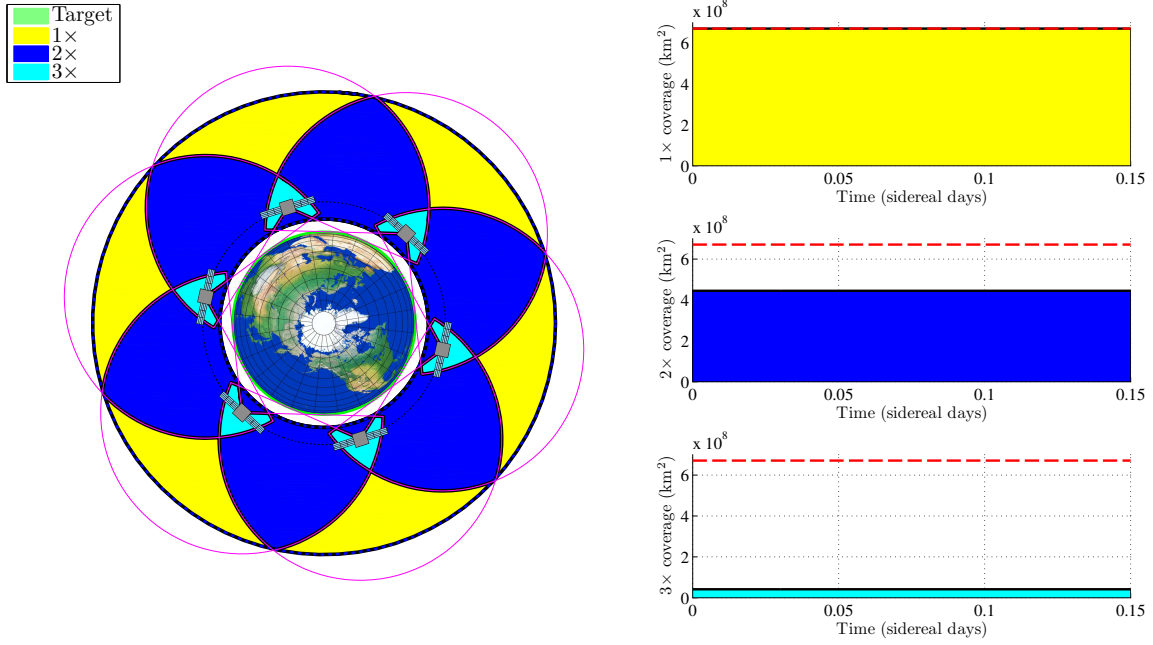
(b) Solution

Figure 19: Example 5 – Start point to solution with continuous 1× coverage constraint (see accompanying video #2)

5.3.2 Example 6 – Continuous Observation of CONUS GEO Satellites

In contrast to the previous example, an asymmetric Earth-fixed target region is considered here. From a geostationary orbit, the target region is defined as ± 1000 km in altitude, between 148°W and 61°W longitude (populated by satellites serving the continental United States).

One immediately obvious solution corresponds to placing the satellites on a geostationary orbit. However, because this particular arrangement is itself time-invariant, it is not particularly useful in demonstrating the algorithm's capability for addressing time-varying problems. Instead, consider an alternate arrangement where the constellation is composed of satellites placed across four smaller identical orbits, equally distributed in periapsis direction. Unlike previous examples, the satellites are no longer equally distributed within each orbit, and are instead equally distributed within a range in mean anomaly. The positioning (mean anomaly at epoch) of each group is prescribed such that apoapsis of the center of each satellite group occurs as the target region is centered above apoapsis of each orbit. In order to maintain this synchronization, the time period (and thus semi-major axis) of the orbits is prescribed to revisit geostationary altitude an integer number of times per day (twice daily in this example).

The objective in this example is to minimize the satellite sensor range, i.e. determine the smallest sensor range capable of covering the target region continuously. The problem is subsequently posed as a non-linear programming (NLP) problem, where all integer parameters are prescribed, and approached using the interior-point solver in *fmincon*.[8] The decision variables are satellite sensor range, R, orbit eccentricity e, and satellite group spread, ΔM. Problem parameters are summarized in Table 11.

Table 11: Example 6 – Parameters

| Parameter	Description	Value
h_t	tangent height	100 km
h_l	lower target altitude	41164.13 km
h_u	upper target altitude	43164.13 km
λ_l	western target longitude	148°W
λ_u	eastern target longitude	61°W
k	number of distinct orbits in constellation	4 orbits
n	total constellation population	8 satellites
m	initial polygon resolution	100 PPC

Table 12: Example 6 – Start Point & Solution

Decision Variable	Description	Start Point	Solution
R	omni-directional sensor range	12000 km	17444 km
e	orbit eccentricity	0.50	0.40
ΔM	group spread	90° km	89.4°

Table 12 shows the infeasible start point and solution, obtained after 32 iterations. The start point and solution constellations are shown in Figures 20a and 20b respectively. Although the number of satellites in each orbit and the constellation as a whole remain fixed, this example demonstrates how the numerical ATH coverage model may be used in an NLP-driven constellation design process.

31
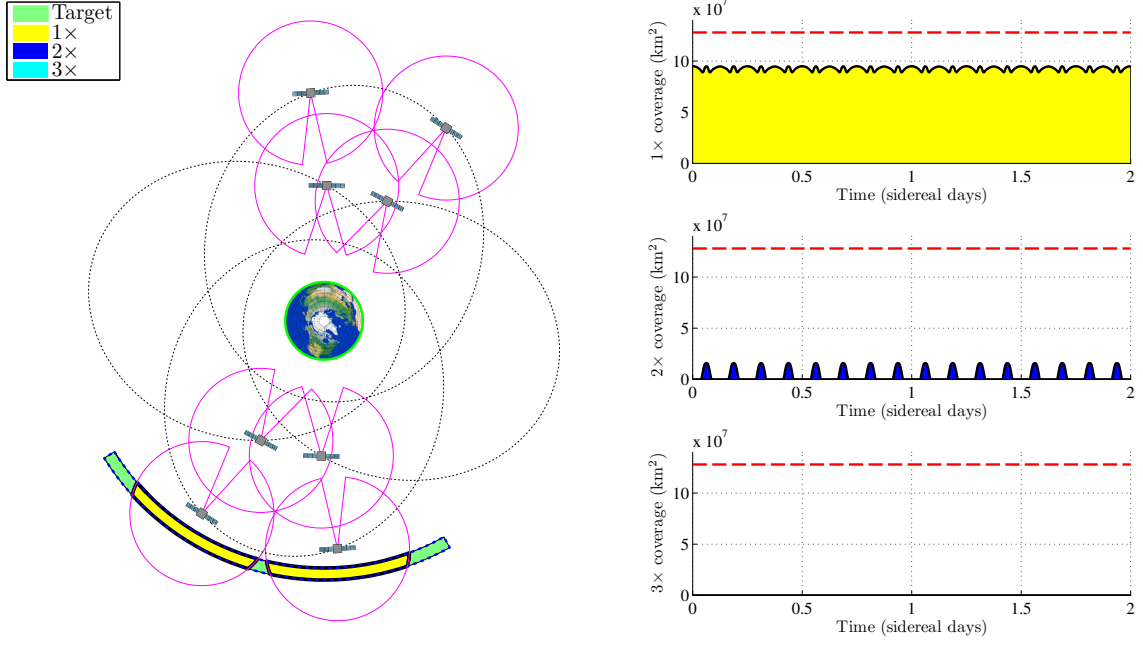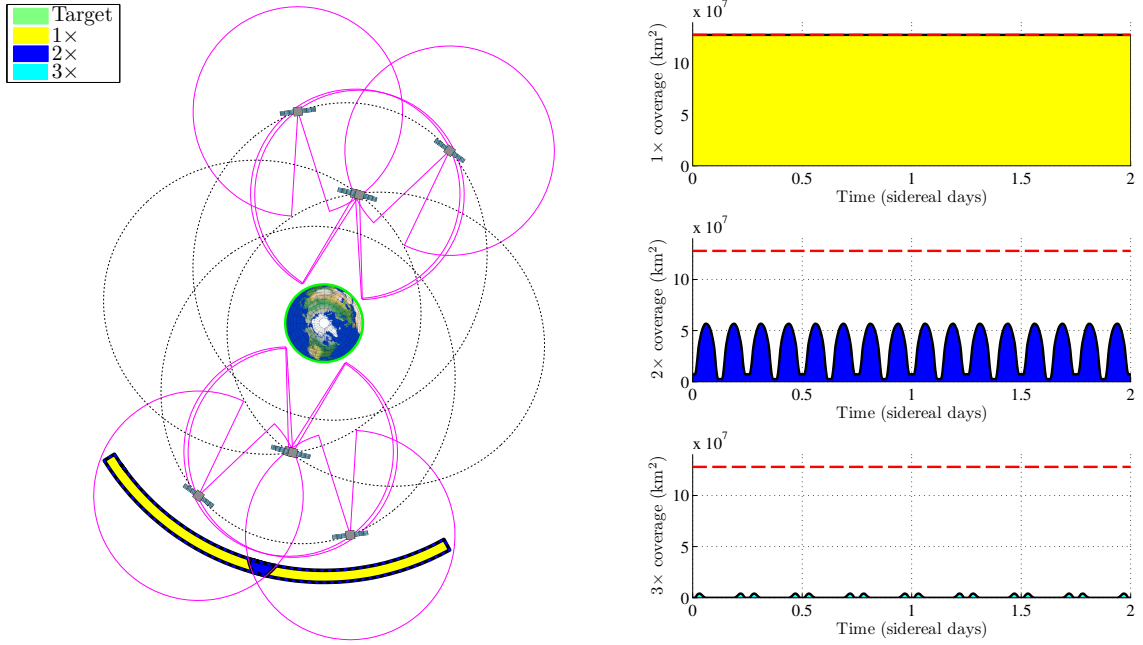
(a) Start Point

(b) Solution

Figure 20: Example 6 – Start point to solution with continuous 1× coverage constraint (see accompanying video #2)

6 Non-Planar Constellation Analysis

Volumetric coverage analysis for potentially non-planar constellations is accomplished by extending the previously described planar analysis code. When considering satellites in non-coplanar orbits, there is no single cross-sectional plane to compute planar coverage area within. Consequently, the coverage area in any one plane has no correlation to the coverage volume of a given non-coplanar constellation. To directly analyze volumetric coverage, the planar analysis code analyzes coverage area of sensor and target region cross-sections within a finite set of equally spaced planes offset from a prescribed analysis plane (i.e. the xy plane in an Earth-centered inertial reference frame). When coverage area in each plane is determined, it is multiplied by the distance between the offset planes, resulting in an approximate volume for a particular 'cutting plane' of constellation coverage. The sum of these 'cutting plane' volumes is the approximate coverage volume for the entire constellation. The accuracy of the coverage volume approximation is directly proportional to 'cutting plane' density over the region covered by the constellation.

The fundamental challenge in analyzing volumetric coverage of constellations then becomes cross-section determination of sensor and target regions. Omni-directional sensor profiles are considered in the present investigation, although this approach may be used for any sensor profile, provided a means exists to generate cross-sections at arbitrary orientations to the profile.

In this section the methods by which target region cross-sections and ATH sensor cross-sections are obtained for the omni-directional sensor case are developed. These results are applied to example problems in the next section, demonstrating volumetric coverage analysis capability for the omni-directional sensor, non-coplanar orbit case.

6.1 ATH Sensor Coverage Cross-Section Generation

Figure 21 shows several representative cross-sections of an approximated omni-directional sensor coverage volume. The red dot indicates the location of the satellite, and the missing section is the tangent height cone (THC) – the region of the omni-directional volume that is below the horizon, or against an Earth background.
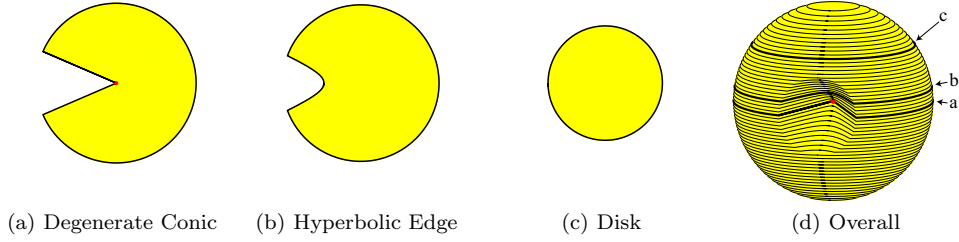

<div align="center">
(a) Degenerate Conic   (b) Hyperbolic Edge   (c) Disk   (d) Overall
</div>

Figure 21: Offset cross-sections of the sensor coverage volume

Figure 21a shows the familiar sensor region cross-section seen in prior planar constellation investigations. The 'cutting plane' intersects the position of the satellite and the axis of the THC (the satellite position vector), creating a boundary composed of a circular arc and a degenerate conic section. Figure 21b shows a cross-section composed of a circular arc and a hyperbolic conic section, while Figure 21c shows a disk cross-section, not intersecting the THC.

To analyze constellations composed of satellites in non-coplanar orbits, sensor coverage volume cross-sections must be available for any 'cutting plane' angle, ϕ. The cutting plane angle refers to the acute angle between the satellite position vector and the cross-section plane and is bounded by $-\pi/2 \leq \phi \leq \pi/2$. Note that $\phi = 0$ in the case shown in Figure 21. Figure 22 shows a more general case with a positive ϕ, featuring cross-sections composed of circular arcs and hyperbolic conic sections.

<div align="center">
(a) Hyperbolic Edge   (b) Degenerate Conic   (c) Hyperbolic Edge   (d) Disk   (e) Overall
</div>
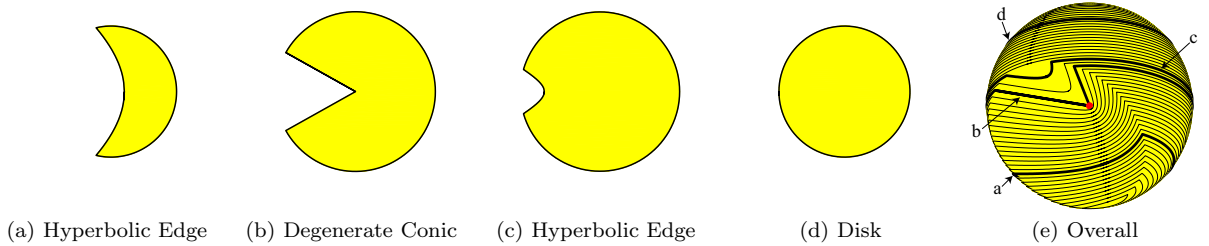
Figure 22: Offset cross-sections of the sensor coverage volume for a non-zero cutting plane angle

For the omni-directional sensor coverage case, given an omni-directional sensor range, satellite position, and tangent height, vertices outlining cross-sections of the ATH sensor coverage volume may be determined in closed form by solving various geometrically obtained equations.

The eccentricity of the THC conic section at cutting plane ϕ may be computed by the relation

$$e = \frac{\cos |\phi|}{cos\gamma}, \tag{16}$$

where γ is the interior half-angle of the THC. The radius of the base of the THC truncated at the intersection of the THC and sensor radius (i.e. the 'edge' of the missing region in Figures 21d and 22e) is given by

$$m = R \sin \gamma. \tag{17}$$

<div align="center">34</div>

The eccentricity of the THC conic section is used to identify different cases by which cross-sections of the omni-directional ATH coverage region are determined. For $0 \leq e < 1 - n\varepsilon$, the cross-sections are either disks, or compound regions composed of circular and elliptical arcs. For $1 - n\varepsilon \leq e \leq 1 + n\varepsilon$, the cross-sections are either disks, or compound regions composed of circular and parabolic arcs. For $e \geq 1 + n\varepsilon$, the cross-sections are either disks or compound regions composed of circular and hyperbolic arcs. Degenerate conics result when the cutting plane passes through the satellite position (apex of the THC). This occurs when the cutting plane offset, h, is zero. Note that in the implementation degenerate and non-existent cases are tested for first in order to simplify the logical structure of the proceeding code. Thus, the degenerate and non-existent cases, **D** and **E** are presented prior to cases **A-C**.

The conditions for a parabolic conic section of the THC are modified with respect to classical analytical consideration for numerical reasons. In practice, on a finite precision computing platform, the near-parabolic hyperbolic or elliptical conic sections are difficult to compute accurately due to the discontinuity in several of the conic section parameters in the neighborhood of $e = 1$. For this reason, an expanded parabolic interval of $\pm n\varepsilon$ is implemented, where near-parabolic conic sections are assumed to be parabolic and are determined by relationships derived for the parabolic case. The parameter ε is the 'machine epsilon' for the computer platform being used, and represents the distance to the nearest number to 1 that is differentiable by the system from 1. n is a parameter that is determined by experimentation to encompass the region of inaccuracy surrounding $e = 1$, and is assumed to be 1×10^8 in the current study.

The rest of this section documents the geometric relationships necessary to define the omni-directional sensor cross-sections at arbitrary cutting plane angles. This capability is necessary for generalized volumetric ATH coverage computation using the volumetric layering approximation method investigated in this study. The cross-sections are derived in a Cartesian coordinate system $(\hat{x}\hat{y}\hat{z})$ such that the analysis plane is parallel to the $x - y$ plane in the general problem, the $\hat{z}$ axis is parallel to the z axis in the general problem, and the $\hat{x}$ axis points toward the Earth parallel to the projection of the satellite position vector into the $\hat{x} - \hat{y}$ plane. Transformation from the $\hat{x}\hat{y}\hat{z}$ frame back to the xyz frame of the general problem is discussed at the end of this section.

6.1.1 Case D: $h = 0$

When the cutting plane intersects the satellite location (the apex of the THC), a degenerate conic results. This conic section is either a single point, a line that encompass zero area (in which case the sensor cross-section is regarded as a disk), or a triangular region bounded by two lines intersecting at the apex (resulting in a sensor cross-section resembling the in-plane planar case cross-sections of previous discussion). Cutting plane positions leading to this case are shown in Figure 23. The associated cutting-plane cross-sections of the ATH coverage volumes in Figure 23 are shown in Figure 24.
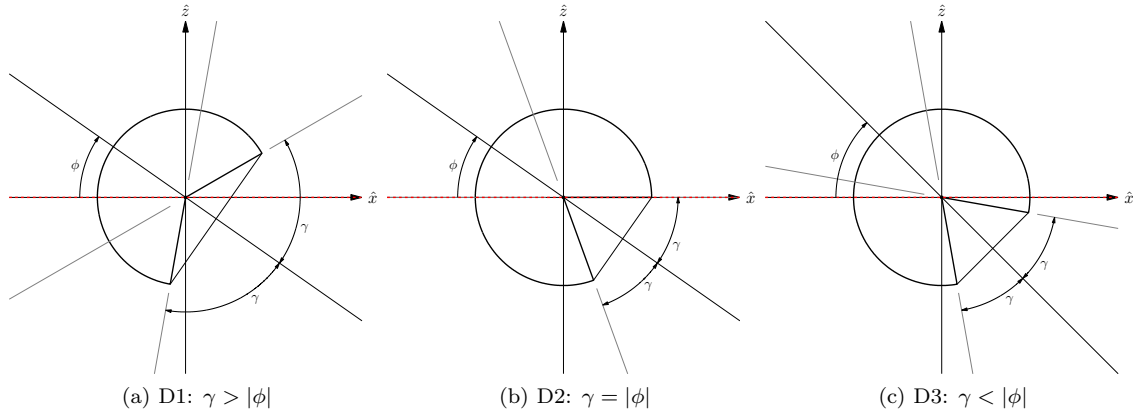

(a) D1: $\gamma > |\phi|$ (b) D2: $\gamma = |\phi|$ (c) D3: $\gamma < |\phi|$

Figure 23: Case D

(a) D1: $\gamma > |\phi|$ (b) D2: $\gamma = |\phi|$ (c) D3: $\gamma < |\phi|$
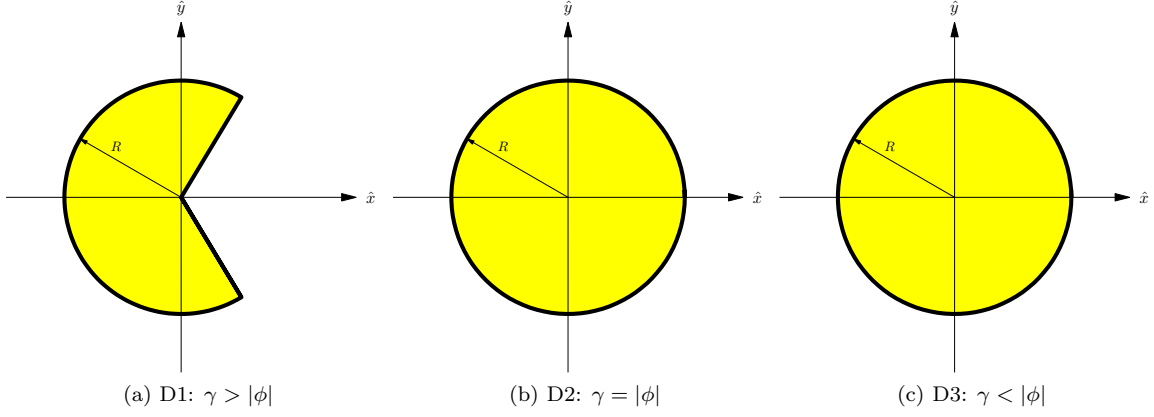
Figure 24: Case D

Case D1: $\gamma > |\phi|$ The degenerate conic section is bounded by two lines intersecting at the satellite, separated by the interior half angle

$$\gamma' = \cos^{-1}\left(\frac{\cos\gamma}{\cos|\phi|}\right). \tag{18}$$

The circular portion, spanned clockwise is bounded by the angles

$$\psi_i = 2\pi - \gamma', \psi_f = \gamma' \tag{19}$$

as measured in the cutting plane from the $\hat{x}$ direction.

Thus, the cross-section is a disk of radius R missing a $2\gamma'$ wide sector, as shown in Figure 24a.

Cases D2, D3: $\gamma = |\phi|$ **or** $\gamma < |\phi|$ The cutting plane does not intersect the interior of the THC, thus the conic section of the THC is a point or a line with zero area. The sensor cross-section is assumed with no loss of accuracy to be a disk of radius R, as shown in Figures 24b and 24c.

6.1.2   Case E: $|h| \geq R$

The cutting plane lies outside the radius of the omni-directional sensor volume, thus the cross-section does not exist. Figure 25 shows cutting plane offsets (h) leading to this case. The associated cross-sections do not exist, thus, they are not shown.

6.1.3   Case A1: $e > 1 + n\varepsilon$ **and** $\phi \geq 0$

The THC cross-section is strictly hyperbolic, thus, sensor region cross-sections may be disks, non-existent, or defined by a compound boundary between a circular arc and a hyperbola. Excluding the cases where the cross-section is determined to be a disk, the problem is determining the hyperbolic parameters a and b in the canonical form of a hyperbola, and determining the center-point of the conic-section, s'. s' is centered between the 'first point,' p_1, of the THC conic section, and the 'first point' of the imaginary rear-half of the THC, q_1. 'First point' refers to the closest point on each hyperbola to the center. By finding the location of a 'second point,' p_{2+}, where the conic section intersects the omni-directional sensor radius in the cutting plane, the appropriate angular intervals in ψ may be determined to define the hyperbolic and circular curves.

For the hyperbolic segments, the radius of the hyperbola with respect to the focus, f, located on the $\hat{x}$ axis at $x_{s'} + ae$, is given by

$$r_{\text{hyperbola}} = \frac{a(e^2 - 1)}{1 - e\cos\psi}. \tag{20}$$
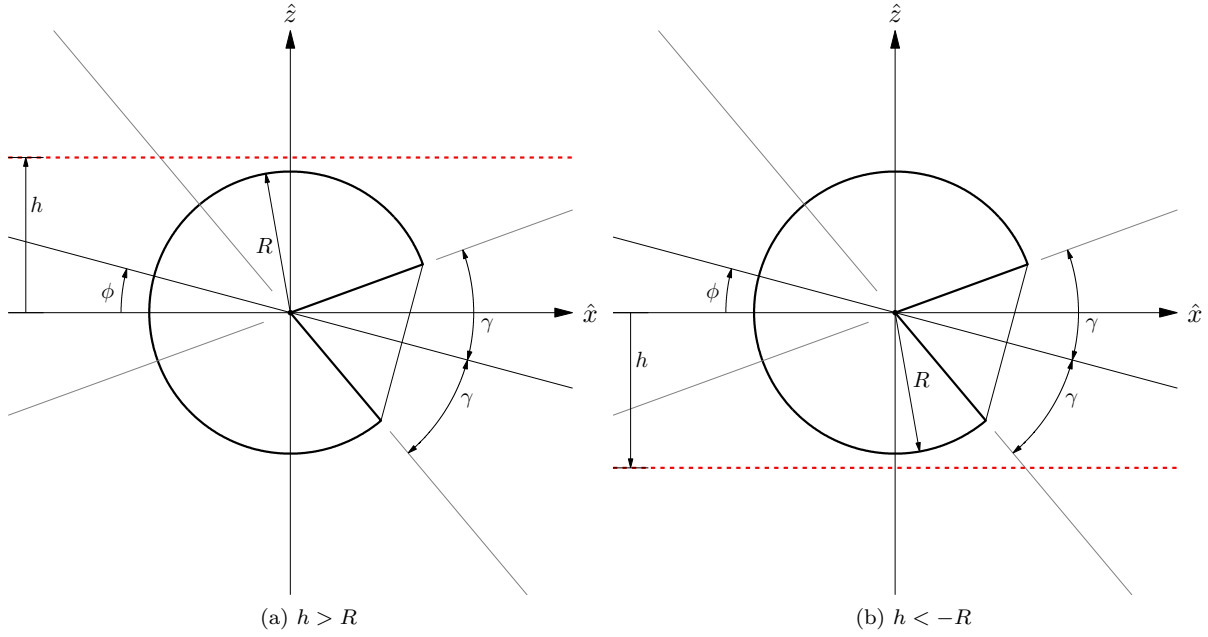
36

(a) $h > R$ (b) $h < -R$

Figure 25: Case E

The radius of the outer circular arc, bounding the omni-directional sensor radius in the ATH regions is given with respect to the origin by

$$r_{\text{circular arc}} = \sqrt{R^2 - h^2}. \tag{21}$$

Case A1A: $R > h$ **and** $h \geq R\sin(\gamma - |\phi|)$ The cutting plane lies above the upper intersection of the THC with the omni-directional sensor radius, leading to a disk-shaped sensor cross-section with radius $r_{\text{circular arc}}$.

Cutting plane positions leading to this case are shown in Figure 26. The associated cutting-plane cross-sections of the ATH coverage volumes in Figure 26 are shown in Figure 27.

Case A1B: $R\sin(\gamma - |\phi|) > h$ **and** $h > 0$ The cutting plane intersects the THC within the omni-directional sensor radius, leading to a sensor cross-section defined by a compound boundary between a circular arc and a hyperbola.

Cutting plane positions leading to this case are shown in Figure 28. The associated cutting-plane cross-sections of the ATH coverage volumes in Figure 28 are shown in Figure 29.

First, the coordinates of the 'first point' on the THC, p_1, are determined by

$$x_{p_1} = \begin{cases} 0 & : \gamma - |\phi| = \frac{\pi}{2} \\ \frac{|h|}{\tan(\gamma - |\phi|)} & : \gamma - |\phi| \neq \frac{\pi}{2} \end{cases}, \tag{22}$$

$$y_{p_1} = 0.$$

Similarly, the 'first point' on the THC, q_1 is determined by

$$x_{q_1} = \begin{cases} 0 & : \gamma + |\phi| = \frac{\pi}{2} \\ -\frac{|h|}{\tan(\gamma + |\phi|)} & : \gamma + |\phi| \neq \frac{\pi}{2} \end{cases}, \tag{23}$$

$$y_{q_1} = 0.$$

It can be shown by trigonometry then that using the intermediate values q and g, found by the relations

$$q = m - \left(R - \sqrt{h^2 + x_{p_1}^2}\right) \frac{\sin(\gamma - |\phi|)}{\cos|\phi|}, \tag{24}$$

37

(a) $|\phi| + \gamma < \pi/2$

(b) $|\phi| + \gamma > \pi/2$

Figure 26: Case A1A

(a) $|\phi| + \gamma < \pi/2$

(b) $|\phi| + \gamma > \pi/2$
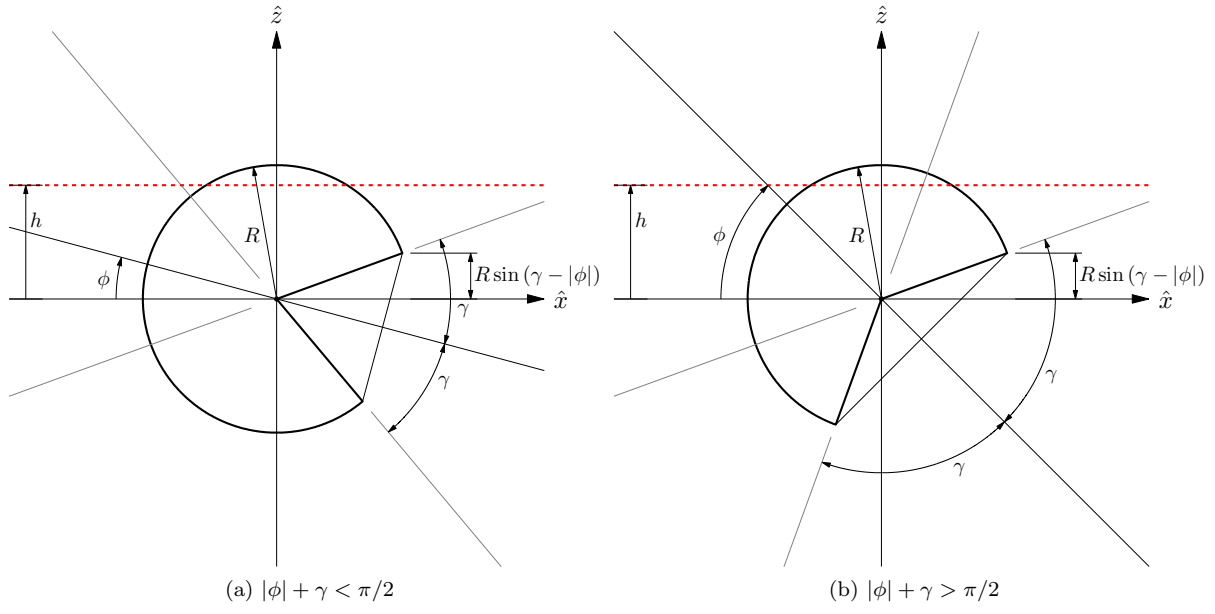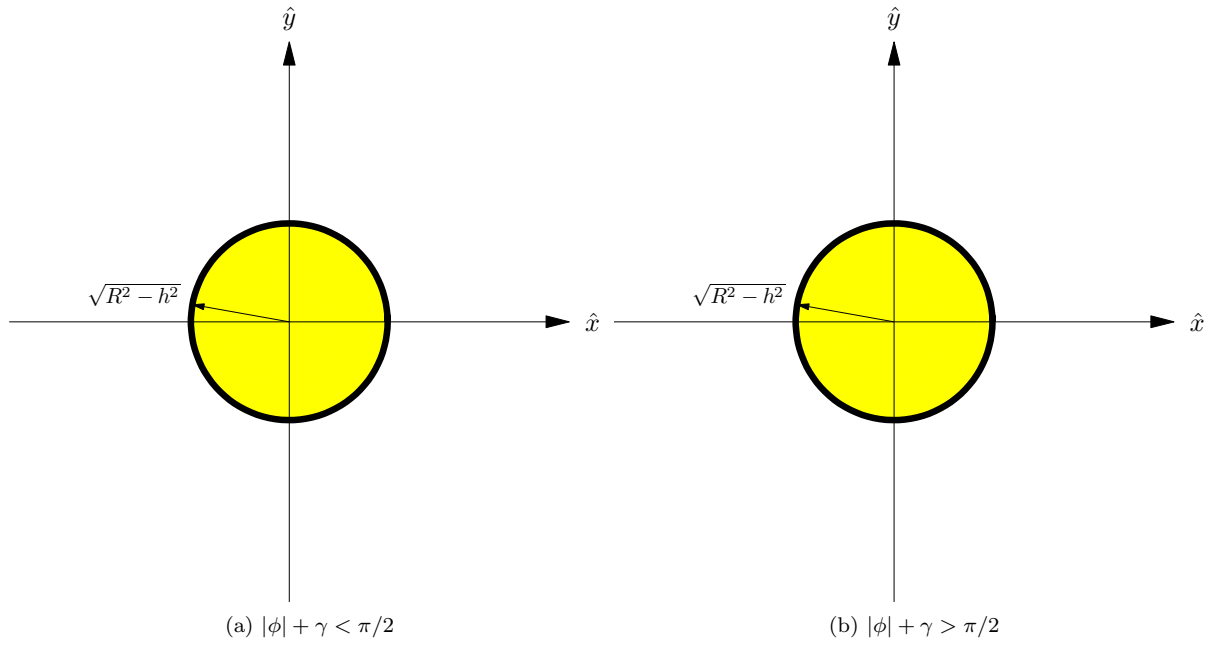
Figure 27: Case A1A

$$g = \left(R - \frac{h}{\sin\gamma - |\phi|} \right) \frac{\cos\gamma}{\cos|\phi|}, \tag{25}$$

the coordinates of the 'second point,' p_{2+}, can be determined by

$$x_{p_{2+}} = x_{p_1} + g,$$
$$y_{p_{2+}} = \sqrt{m^2 - q^2}. \tag{26}$$

It then follows that the hyperbolic parameters a, b, and $x_{s'}$ may be determined by

$$a = \frac{x_{p_1} - x_{q_1}}{2},$$
$$b = a\sqrt{e^2 - 1}, \tag{27}$$

$$x_{s'} = x_{p_1} - a. \tag{28}$$

In the implementation, the hyperbolic span is split into two regions, such that the initial point of the outer polygon boundary is at the satellite location. This is done for convenience in the implementation of visualization functions. The upper half of the hyperbola is thus spanned by the angles

$$\psi_i = \pi,$$
$$\psi_f = \arctan\left(\frac{y_{p_{2+}}}{x_{p_{2+}} - (x_s' + ae)} \right), \tag{29}$$

relative to the focus, f. The radius relative to f is determined using Equation 20. The circular arc, relative to the origin is spanned by

$$\psi_i = \arctan\left(\frac{y_{p_{2+}}}{x_{p_{2+}}} \right),$$
$$\psi_f = 2\pi - \arctan\left(\frac{y_{p_{2+}}}{x_{p_{2+}}} \right), \tag{30}$$

with a radius given by Equation 21. Finally, the lower half of the hyperbola is spanned by

$$\psi_i = -\arctan\left(\frac{y_{p_{2+}}}{x_{p_{2+}} - (x_s' + ae)} \right),$$
$$\psi_f = -\pi. \tag{31}$$

Case A1C: $0 > h$ **and** $h > -R\sin(\gamma + |\phi|)$ The cutting plane intersects the THC within the omni-directional sensor radius, leading to a sensor cross-section defined by a compound boundary between a circular arc and a hyperbola.

Cutting plane positions leading to this case are shown in Figure 30. The associated cutting-plane cross-sections of the ATH coverage volumes in Figure 30 are shown in Figure 31.

First, the coordinates of the 'first point' on the THC, p_1, are determined by

$$x_{p_1} = \begin{cases} 0 & : \gamma + |\phi| = \frac{\pi}{2} \\ \frac{|h|}{\tan(\gamma + |\phi|)} & : \gamma + |\phi| \neq \frac{\pi}{2} \end{cases}, \tag{32}$$
$$y_{p_1} = 0.$$

Similarly, the 'first point' on the THC, q_1 is determined by

$$x_{q_1} = \begin{cases} 0 & : \gamma - |\phi| = \frac{\pi}{2} \\ -\frac{|h|}{\tan(\gamma - |\phi|)} & : \gamma - |\phi| \neq \frac{\pi}{2} \end{cases}, \tag{33}$$
$$y_{q_1} = 0.$$

(a) $|\phi| + \gamma < \pi/2$

(b) $|\phi| + \gamma > \pi/2$

Figure 28: Case A1B

(a) $|\phi| + \gamma < \pi/2$
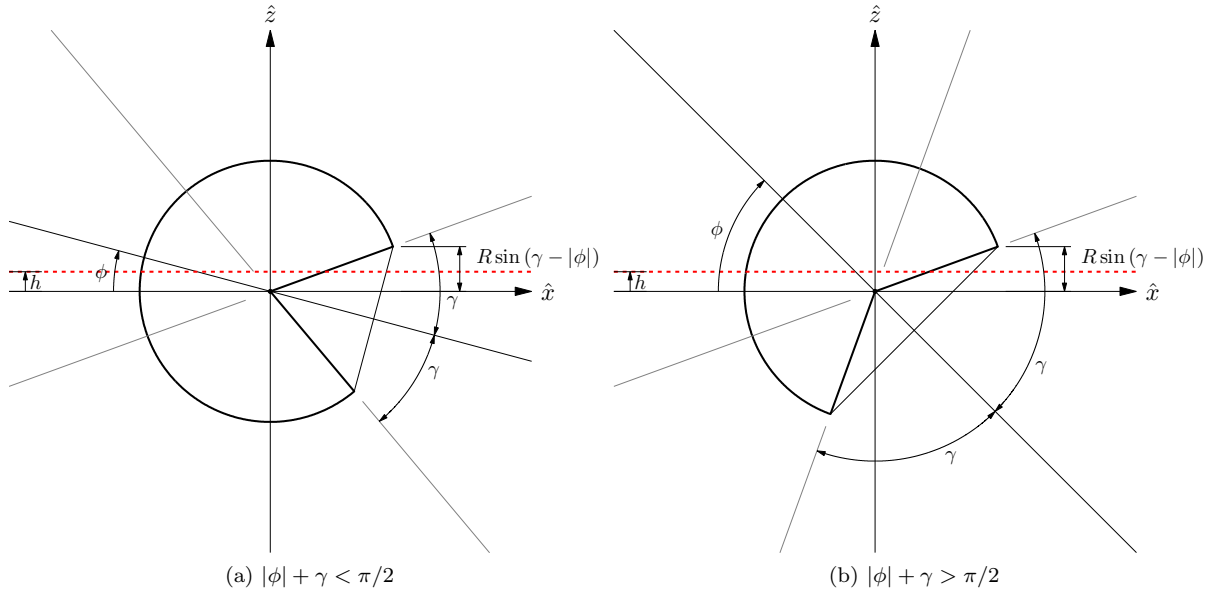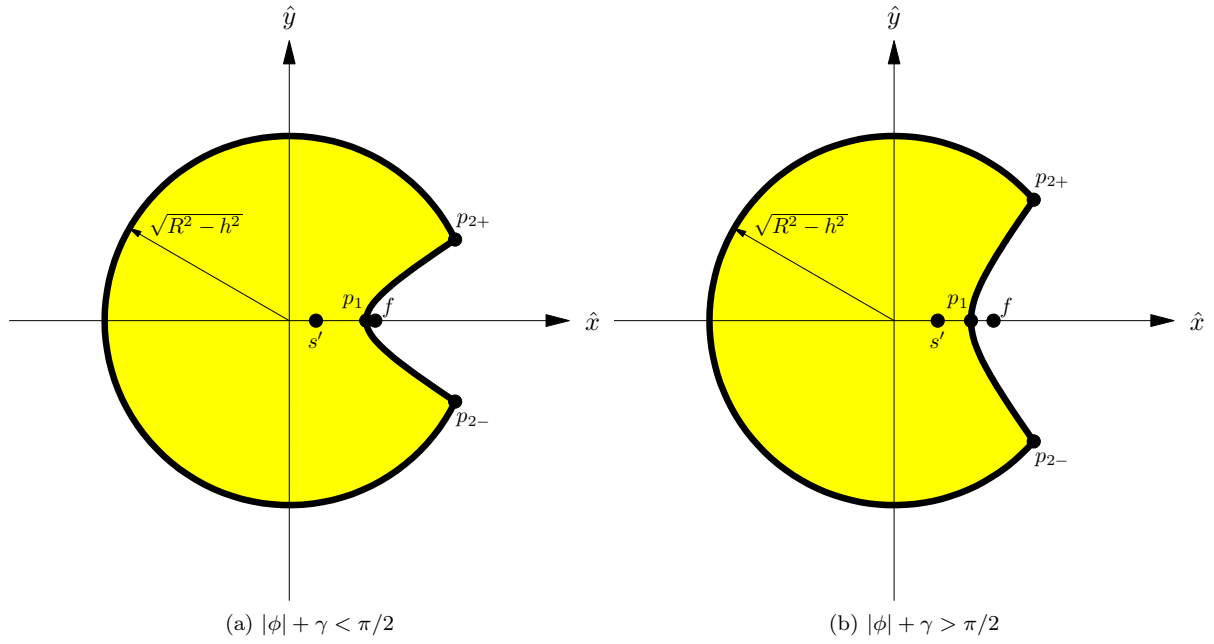
(b) $|\phi| + \gamma > \pi/2$

Figure 29: Case A1B

It can be shown by trigonometry then that using the intermediate values g and q, found by the relations

$$g = \left(R - \sqrt{h^2 + x_{p_1}^2}\right) \frac{\cos \gamma}{\cos |\phi|}, \tag{34}$$

$$q = \left| m - g \frac{\sin (|\phi| + \gamma)}{\cos \gamma} \right|, \tag{35}$$

the coordinates of the 'second point,' p_{2+}, can be determined by

$$\begin{aligned} x_{p_{2+}} &= x_{p_1} + g, \\ y_{p_{2+}} &= \sqrt{m^2 - q^2}. \end{aligned} \tag{36}$$

It then follows that the hyperbolic parameters a, b, and $x_{s'}$ may be determined by

$$\begin{aligned} a &= \frac{x_{p_1} - x_{q_1}}{2}, \\ b &= a\sqrt{e^2 - 1}, \end{aligned} \tag{37}$$

$$x_{s'} = x_{p_1} - a. \tag{38}$$

In the implementation, the hyperbolic span is split into two regions, such that the initial point of the outer polygon boundary is at the satellite location. This is done for convenience in the implementation of visualization functions. The upper half of the hyperbola is thus spanned by the angles

$$\begin{aligned} \psi_i &= \pi, \\ \psi_f &= \arctan\left(\frac{y_{p_{2+}}}{x_{p_{2+}} - (x_s' + ae)}\right), \end{aligned} \tag{39}$$

relative to the focus, f. The radius relative to f is determined using Equation 20. The circular arc, relative to the origin is spanned by

$$\begin{aligned} \psi_i &= \arctan\left(\frac{y_{p_{2+}}}{x_{p_{2+}}}\right), \\ \psi_f &= 2\pi - \arctan\left(\frac{y_{p_{2+}}}{x_{p_{2+}}}\right), \end{aligned} \tag{40}$$

with a radius given by Equation 21. Finally, the lower half of the hyperbola is spanned by

$$\begin{aligned} \psi_i &= -\arctan\left(\frac{y_{p_{2+}}}{x_{p_{2+}} - (x_s' + ae)}\right), \\ \psi_f &= -\pi. \end{aligned} \tag{41}$$

Case A1D: $-R\sin(|\phi| + \gamma) \geq h$ **and** $h > -R$ The cutting plane lies below the lower intersection of the THC with the omni-directional sensor radius leading to either a disk-shaped sensor cross-section with radius $r_{\text{circular arc}}$, or no region at all if $|\phi| + \gamma > \pi/2$.

Cutting plane positions leading to this case are shown in Figure 32. The associated cutting-plane cross-sections of the ATH coverage volumes in Figure 32 are shown in Figure 33.

6.1.4   Case A2: $e > 1 + n\varepsilon$ and $\phi < 0$

The THC cross-section is strictly hyperbolic, thus, sensor region cross-sections may be disks, non-existent, or defined by a compound boundary between a circular arc and a hyperbola. Excluding the cases where the cross-section is determined to be a disk, the problem is determining the hyperbolic parameters a and b in the canonical form of a hyperbola, and determining the center-point of the conic-section, s'. s' is centered between the 'first point,' p_1, of the THC conic section, and the 'first point' of the imaginary rear-half of the
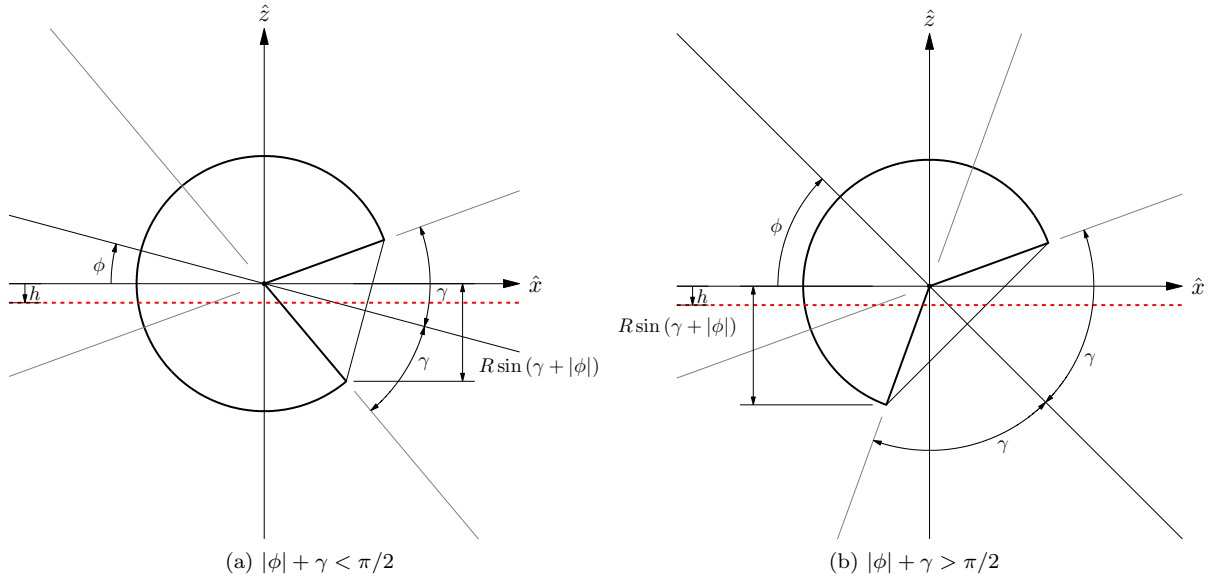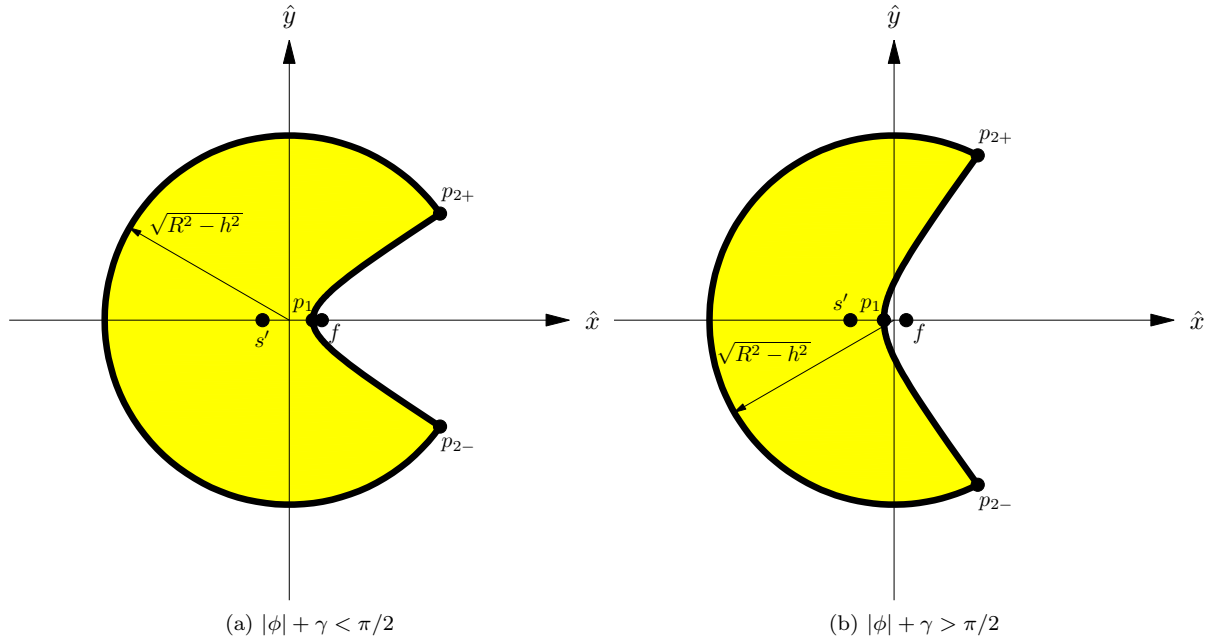
41

(a) $|\phi| + \gamma < \pi/2$

(b) $|\phi| + \gamma > \pi/2$

Figure 30: Case A1C

(a) $|\phi| + \gamma < \pi/2$

(b) $|\phi| + \gamma > \pi/2$

Figure 31: Case A1C

(a) $|\phi| + \gamma < \pi/2$ (b) $|\phi| + \gamma > \pi/2$

Figure 32: Case A1D
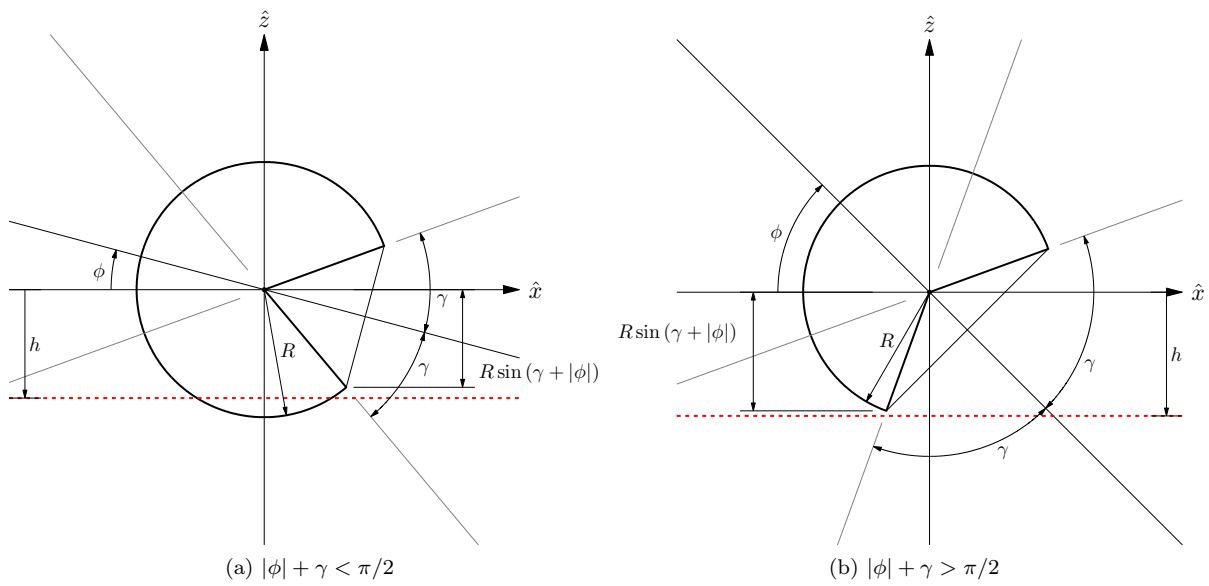

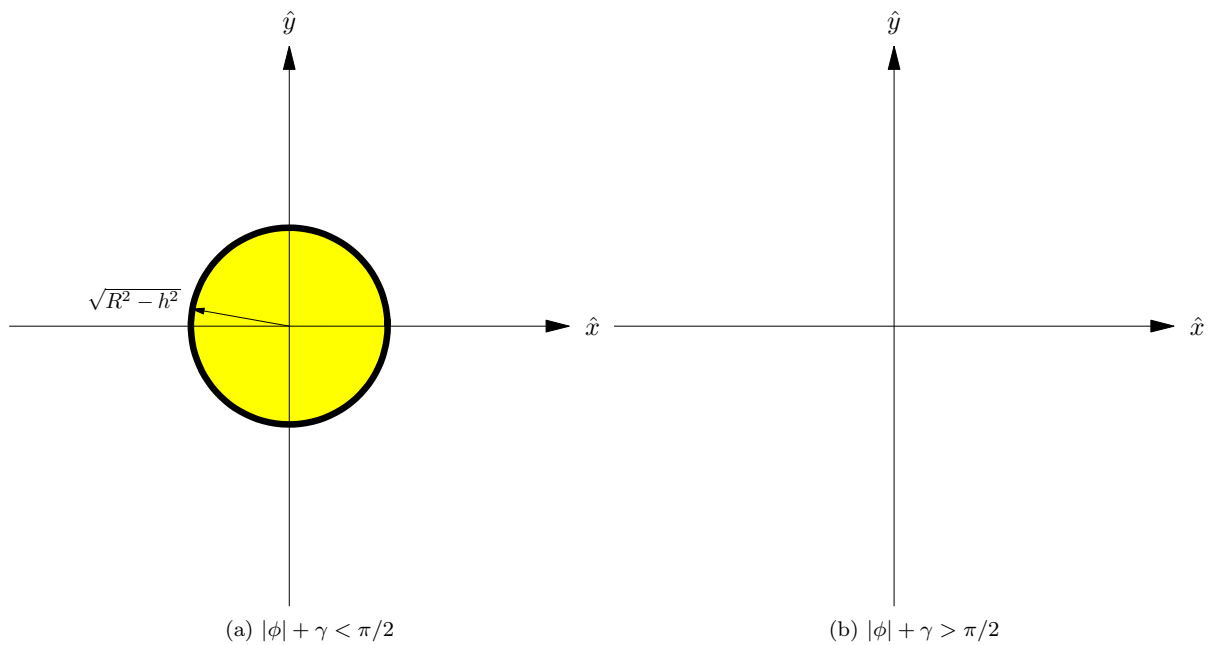(a) $|\phi| + \gamma < \pi/2$ (b) $|\phi| + \gamma > \pi/2$

Figure 33: Case A1D

43

THC, q_1. 'First point' refers to the closest point on each hyperbola to the center. By finding the location of a 'second point,' p_{2+}, where the conic section intersects the omni-directional sensor radius in the cutting plane, the appropriate angular intervals in ψ may be determined to define the hyperbolic and circular curves.

For the hyperbolic segments, the radius of the hyperbola with respect to the focus, f, located on the $\hat{x}$ axis at $x_{s'} + ae$, is given by

$$r_{\text{hyperbola}} = \frac{a(e^2 - 1)}{1 - e\cos\psi} \tag{42}$$

The radius of the outer circular arc, bounding the omni-directional sensor radius in the ATH regions is given with respect to the origin by

$$r_{\text{circular arc}} = \sqrt{R^2 - h^2}. \tag{43}$$

Case A2A: $R > h$ **and** $h \geq R\sin(\gamma + |\phi|)$ The cutting plane lies above the upper intersection of the THC with the omni-directional sensor radius leading to either a disk-shaped sensor cross-section with radius $r_{\text{circular arc}}$, or no region at all if $|\phi| + \gamma > \pi/2$.

Cutting plane positions leading to this case are shown in Figure 34. The associated cutting-plane cross-sections of the ATH coverage volumes in Figure 34 are shown in Figure 35.

(a) $|\phi| + \gamma < \pi/2$ (b) $|\phi| + \gamma > \pi/2$
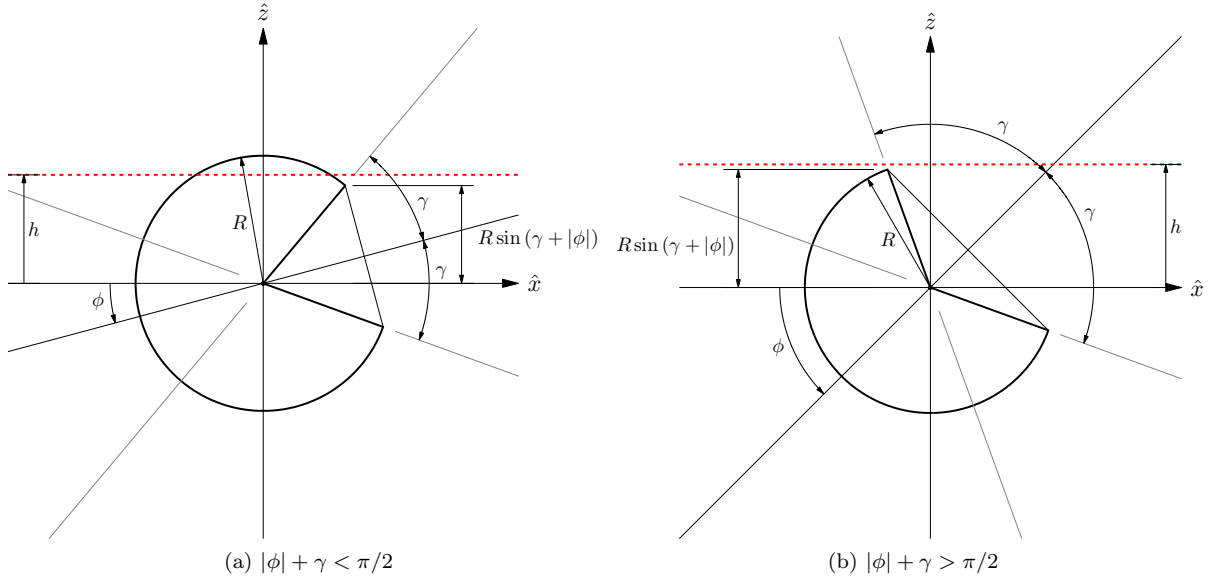
Figure 34: Case A2A

Case A2B: $R\sin(\gamma + |\phi|) > h$ **and** $h > 0$ The cutting plane intersects the THC within the omni-directional sensor radius, leading to a sensor cross-section defined by a compound boundary between a circular arc and a hyperbola.

Cutting plane positions leading to this case are shown in Figure 36. The associated cutting-plane cross-sections of the ATH coverage volumes in Figure 36 are shown in Figure 37.

First, the coordinates of the 'first point' on the THC, p_1, are determined by

$$x_{p_1} = \begin{cases} 0 & : \gamma + |\phi| = \frac{\pi}{2} \\ \frac{|h|}{\tan(\gamma + |\phi|)} & : \gamma + |\phi| \neq \frac{\pi}{2} \end{cases}, \tag{44}$$

$$y_{p_1} = 0.$$

44

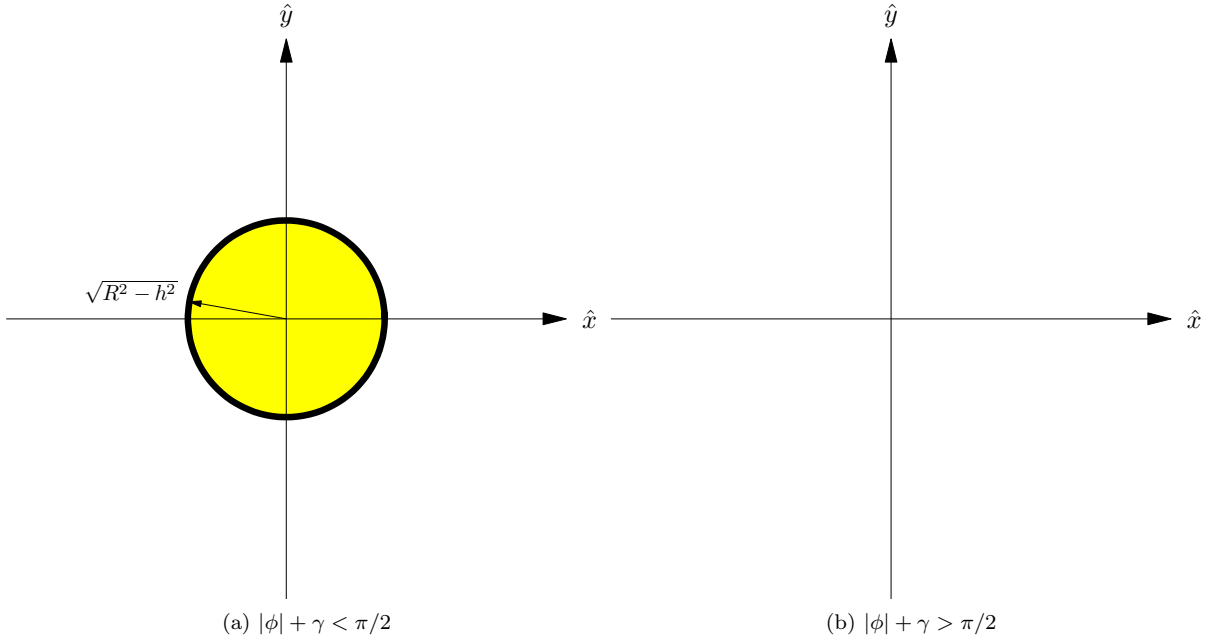(a) $|\phi| + \gamma < \pi/2$ (b) $|\phi| + \gamma > \pi/2$

Figure 35: Case A2A

Similarly, the 'first point' on the THC, q_1 is determined by

$$
x_{q_1} = \begin{cases} 0 & : \gamma - |\phi| = \frac{\pi}{2} \\ -\frac{|h|}{\tan(\gamma - |\phi|)} & : \gamma - |\phi| \neq \frac{\pi}{2} \end{cases},
\tag{45}
$$

$$
y_{q_1} = 0.
$$

It can be shown by trigonometry then that using the intermediate value g, found by the relation

$$
g = \left(R - \sqrt{h^2 + x_{p_1}^2} \right) \frac{\cos\gamma}{\cos|\phi|},
\tag{46}
$$

the coordinates of the 'second point,' p_{2+}, and the intermediate value q can be determined by

$$
x_{p_{2+}} = x_{p_1} + g,
$$

$$
q = \left| x_{p_{2+}} - \frac{|h|}{\tan|\phi|} \right| \sin|\phi|,
\tag{47}
$$

$$
y_{p_{2+}} = \sqrt{m^2 - q^2}.
$$

It then follows that the hyperbolic parameters a, b, and $x_{s'}$ may be determined by

$$
a = \frac{x_{p_1} - x_{q_1}}{2},
$$

$$
b = a\sqrt{e^2 - 1},
\tag{48}
$$

$$
x_{s'} = x_{p_1} - a.
\tag{49}
$$

In the implementation, the hyperbolic span is split into two regions, such that the initial point of the outer polygon boundary is at the satellite location. This is done for convenience in the implementation of visualization functions. The upper half of the hyperbola is thus spanned by the angles

$$
\psi_i = \pi,
$$

$$
\psi_f = \arctan\left(\frac{y_{p_{2+}}}{x_{p_{2+}} - (x'_s + ae)} \right),
\tag{50}
$$

relative to the focus, f. The radius relative to f is determined using Equation 42. The circular arc, relative to the origin is spanned by

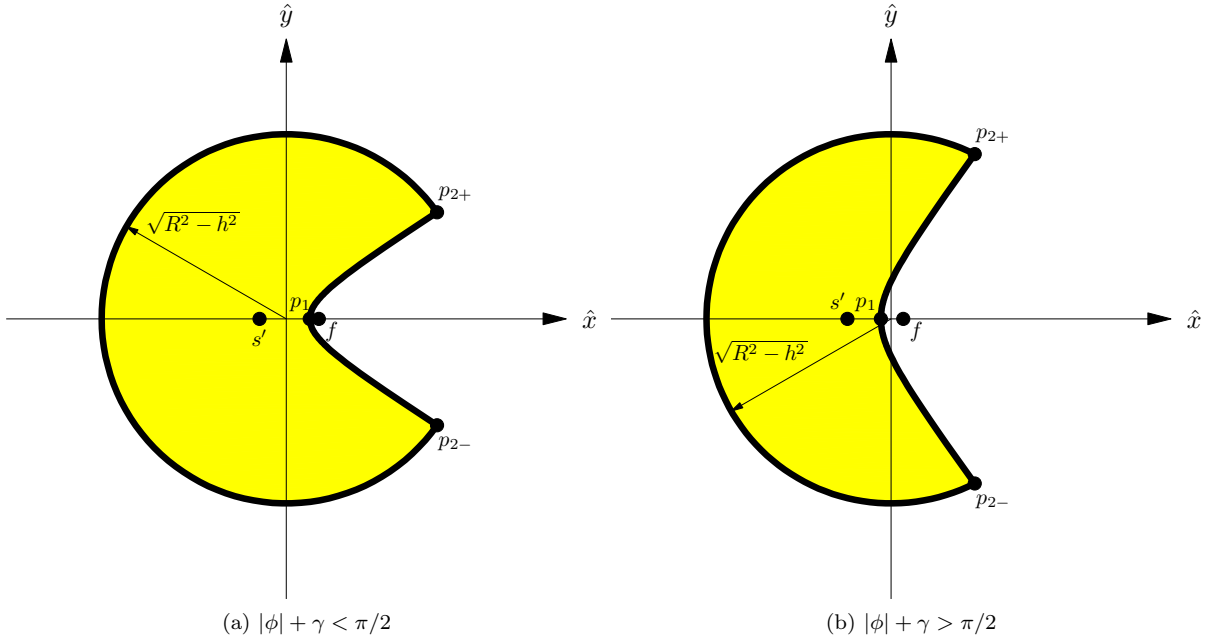$$\psi_i = \arctan\left(\frac{y_{p_{2+}}}{x_{p_{2+}}}\right),$$
$$\psi_f = 2\pi - \arctan\left(\frac{y_{p_{2+}}}{x_{p_{2+}}}\right), \tag{51}$$

with a radius given by Equation 43. Finally, the lower half of the hyperbola is spanned by

$$\psi_i = -\arctan\left(\frac{y_{p_{2+}}}{x_{p_{2+}} - (x'_s + ae)}\right),$$
$$\psi_f = -\pi. \tag{52}$$

(a) $|\phi| + \gamma < \pi/2$ (b) $|\phi| + \gamma > \pi/2$

Figure 36: Case A2B

Case A2C: $0 > h$ **and** $h > -R\sin(\gamma + |\phi|)$ The cutting plane intersects the THC within the omni-directional sensor radius, leading to a sensor cross-section defined by a compound boundary between a circular arc and a hyperbola.

Cutting plane positions leading to this case are shown in Figure 38. The associated cutting-plane cross-sections of the ATH coverage volumes in Figure 38 are shown in Figure 39.

First, the coordinates of the 'first point' on the THC, p_1, are determined by

$$x_{p_1} = \begin{cases} 0 & : \gamma - |\phi| = \frac{\pi}{2} \\ \frac{|h|}{\tan(\gamma - |\phi|)} & : \gamma - |\phi| \neq \frac{\pi}{2} \end{cases}, \tag{53}$$
$$y_{p_1} = 0.$$

Similarly, the 'first point' on the THC, q_1 is determined by

$$x_{q_1} = \begin{cases} 0 & : \gamma + |\phi| = \frac{\pi}{2} \\ -\frac{|h|}{\tan(\gamma + |\phi|)} & : \gamma + |\phi| \neq \frac{\pi}{2} \end{cases}, \tag{54}$$
$$y_{q_1} = 0.$$

46

(a) $|\phi| + \gamma < \pi/2$ (b) $|\phi| + \gamma > \pi/2$

Figure 37: Case A2B

It can be shown by trigonometry then that using the intermediate values q and g, found by the relations

$$g = \left(R - \sqrt{h^2 + x_{p_1}^2}\right) \frac{\cos\gamma}{\cos|\phi|},$$

$$q = m - \left(R - \sqrt{h^2 + x_{p_1}^2}\right) \frac{\sin\left(\gamma - |\phi|\right)}{\cos|\phi|},$$

$$(55)$$

the coordinates of the 'second point,' p_{2+}, can be determined by

$$x_{p_{2+}} = x_{p_1} + g.$$

$$y_{p_{2+}} = \sqrt{m^2 - q^2}.$$

$$(56)$$

It then follows that the hyperbolic parameters a, b, and $x_{s'}$ may be determined by

$$a = \frac{x_{p_1} - x_{q_1}}{2},$$

$$b = a\sqrt{e^2 - 1},$$

$$(57)$$

$$x_{s'} = x_{p_1} - a.$$

$$(58)$$

In the implementation, the hyperbolic span is split into two regions, such that the initial point of the outer polygon boundary is at the satellite location. This is done for convenience in the implementation of visualization functions. The upper half of the hyperbola is thus spanned by the angles

$$\psi_i = \pi,$$

$$\psi_f = \arctan\left(\frac{y_{p_{2+}}}{x_{p_{2+}} - (x'_s + ae)}\right),$$

$$(59)$$

relative to the focus, f. The radius relative to f is determined using Equation 42. The circular arc, relative

to the origin is spanned by

$$\psi_i = \arctan\left(\frac{y_{p_{2+}}}{x_{p_{2+}}}\right),$$

$$\psi_f = 2\pi - \arctan\left(\frac{y_{p_{2+}}}{x_{p_{2+}}}\right),$$

(60)

with a radius given by Equation 43. Finally, the lower half of the hyperbola is spanned by

$$\psi_i = -\arctan\left(\frac{y_{p_{2+}}}{x_{p_{2+}} - (x'_s + ae)}\right),$$

$$\psi_f = -\pi.$$

(61)

(a) $|\phi| + \gamma < \pi/2$ (b) $|\phi| + \gamma > \pi/2$

Figure 38: Case A2C

Case A2D: $-R\sin(\gamma + |\phi|) \geq h$ **and** $h > -R$ The cutting plane lies below the lower intersection of the THC with the omni-directional sensor radius, leading to a disk-shaped sensor cross-section with radius $r_{\text{circular arc}}$.

Cutting plane positions leading to this case are shown in Figure 40. The associated cutting-plane cross-sections of the ATH coverage volumes in Figure 40 are shown in Figure 41.

6.1.5   Case B1: $1 + n\varepsilon \geq e \geq 1 - n\varepsilon$ and $\phi > 0$

The THC cross-section is strictly parabolic, thus, sensor region cross-sections may be disks, non-existent, or defined by a compound boundary between a circular arc and a parabola. Excluding the cases where the cross-section is determined to be a disk, the problem is determining the parabolic parameter P in the canonical form of a parabola, and the 'first point,' p_1, of the THC conic section. 'First point' refers to the point on the parabola most negative in the $\hat{x}$ direction. By finding the location of a 'second point,' p_{2+}, where the conic section intersects the omni-directional sensor radius in the cutting plane, the appropriate angular intervals in ψ may be determined to define the hyperbolic and circular curves.
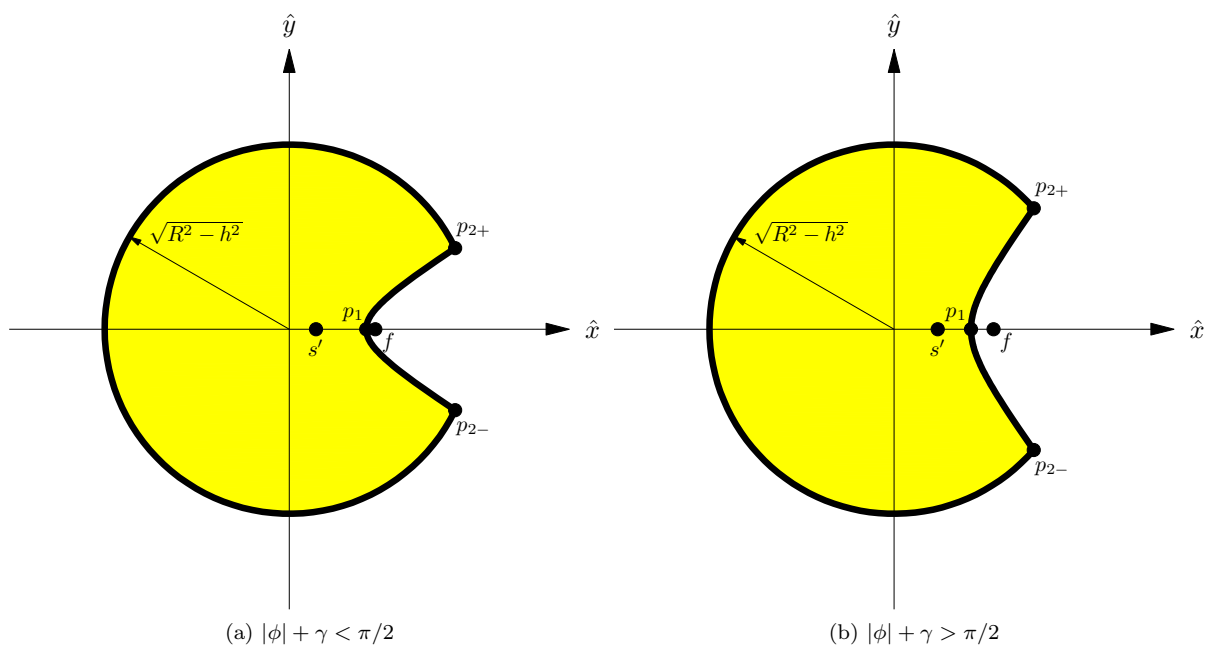
48

(a) $|\phi| + \gamma < \pi/2$ (b) $|\phi| + \gamma > \pi/2$

Figure 39: Case A2C

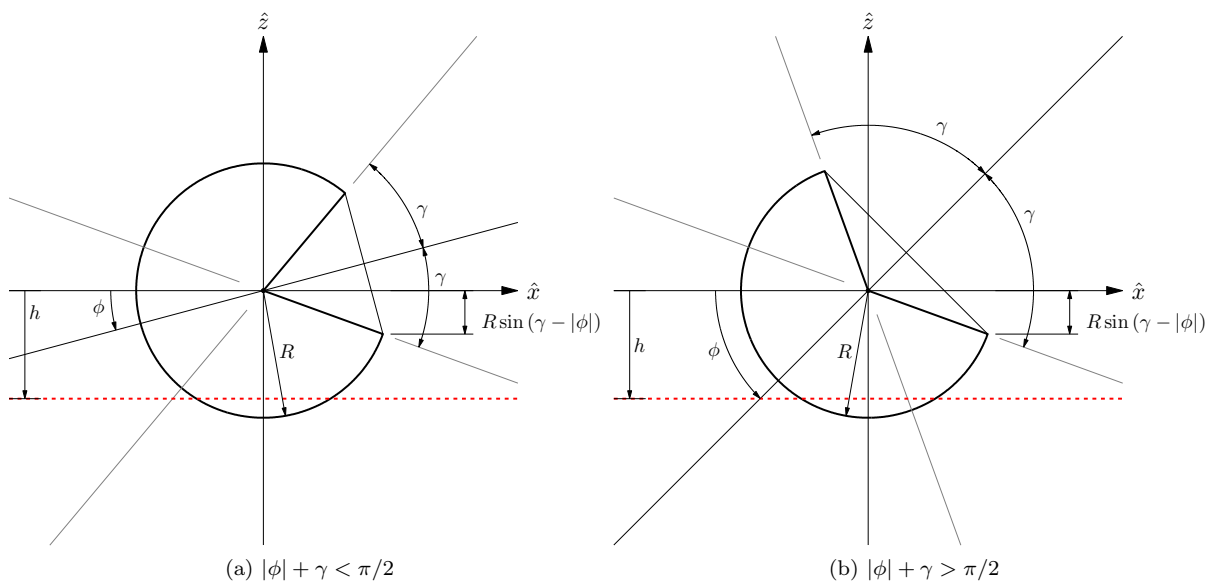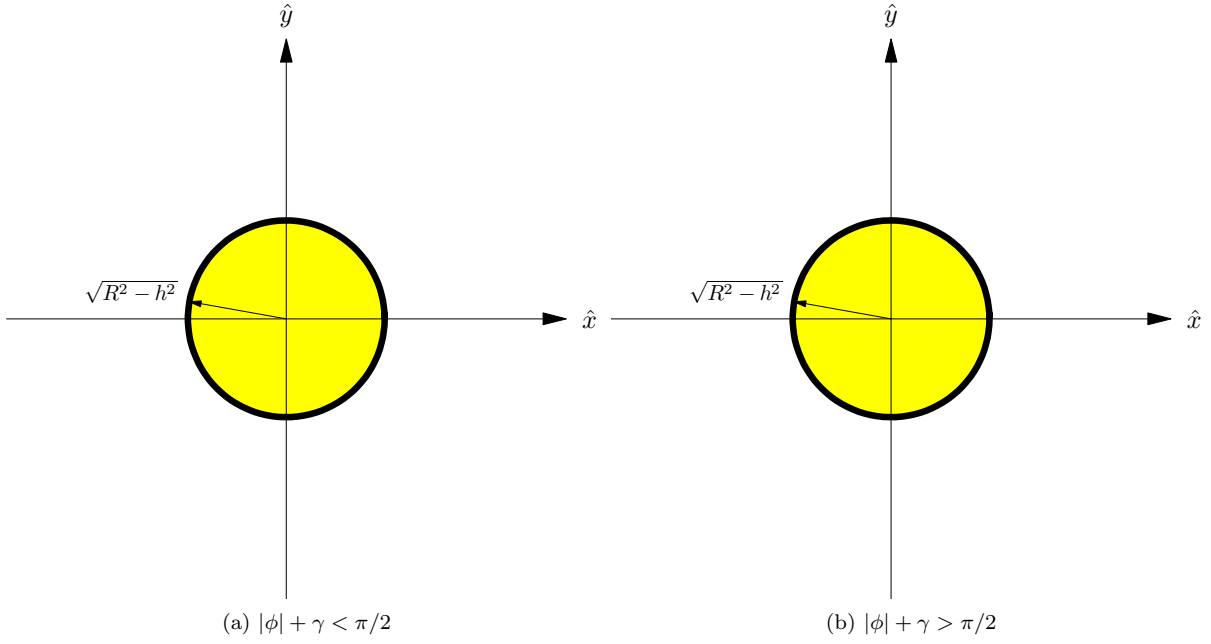(a) $|\phi| + \gamma < \pi/2$ (b) $|\phi| + \gamma > \pi/2$

Figure 40: Case A2D

Figure 41: Case A2D

For the parabolic segments, the radius of the parabola with respect to the focus, f, located on the $\hat{x}$ axis at $x_{p_1} + P$, is given by

$$r_{\text{parabola}} = \frac{2P}{1 - \cos\psi} \tag{62}$$

The radius of the outer circular arc, bounding the omni-directional sensor radius in the ATH regions is given with respect to the origin by

$$r_{\text{circular arc}} = \sqrt{R^2 - h^2}. \tag{63}$$

Case B1A: $R > h$ **and** $h \geq 0$ The cutting plane lies above the upper intersection of the THC with the omni-directional sensor radius, leading to a disk-shaped sensor cross-section with radius $r_{\text{circular arc}}$.

Cutting plane positions leading to this case are shown in Figure 42. The associated cutting-plane cross-sections of the ATH coverage volumes in Figure 42 are shown in Figure 43.

Case B1B: $0 > h$ **and** $h > -R\sin 2\gamma$ The cutting plane intersects the THC within the omni-directional sensor radius, leading to a sensor cross-section defined by a compound boundary between a circular arc and a parabola.

Cutting plane positions leading to this case are shown in Figure 44. The associated cutting-plane cross-sections of the ATH coverage volumes in Figure 44 are shown in Figure 45.

First, the coordinates of the 'first point' on the THC, p_1, are determined by

$$x_{p_1} = \begin{cases} 0 & : 2\gamma = \frac{\pi}{2} \\ \frac{|h|}{\tan 2\gamma} & : 2\gamma \neq \frac{\pi}{2} \end{cases}, \tag{64}$$
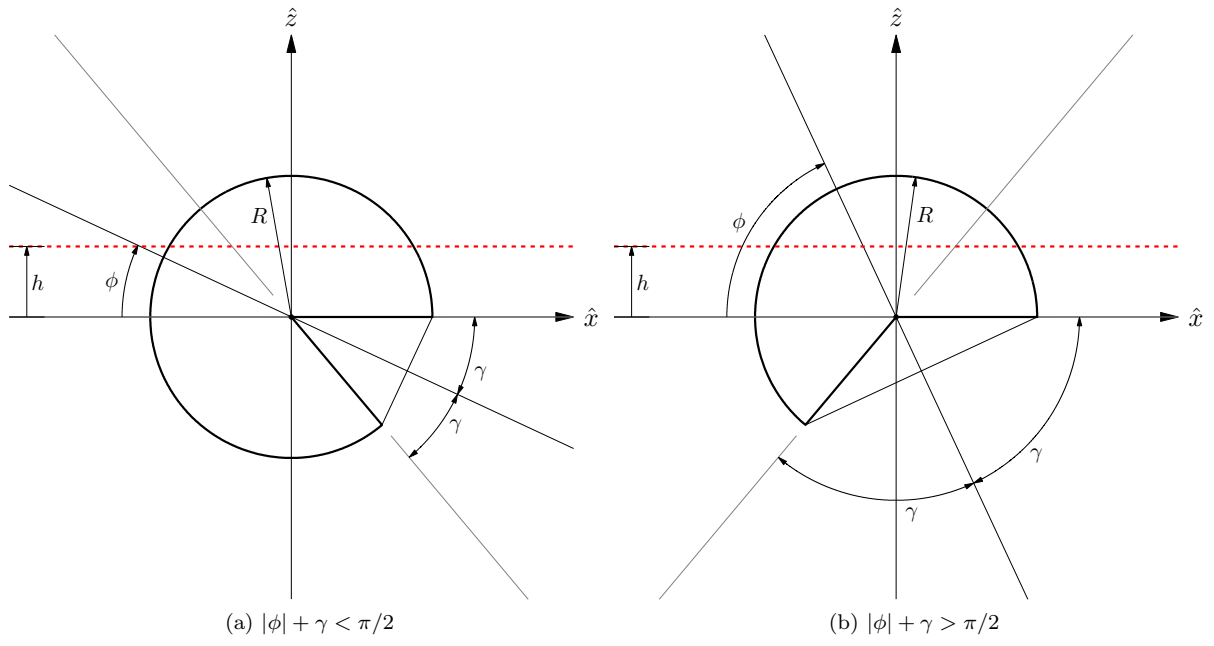
$$y_{p_1} = 0.$$

(a) $|\phi| + \gamma < \pi/2$ (b) $|\phi| + \gamma > \pi/2$

Figure 42: Case B1A

(a) $|\phi| + \gamma < \pi/2$ (b) $|\phi| + \gamma > \pi/2$
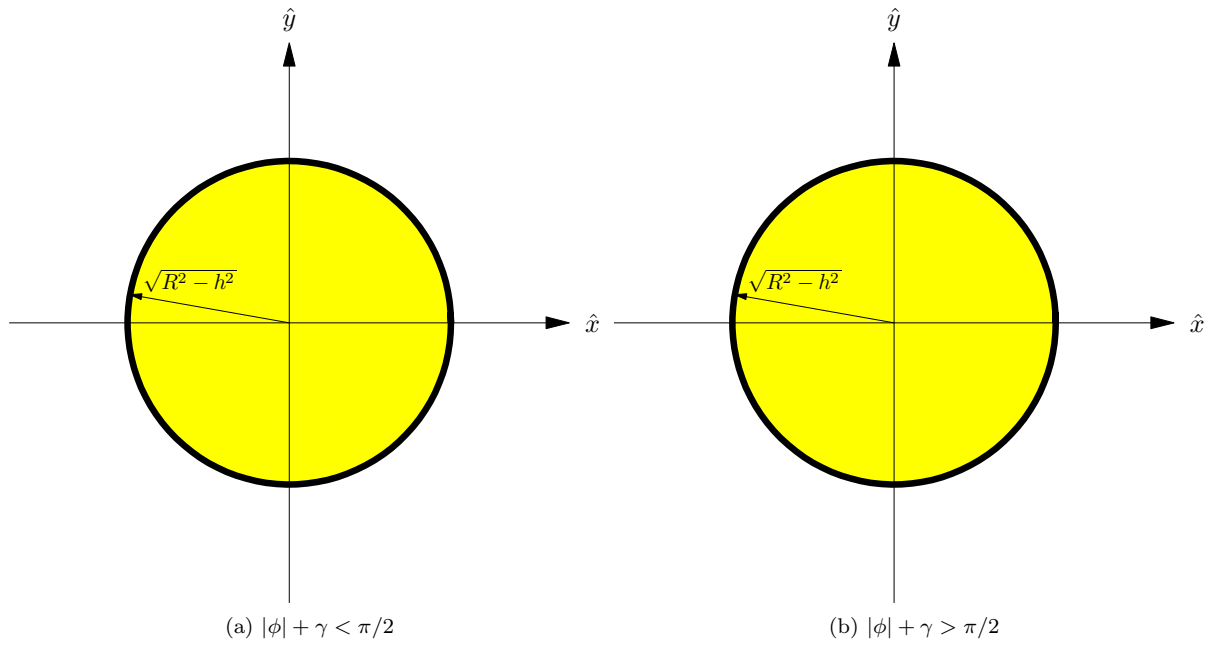
Figure 43: Case B1A

It can be shown by trigonometry that the coordinates of the 'second point,' p_{2+} can be determined by

$$x_{p_{2+}} = x_{p_1} + R - sqrth^2 + x_{p_1}^2$$

$$q = \left| m - \left(R - sqrth^2 + x_{p_1}^2 \right) \frac{\sin 2\gamma}{\cos \gamma} \right|,$$

(65)

$$y_{p_{2+}} = \sqrt{m^2 - q^2}.$$

It then follows that the parabolic parameter P may be determined by

$$P = \frac{y_{p_{2+}}^2}{4 \left(x_{p_{2+}} - x_{p_1} \right)}.$$

(66)

In the implementation, the parabolic span is split into two regions, such that the initial point of the outer polygon boundary is at the satellite location. This is done for convenience in the implementation of visualization functions. The upper half of the parabola is thus spanned by the angles

$$\psi_i = \pi,$$

$$\psi_f = \arctan \left(\frac{y_{p_{2+}}}{x_{p_{2+}} - (x_{p_1} + P)} \right),$$

(67)

relative to the focus, f. The radius relative to f is determined using Equation 62. The circular arc, relative to the origin is spanned by

$$\psi_i = \arctan \left(\frac{y_{p_{2+}}}{x_{p_{2+}}} \right),$$

$$\psi_f = 2\pi - \arctan \left(\frac{y_{p_{2+}}}{x_{p_{2+}}} \right).$$

(68)

with a radius given by Equation 63. Finally, the lower half of the parabola is spanned by

$$\psi_i = - \arctan \left(\frac{y_{p_{2+}}}{x_{p_{2+}} - (x_{p_1} + P)} \right),$$

$$\psi_f = -\pi.$$

(69)

Case B1C: $-R \sin 2\gamma \geq h$ **and** $h > -R$ The cutting plane lies below the lower intersection of the THC with the omni-directional sensor radius leading to either a disk-shaped sensor cross-section with radius $r_{\text{circular arc}}$, or no region at all if $|\phi| + \gamma > \pi/2$.

Cutting plane positions leading to this case are shown in Figure 46. The associated cutting-plane cross-sections of the ATH coverage volumes in Figure 46 are shown in Figure 47.

6.1.6   Case B2: $1 + n\varepsilon \geq e \geq 1 - n\varepsilon$ and $\phi < 0$

The THC cross-section is strictly parabolic, thus, sensor region cross-sections may be disks, non-existent, or defined by a compound boundary between a circular arc and a parabola. Excluding the cases where the cross-section is determined to be a disk, the problem is determining the parabolic parameter P in the canonical form of a parabola, and the 'first point,' p_1, of the THC conic section. 'First point' refers to the point on the parabola most negative in the $\hat{x}$ direction. By finding the location of a 'second point,' p_{2+}, where the conic section intersects the omni-directional sensor radius in the cutting plane, the appropriate angular intervals in ψ may be determined to define the hyperbolic and circular curves.

For the parabolic segments, the radius of the parabola with respect to the focus, f, located on the $\hat{x}$ axis at $x_{p_1} + P$, is given by

$$r_{\text{parabola}} = \frac{2P}{1 - \cos \psi}$$

(70)

The radius of the outer circular arc, bounding the omni-directional sensor radius in the ATH regions is given with respect to the origin by
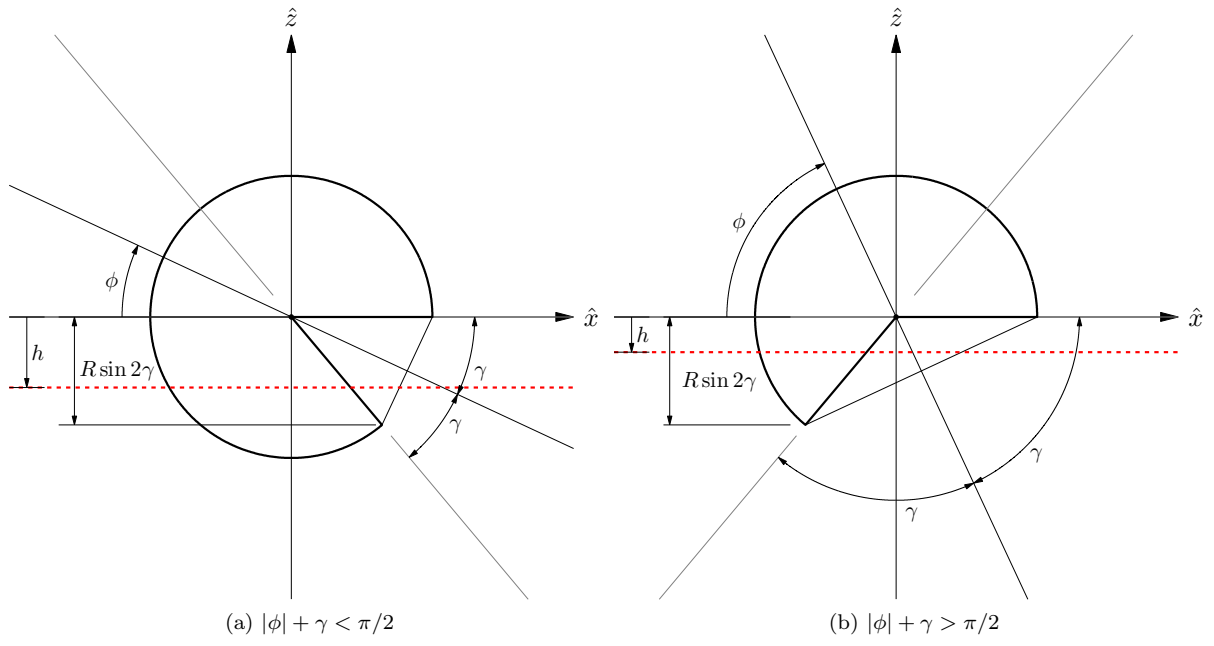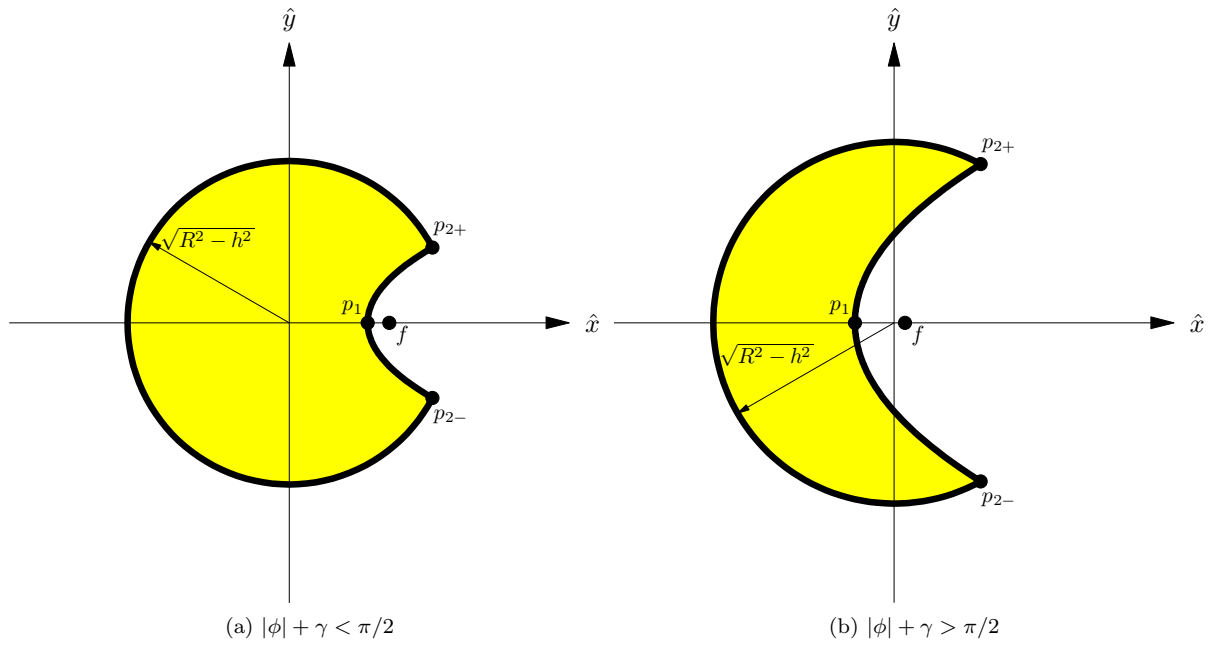
$$r_{\text{circular arc}} = \sqrt{R^2 - h^2}.$$

(71)

(a) $|\phi| + \gamma < \pi/2$

(b) $|\phi| + \gamma > \pi/2$

Figure 44: Case B1B

(a) $|\phi| + \gamma < \pi/2$

(b) $|\phi| + \gamma > \pi/2$

Figure 45: Case B1B

53

(a) $|\phi| + \gamma < \pi/2$ (b) $|\phi| + \gamma > \pi/2$

Figure 46: Case B1C
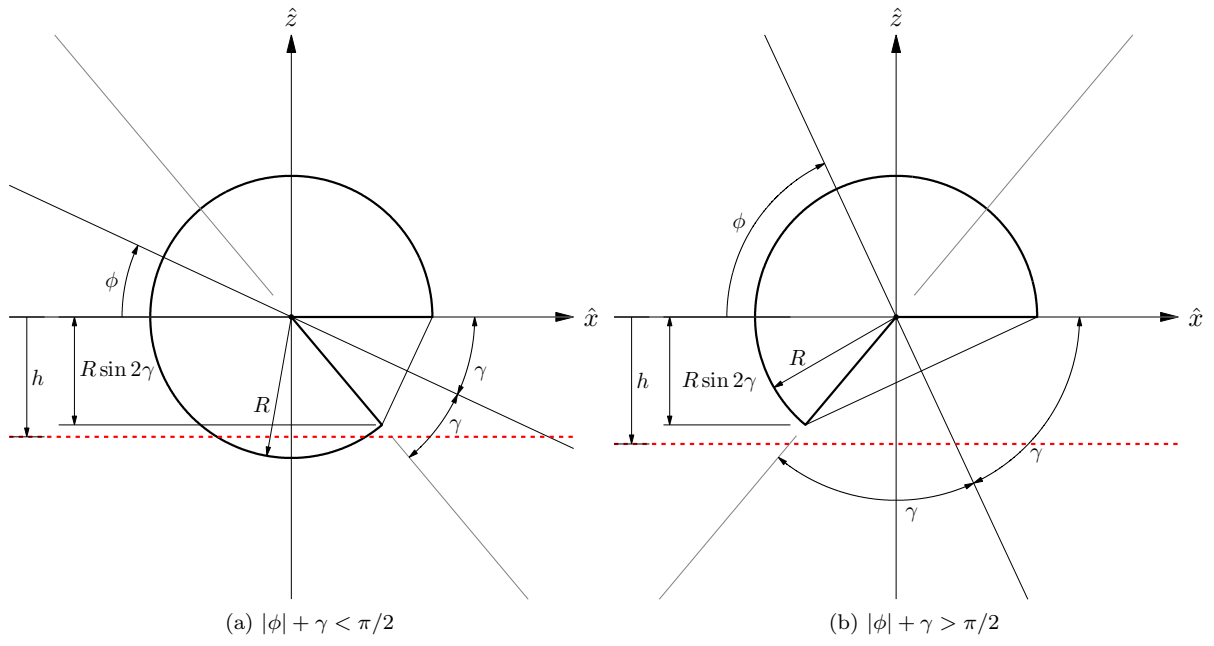

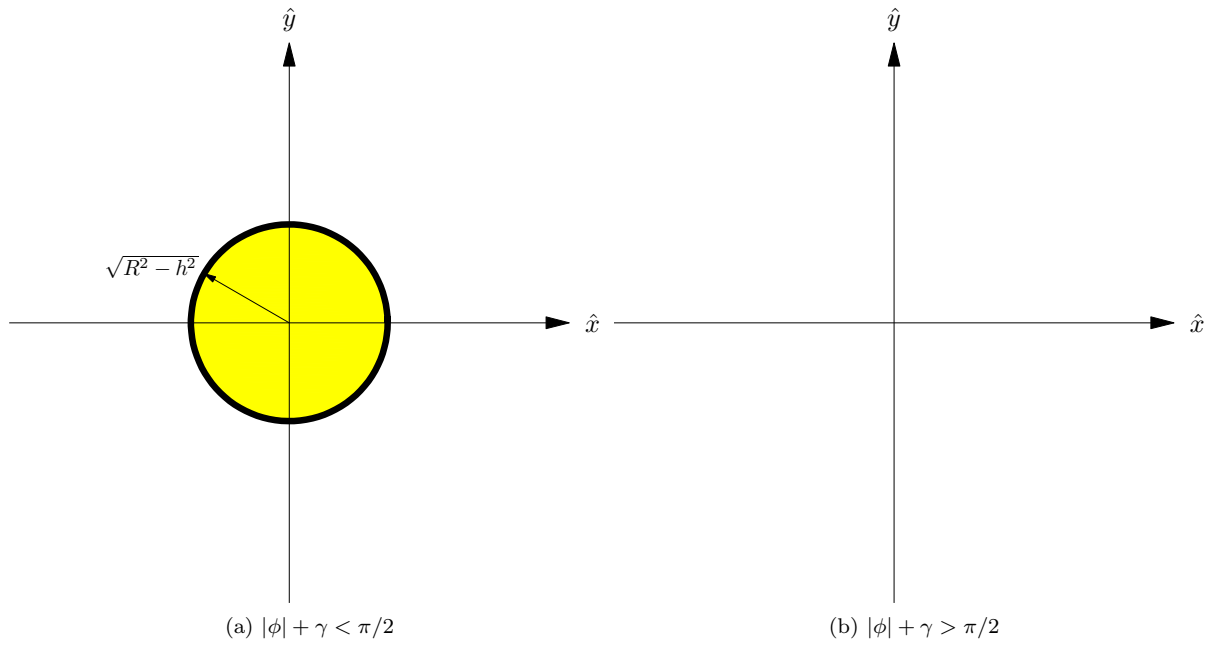(a) $|\phi| + \gamma < \pi/2$ (b) $|\phi| + \gamma > \pi/2$

Figure 47: Case B1C

Case B2A: $R > h$ **and** $h >= R\sin 2\gamma$ The cutting plane lies above the upper intersection of the THC with the omni-directional sensor radius leading to either a disk-shaped sensor cross-section with radius $r_{\text{circular arc}}$, or no region at all if $|\phi| + \gamma > \pi/2$.

Cutting plane positions leading to this case are shown in Figure 48. The associated cutting-plane cross-sections of the ATH coverage volumes in Figure 48 are shown in Figure 49.

(a) $|\phi| + \gamma < \pi/2$ (b) $|\phi| + \gamma > \pi/2$
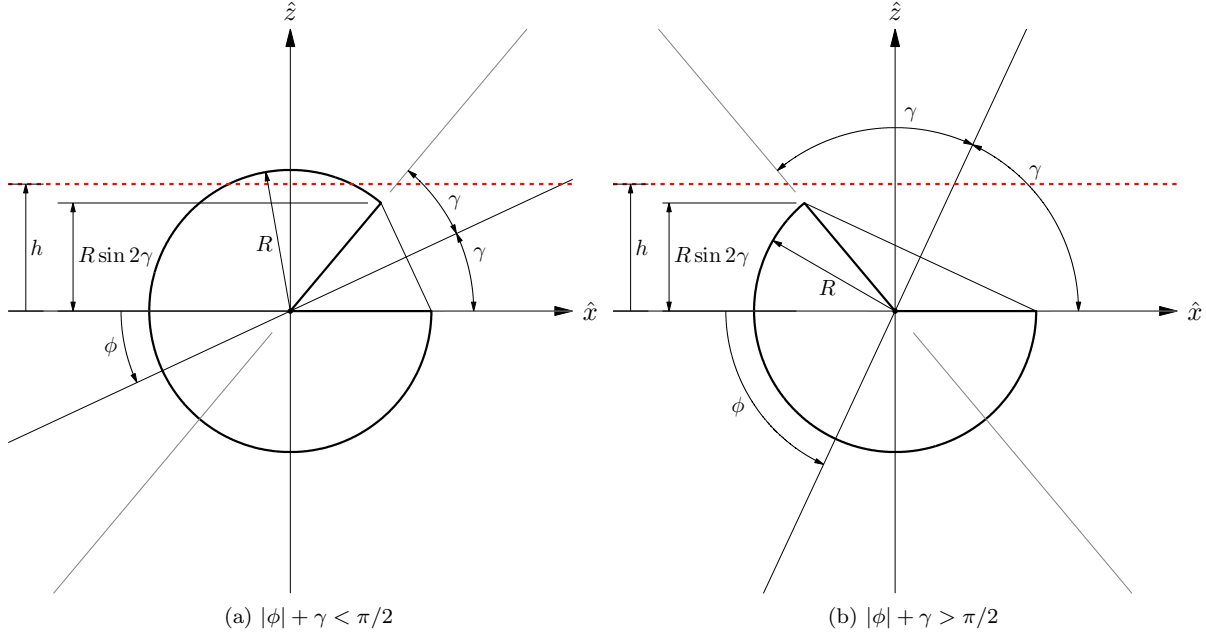
Figure 48: Case B2A

Case B2B: $R\sin 2\gamma > h$ **and** $h > 0$ The cutting plane intersects the THC within the omni-directional sensor radius, leading to a sensor cross-section defined by a compound boundary between a circular arc and a parabola.

Cutting plane positions leading to this case are shown in Figure 50. The associated cutting-plane cross-sections of the ATH coverage volumes in Figure 50 are shown in Figure 51.

First, the coordinates of the 'first point' on the THC, p_1, are determined by

$$x_{p_1} = \begin{cases} 0 & : 2\gamma = \frac{\pi}{2} \\ \frac{|h|}{\tan 2\gamma} & : 2\gamma \neq \frac{\pi}{2} \end{cases} \, , \tag{72}$$

$$y_{p_1} = 0.$$

It can be shown by trigonometry that the coordinates of the 'second point,' p_{2+} can be determined by

$$x_{p_{2+}} = x_{p_1} + R - sqrth^2 + x_{p_1}^2,$$

$$q = \left| m - \left(R - sqrth^2 + x_{p_1}^2 \right) \frac{\sin 2\gamma}{\cos \gamma} \right|, \tag{73}$$

$$y_{p_{2+}} = \sqrt{m^2 - q^2}.$$

It then follows that the parabolic parameter P may be determined by

$$P = \frac{y_{p_{2+}}^2}{4\left(x_{p_{2+}} - x_{p_1}\right)}. \tag{74}$$

55

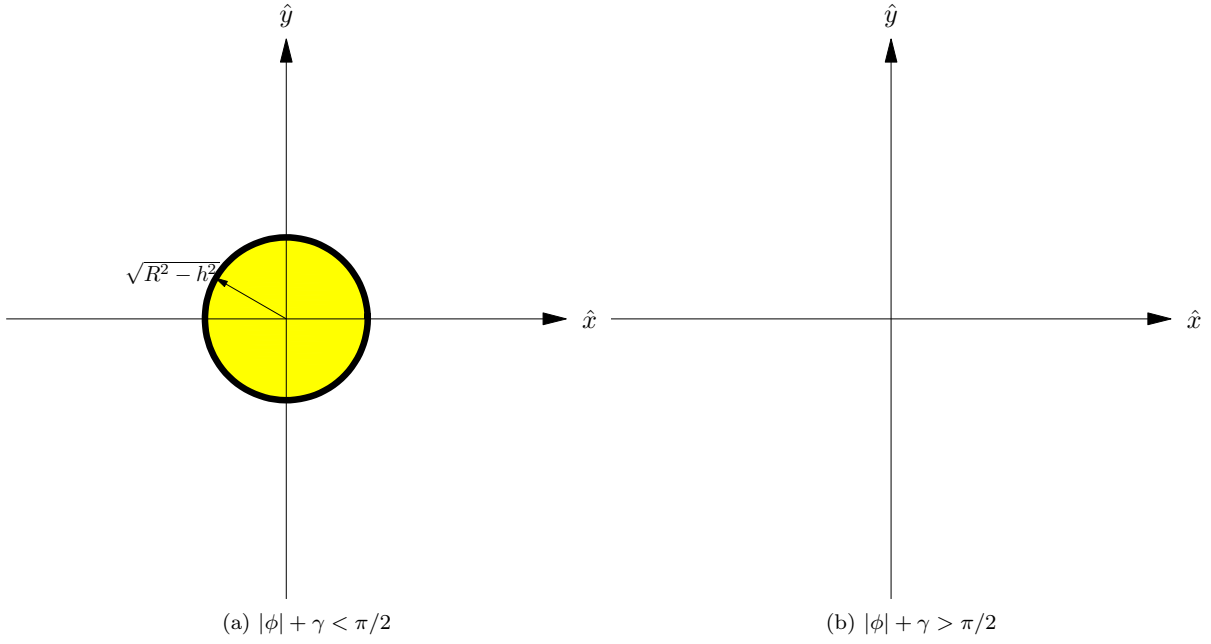(a) $|\phi| + \gamma < \pi/2$ (b) $|\phi| + \gamma > \pi/2$

Figure 49: Case B2A

In the implementation, the parabolic span is split into two regions, such that the initial point of the outer polygon boundary is at the satellite location. This is done for convenience in the implementation of visualization functions. The upper half of the parabola is thus spanned by the angles

$$
\begin{aligned}
\psi_i &= \pi, \\
\psi_f &= \arctan\left(\frac{y_{p_{2+}}}{x_{p_{2+}} - (x_{p_1} + P)}\right),
\end{aligned}
\tag{75}
$$

relative to the focus, f. The radius relative to f is determined using Equation 70. The circular arc, relative to the origin is spanned by

$$
\begin{aligned}
\psi_i &= \arctan\left(\frac{y_{p_{2+}}}{x_{p_{2+}}}\right) \\
\psi_f &= 2\pi - \arctan\left(\frac{y_{p_{2+}}}{x_{p_{2+}}}\right)
\end{aligned}
\tag{76}
$$

with a radius given by Equation 71. Finally, the lower half of the parabola is spanned by

$$
\begin{aligned}
\psi_i &= -\arctan\left(\frac{y_{p_{2+}}}{x_{p_{2+}} - (x_{p_1} + P)}\right) \\
\psi_f &= -\pi
\end{aligned}
\tag{77}
$$

Case B2C: $0 \geq h$ **and** $h > -R$ The cutting plane lies below the lower intersection of the THC with the omni-directional sensor radius, leading to a disk-shaped sensor cross-section with radius $r_{\text{circular arc}}$.

Cutting plane positions leading to this case are shown in Figure 52. The associated cutting-plane cross-sections of the ATH coverage volumes in Figure 52 are shown in Figure 53.
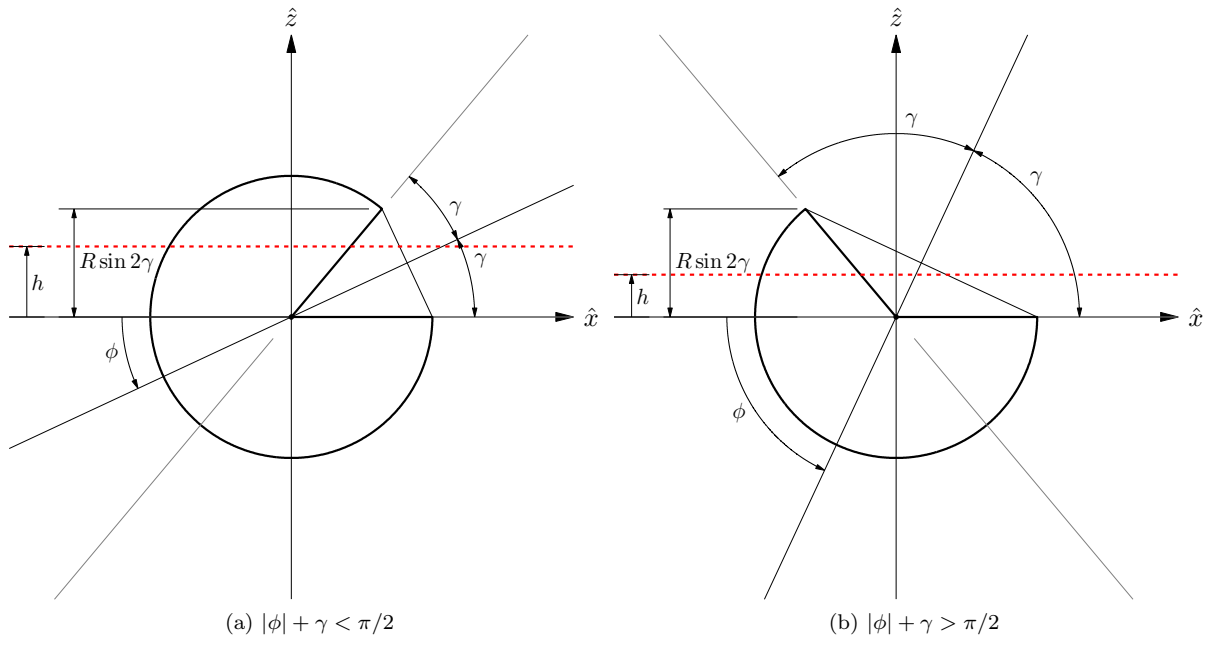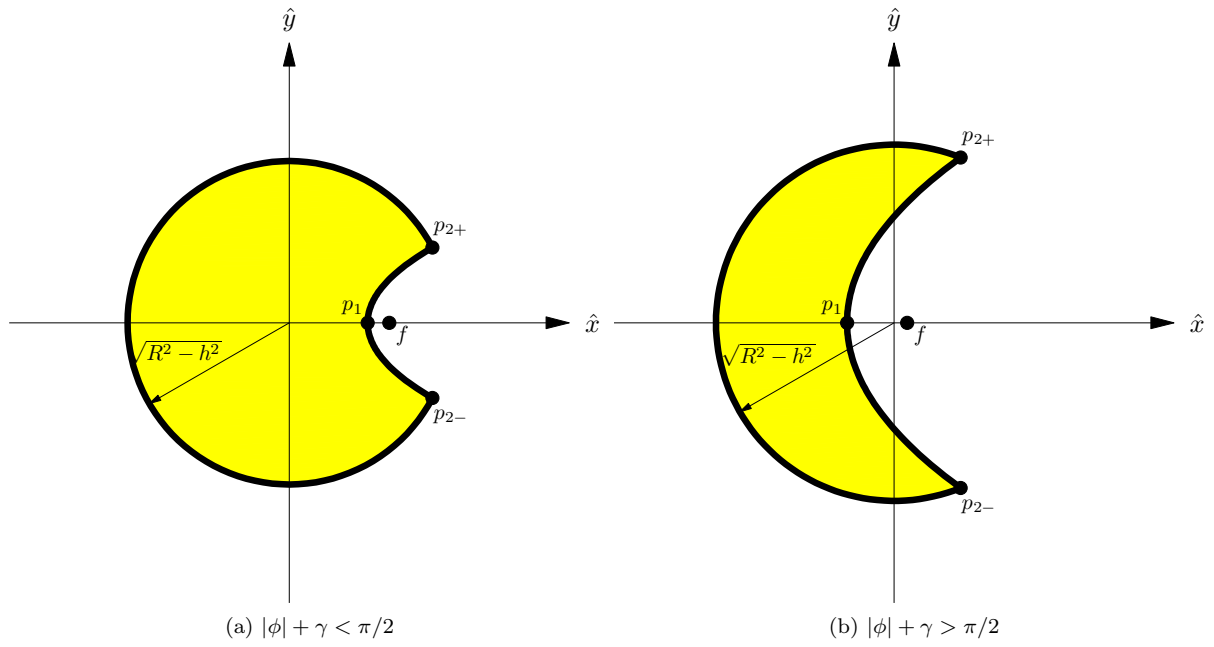
56

(a) $|\phi| + \gamma < \pi/2$ (b) $|\phi| + \gamma > \pi/2$

Figure 50: Case B2B

(a) $|\phi| + \gamma < \pi/2$ (b) $|\phi| + \gamma > \pi/2$

Figure 51: Case B2B

(a) $|\phi| + \gamma < \pi/2$

(b) $|\phi| + \gamma > \pi/2$

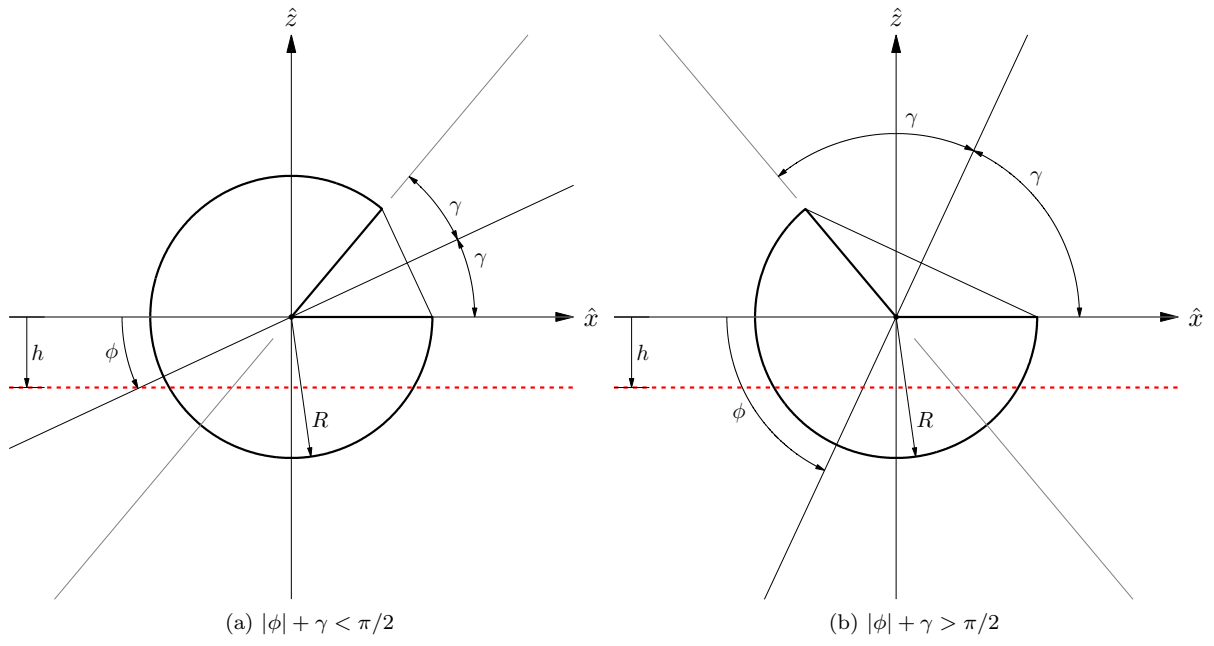Figure 52: Case B2C

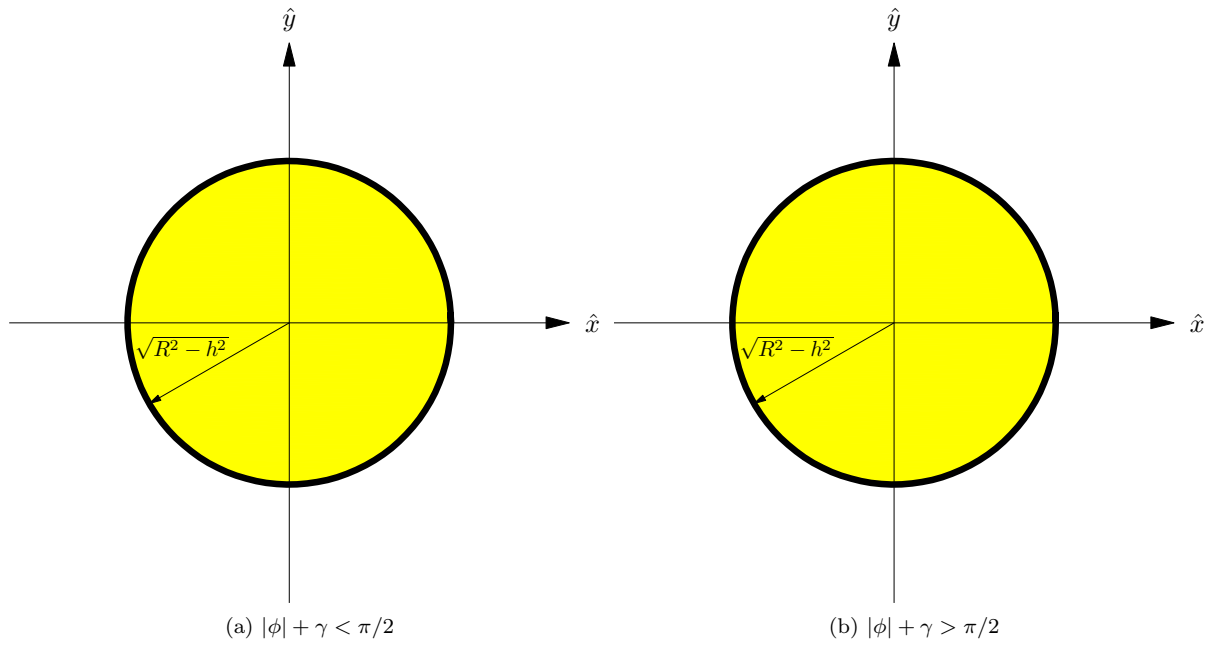(a) $|\phi| + \gamma < \pi/2$

(b) $|\phi| + \gamma > \pi/2$

Figure 53: Case B2C

6.1.7 Case C1: $1 - n\varepsilon > e$ and $\phi > 0$

The THC cross-section is strictly elliptical, thus, sensor region cross-sections may be disks, non-existent, or defined by a compound boundary between a circular arc and an ellipse or elliptical arc. Excluding the cases where the cross-section is determined to be a disk, the problem is determining the elliptical parameters a and b in the canonical form of an ellipse, and determining the center-point of the conic-section, s'. s' is centered between the 'first point,' p_1, of the THC conic section, and the 'third point,' p_3, at the opposite end of the ellipse major axis from p_1. When it exists, by finding the location of a 'second point,' p_{2+}, where the conic section intersects the omni-directional sensor radius in the cutting plane, the appropriate angular intervals in ψ may be determined to define the hyperbolic and circular curves. When p_{2+} does not exist, the ellipse forms a hole in a disk shaped region.

For the elliptical segments, the radius of the ellipse with respect to the center-point s', is given by

$$r_{\text{ellipse}} = \frac{ab}{\sqrt{(b\cos\psi)^2 + (a\sin\psi)^2}} \tag{78}$$

The radius of the outer circular arc, bounding the omni-directional sensor radius in the ATH regions is given with respect to the origin by

$$r_{\text{circular arc}} = \sqrt{R^2 - h^2}. \tag{79}$$

Case C1A: $R > h$ and $h \geq 0$ The cutting plane lies above the upper intersection of the THC with the omni-directional sensor radius, leading to a disk-shaped sensor cross-section with radius $r_{\text{circular arc}}$.

Cutting plane positions leading to this case are shown in Figure 54. The associated cutting-plane cross-sections of the ATH coverage volumes in Figure 54 are shown in Figure 55.
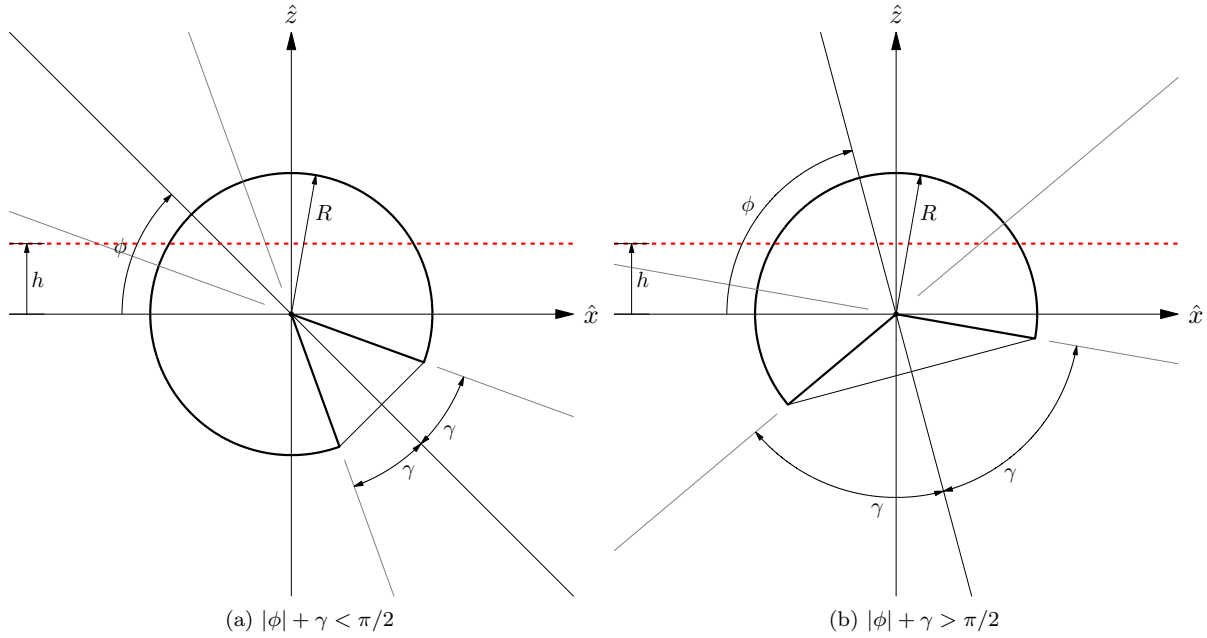

(a) $|\phi| + \gamma < \pi/2$ (b) $|\phi| + \gamma > \pi/2$

Figure 54: Case C1A

Case C1B: $0 > h$ and $h \geq -R\sin(|\phi| - \gamma)$ The cutting plane intersects the THC within the omni-directional sensor radius, leading to a sensor cross-section defined by a circular outer boundary with an elliptical interior hole.

(a) $|\phi| + \gamma < \pi/2$ (b) $|\phi| + \gamma > \pi/2$
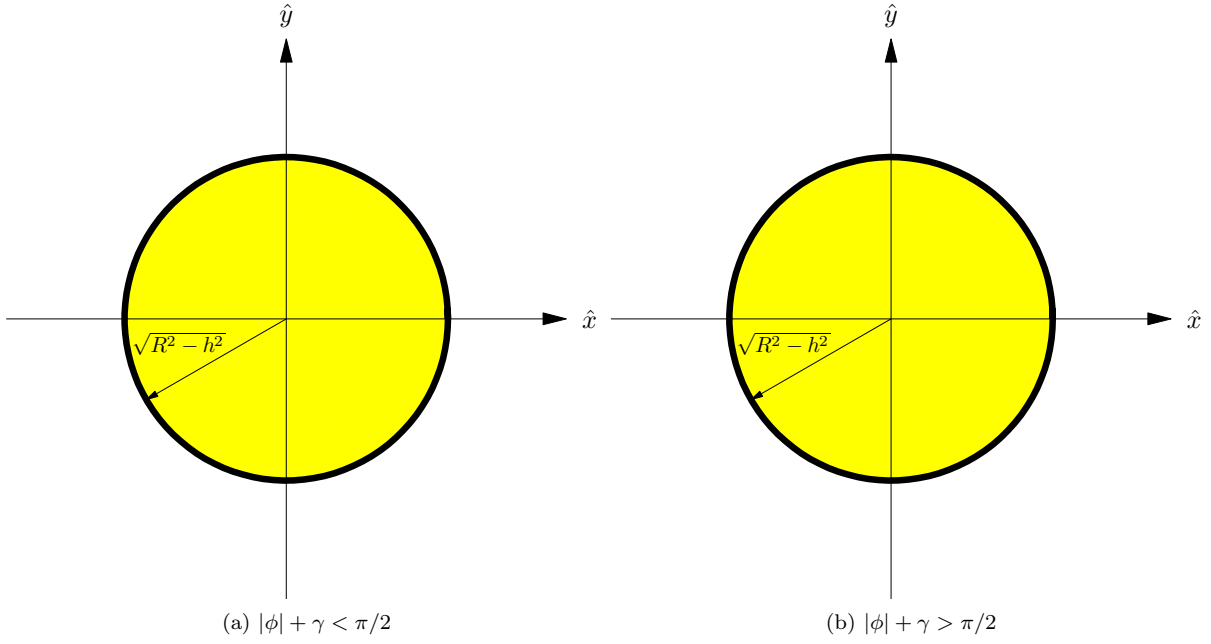
Figure 55: Case C1A

Cutting plane positions leading to this case are shown in Figure 56. The associated cutting-plane cross-sections of the ATH coverage volumes in Figure 56 are shown in Figure 57.

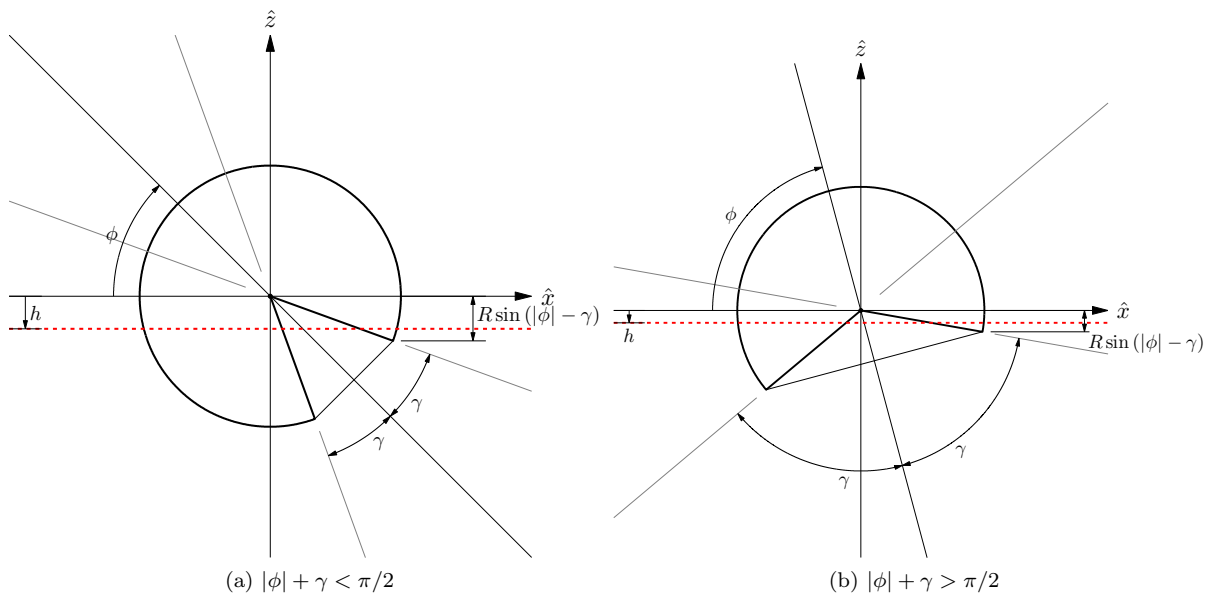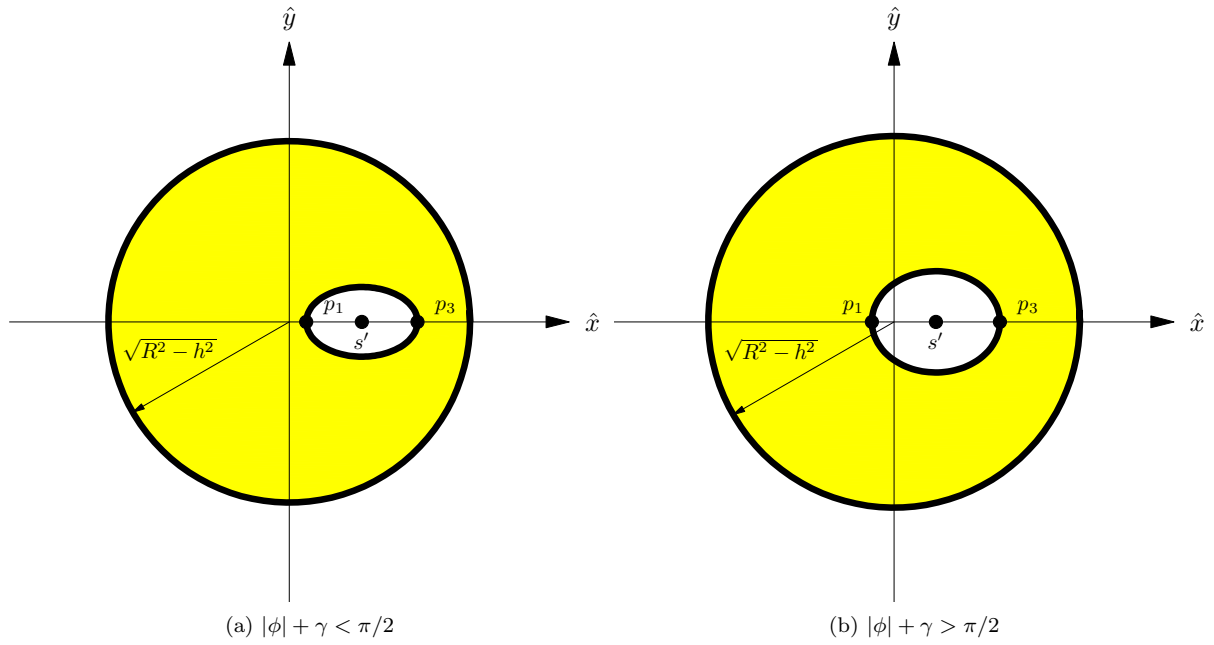First, the coordinates of the 'first' and 'third' points, p_1 and p_3, which are on either end of the major axis of the elliptical THC conic section, are determined by

$$
\begin{aligned}
x_{p_1} &= \frac{|h|}{\tan\left(|\phi| + \gamma\right)}, \\
x_{p_3} &= \frac{|h|}{\tan\left(|\phi| + \gamma\right)}.
\end{aligned}
\tag{80}
$$

It then follows that the elliptical parameters a, b, and x'_s may be determined by

$$
\begin{aligned}
a &= \frac{x_{p_3} - x_{p_1}}{2}, \\
b &= a\sqrt{1 - e^2},
\end{aligned}
\tag{81}
$$

$$
x'_s = \frac{x_{p_1} + x_{p_3}}{2}.
\tag{82}
$$

For a radius given by equation 79, an outer circle spans $0 \le \psi \le 2\pi$, while an internal elliptical hole region is defined by 78 over $0 \le \psi \le 2\pi$ centered on s'.

Case C1C: $-R\sin\left(|\phi| - \gamma\right) > h$ **and** $h > -R\sin\left(|\phi| + \gamma\right)$ The cutting plane intersects the THC within the omni-directional sensor radius, leading to a sensor cross-section defined by a compound boundary between a circular arc and an elliptical arc.

Cutting plane positions leading to this case are shown in Figure 58. The associated cutting-plane cross-sections of the ATH coverage volumes in Figure 58 are shown in Figure 59.

First, the coordinates of the 'first' and 'third' points, p_1 and p_3, which are on either end of the major

(a) $|\phi| + \gamma < \pi/2$

(b) $|\phi| + \gamma > \pi/2$

Figure 56: Case C1B

(a) $|\phi| + \gamma < \pi/2$

(b) $|\phi| + \gamma > \pi/2$

Figure 57: Case C1B

axis of the elliptical THC conic section, are determined by

$$x_{p_1} = \frac{|h|}{\tan\left(|\phi| + \gamma\right)},$$
$$x_{p_3} = \frac{|h|}{\tan\left(|\phi| + \gamma\right)}.$$

(83)

It can be shown by trigonometry then that using the intermediate values q and g, found by the relations

$$g = \left(R - \sqrt{h^2 + x_{p_1}^2}\right)\frac{\cos\gamma}{\cos|\phi|},$$
$$q = m - g\frac{\sin\left(\gamma + |\phi|\right)}{\cos\gamma},$$

(84)

the coordinates of the 'second point,' p_{2+}, can be determined by

$$x_{p_{2+}} = x_{p_1} + g$$
$$y_{p_{2+}} = \sqrt{m^2 - q^2}$$

(85)

It then follows that the elliptical parameters a, b, and $x_{s'}$ may be determined by

$$a = \frac{x_{p_3} - x_{p_1}}{2},$$
$$b = a\sqrt{1 - e^2},$$

(86)

$$x'_s = \frac{x_{p_1} + x_{p_3}}{2}.$$

(87)

In the implementation, the elliptical arc span is split into two regions, such that the initial point of the outer polygon boundary is at the satellite location. This is done for convenience in the implementation of visualization functions. The upper half of the elliptical arc is thus spanned by the angles

$$\psi_i = \pi,$$
$$\psi_f = \arctan\left(\frac{y_{p_{2+}}}{x_{p_{2+}} - x'_s}\right),$$

(88)

relative to s'. The radius relative to s' is determined using Equation 78. The circular arc, relative to the origin is spanned by

$$\psi_i = \arctan\left(\frac{y_{p_{2+}}}{x_{p_{2+}}}\right)$$
$$\psi_f = 2\pi - \arctan\left(\frac{y_{p_{2+}}}{x_{p_{2+}}}\right)$$

(89)

with a radius given by Equation 79. Finally, the lower half of the hyperbola is spanned by

$$\psi_i = -\arctan\left(\frac{y_{p_{2+}}}{x_{p_{2+}} - x'_s}\right)$$
$$\psi_f = -\pi$$

(90)

Case C1D: $-R\sin\left(|\phi| + \gamma\right) \geq h$ **and** $h > -R$ The cutting plane lies below the lower intersection of the THC with the omni-directional sensor radius leading to either a disk-shaped sensor cross-section with radius $r_{\text{circular arc}}$, or no region at all if $|\phi| + \gamma > \pi/2$.

Cutting plane positions leading to this case are shown in Figure 60. The associated cutting-plane cross-sections of the ATH coverage volumes in Figure 60 are shown in Figure 61.
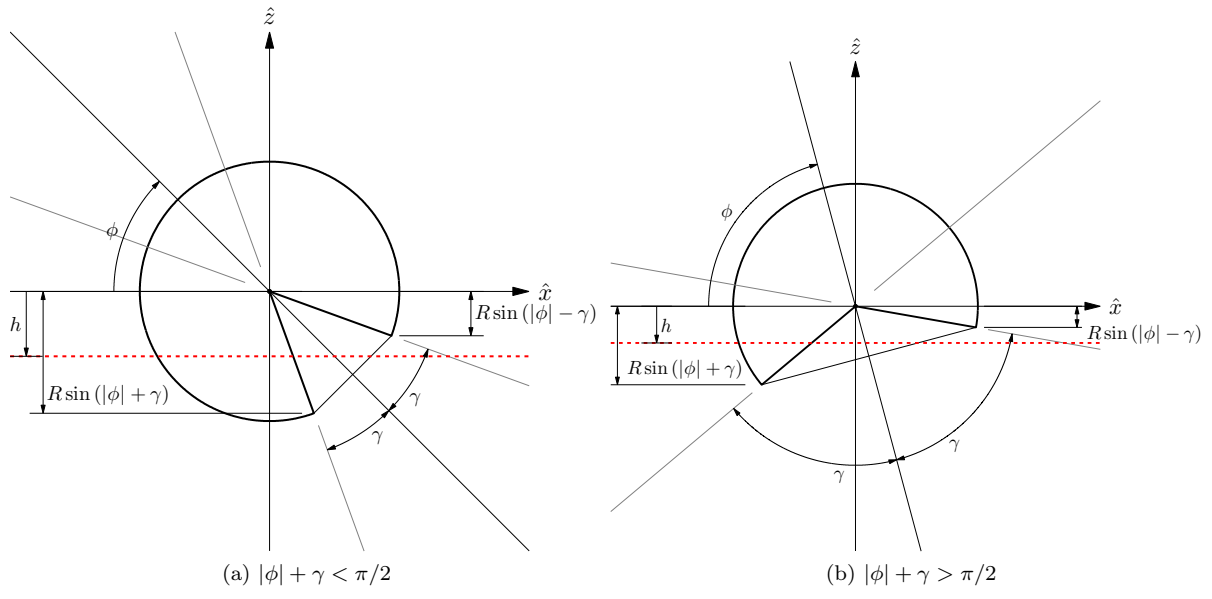
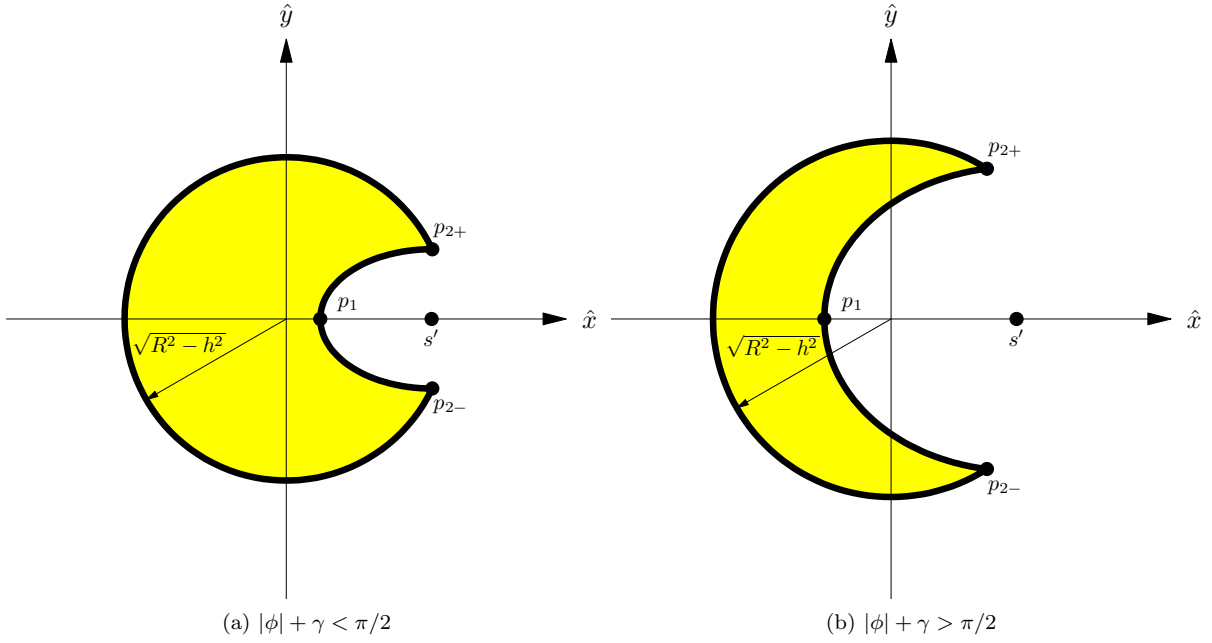(a) $|\phi| + \gamma < \pi/2$ (b) $|\phi| + \gamma > \pi/2$
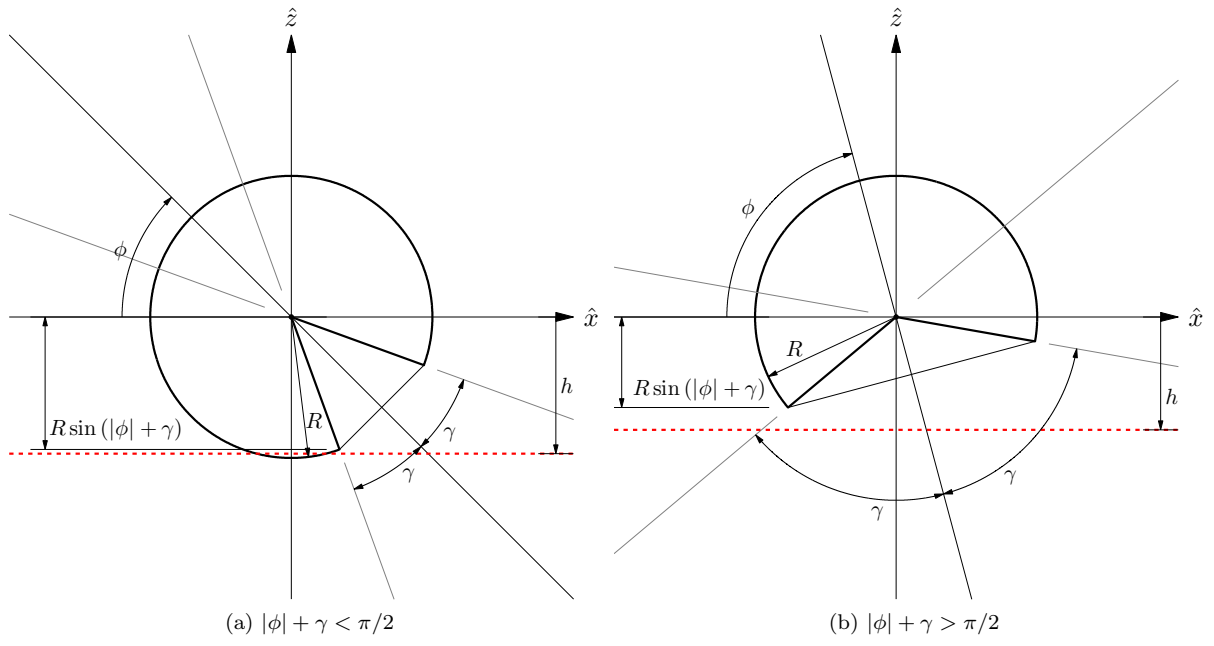
Figure 58: Case C1C

(a) $|\phi| + \gamma < \pi/2$ (b) $|\phi| + \gamma > \pi/2$

Figure 59: Case C1C

(a) $|\phi| + \gamma < \pi/2$

(b) $|\phi| + \gamma > \pi/2$

Figure 60: Case C1D
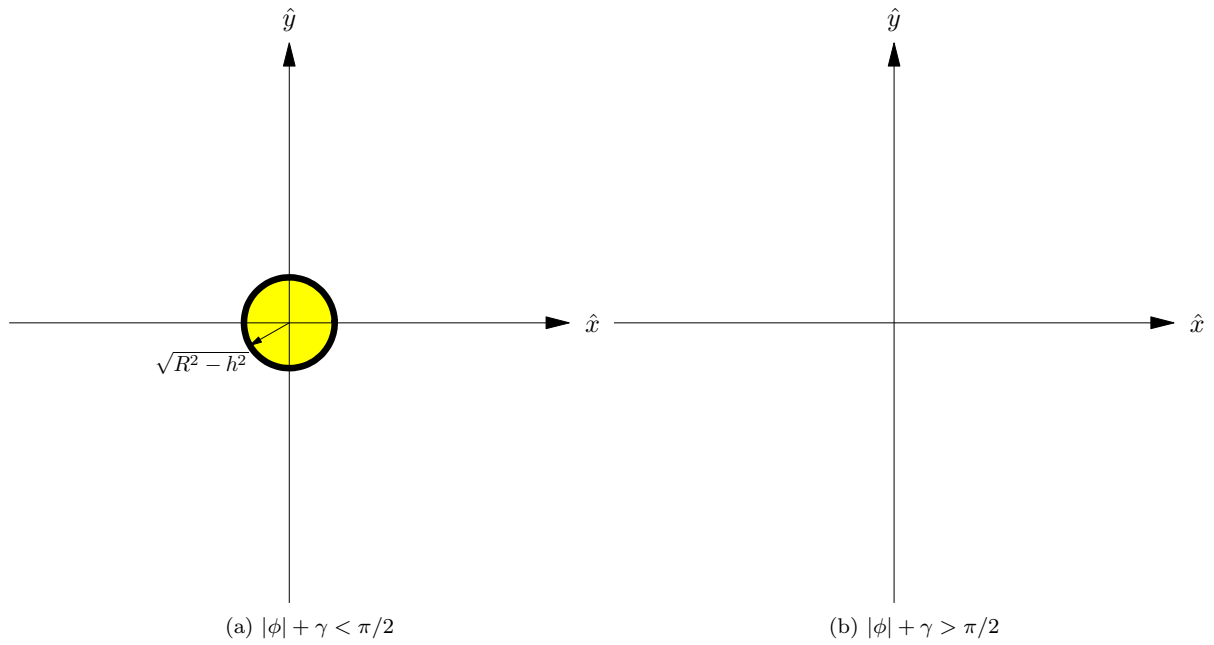

(a) $|\phi| + \gamma < \pi/2$

(b) $|\phi| + \gamma > \pi/2$

Figure 61: Case C1D

6.1.8   Case C2: $1 - n\varepsilon > e$ and $\phi < 0$

The THC cross-section is strictly elliptical, thus, sensor region cross-sections may be disks, non-existent, or defined by a compound boundary between a circular arc and an ellipse or elliptical arc. Excluding the cases where the cross-section is determined to be a disk, the problem is determining the elliptical parameters a and b in the canonical form of an ellipse, and determining the center-point of the conic-section, s'. s' is centered between the 'first point,' p_1, of the THC conic section, and the 'third point,' p_3, at the opposite end of the ellipse major axis from p_1. When it exists, by finding the location of a 'second point,' p_{2+}, where the conic section intersects the omni-directional sensor radius in the cutting plane, the appropriate angular intervals in ψ may be determined to define the hyperbolic and circular curves. When p_{2+} does not exist, the ellipse forms a hole in a disk shaped region.

For the elliptical segments, the radius of the ellipse with respect to the center-point s', is given by

$$r_{\text{ellipse}} = \frac{ab}{\sqrt{(b \cos \psi)^2 + (a \sin \psi)^2}} \tag{91}$$

The radius of the outer circular arc, bounding the omni-directional sensor radius in the ATH regions is given with respect to the origin by

$$r_{\text{circular arc}} = \sqrt{R^2 - h^2}. \tag{92}$$

Case C2A: $R > h$ **and** $h \geq R \sin(|\phi| + \gamma)$ The cutting plane lies above the upper intersection of the THC with the omni-directional sensor radius leading to either a disk-shaped sensor cross-section with radius $r_{\text{circular arc}}$, or no region at all if $|\phi| + \gamma > \pi/2$.

Cutting plane positions leading to this case are shown in Figure 62. The associated cutting-plane cross-sections of the ATH coverage volumes in Figure 62 are shown in Figure 63.
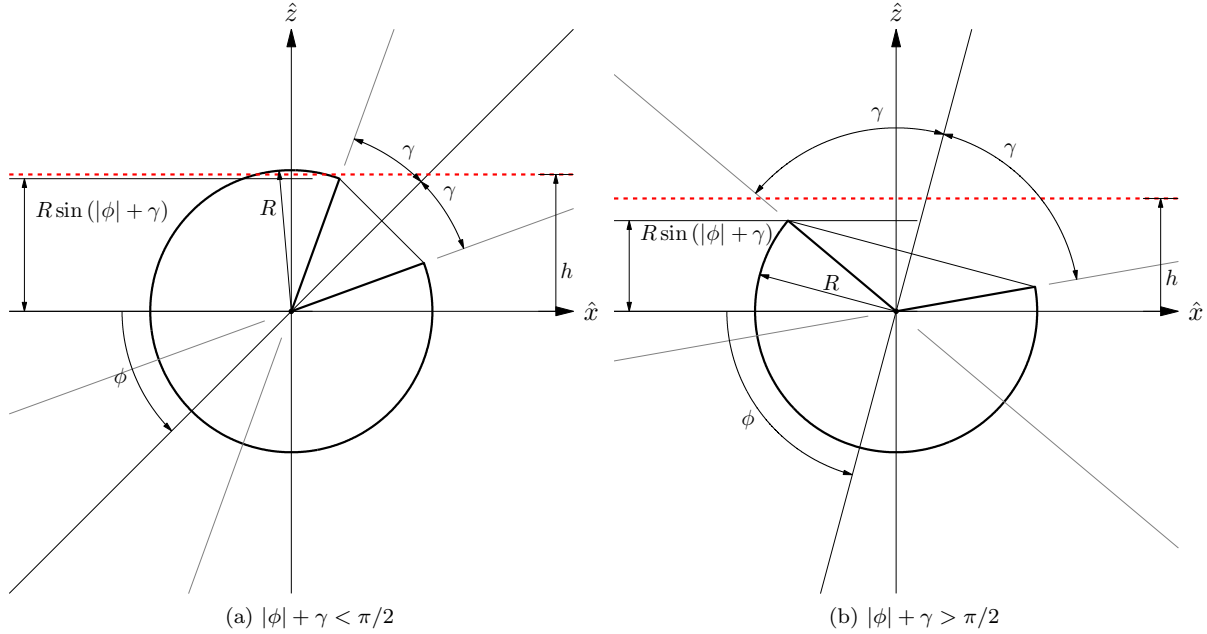

(a) $|\phi| + \gamma < \pi/2$ (b) $|\phi| + \gamma > \pi/2$

Figure 62: Case C2A

Case C2B: $R \sin(|\phi| + \gamma) > h$ **and** $h > R \sin(|\phi| - \gamma)$ The cutting plane intersects the THC within the omni-directional sensor radius, leading to a sensor cross-section defined by a compound boundary between a circular arc and an elliptical arc.

(a) $|\phi| + \gamma < \pi/2$ (b) $|\phi| + \gamma > \pi/2$
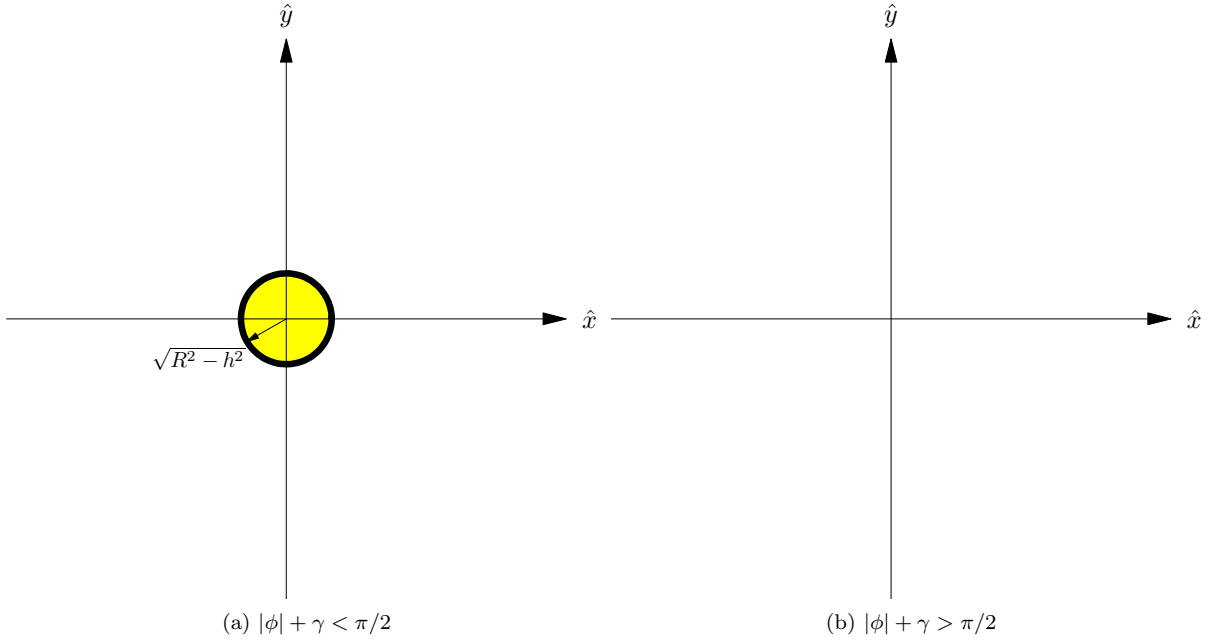
Figure 63: Case C2A

Cutting plane positions leading to this case are shown in Figure 64. The associated cutting-plane cross-sections of the ATH coverage volumes in Figure 64 are shown in Figure 65.

First, the coordinates of the 'first' and 'third' points, p_1 and p_3, which are on either end of the major axis of the elliptical THC conic section, are determined by

$$
\begin{aligned}
x_{p_1} &= \frac{|h|}{\tan\left(|\phi| + \gamma\right)}, \\
x_{p_3} &= \frac{|h|}{\tan\left(|\phi| + \gamma\right)}.
\end{aligned}
\tag{93}
$$

It can be shown by trigonometry then that using the intermediate values q and g, found by the relations

$$
\begin{aligned}
g &= \left(R - \sqrt{h^2 + x_{p_1}^2} \right) \frac{\cos \gamma}{\cos |\phi|}, \\
q &= m - g \frac{\sin\left(\gamma + |\phi|\right)}{\cos \gamma},
\end{aligned}
\tag{94}
$$

the coordinates of the 'second point,' p_{2+}, can be determined by

$$
\begin{aligned}
x_{p_{2+}} &= x_{p_1} + g. \\
y_{p_{2+}} &= \sqrt{m^2 - q^2}.
\end{aligned}
\tag{95}
$$

It then follows that the elliptical parameters a, b, and $x_{s'}$ may be determined by

$$
\begin{aligned}
a &= \frac{x_{p_3} - x_{p_1}}{2}, \\
b &= a\sqrt{1 - e^2},
\end{aligned}
\tag{96}
$$

$$
x_s' = \frac{x_{p_1} + x_{p_3}}{2}.
\tag{97}
$$

66

In the implementation, the elliptical arc span is split into two regions, such that the initial point of the outer polygon boundary is at the satellite location. This is done for convenience in the implementation of visualization functions. The upper half of the elliptical arc is thus spanned by the angles

$$\psi_i = \pi,$$
$$\psi_f = \arctan\left(\frac{y_{p2+}}{x_{p2+} - x'_s}\right),$$

(98)

relative to s'. The radius relative to s' is determined using Equation 78. The circular arc, relative to the origin is spanned by

$$\psi_i = \arctan\left(\frac{y_{p2+}}{x_{p2+}}\right),$$
$$\psi_f = 2\pi - \arctan\left(\frac{y_{p2+}}{x_{p2+}}\right),$$

(99)

with a radius given by Equation 79. Finally, the lower half of the hyperbola is spanned by

$$\psi_i = -\arctan\left(\frac{y_{p2+}}{x_{p2+} - x'_s}\right),$$
$$\psi_f = -\pi.$$

(100)

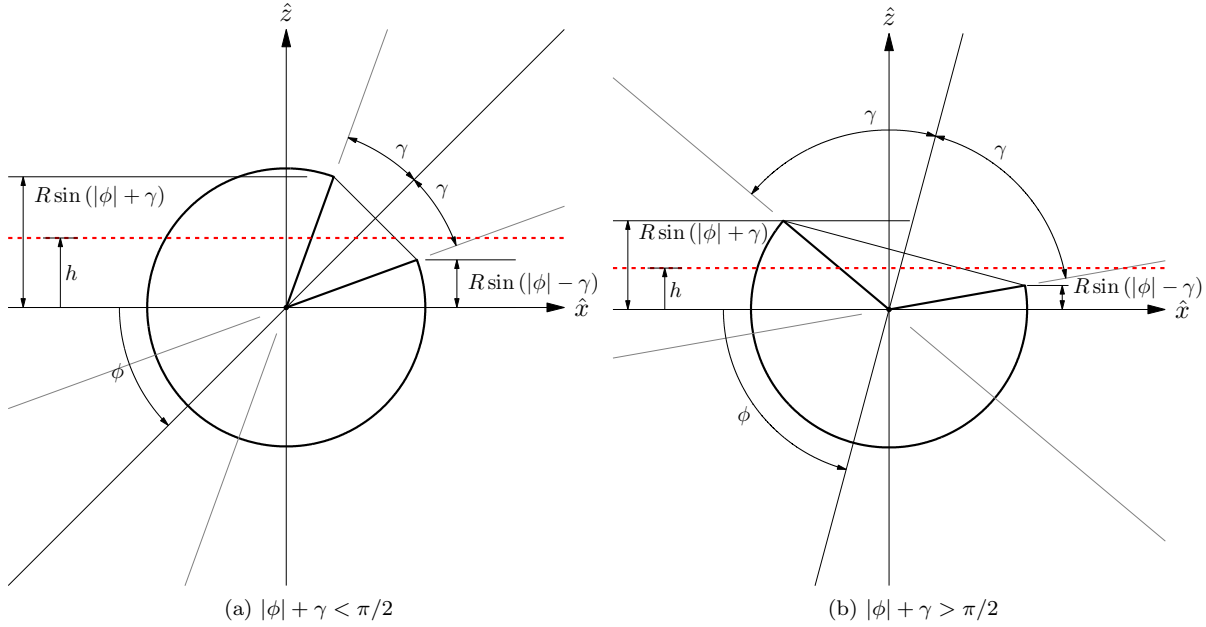(a) $|\phi| + \gamma < \pi/2$ (b) $|\phi| + \gamma > \pi/2$

Figure 64: Case C2B

Case C2C: $R\sin\left(|\phi| - \gamma\right) \geq h$ **and** $h > 0$ The cutting plane intersects the THC within the omni-directional sensor radius, leading to a sensor cross-section defined by a circular outer boundary with an elliptical interior hole.

Cutting plane positions leading to this case are shown in Figure 66. The associated cutting-plane cross-sections of the ATH coverage volumes in Figure 66 are shown in Figure 67.
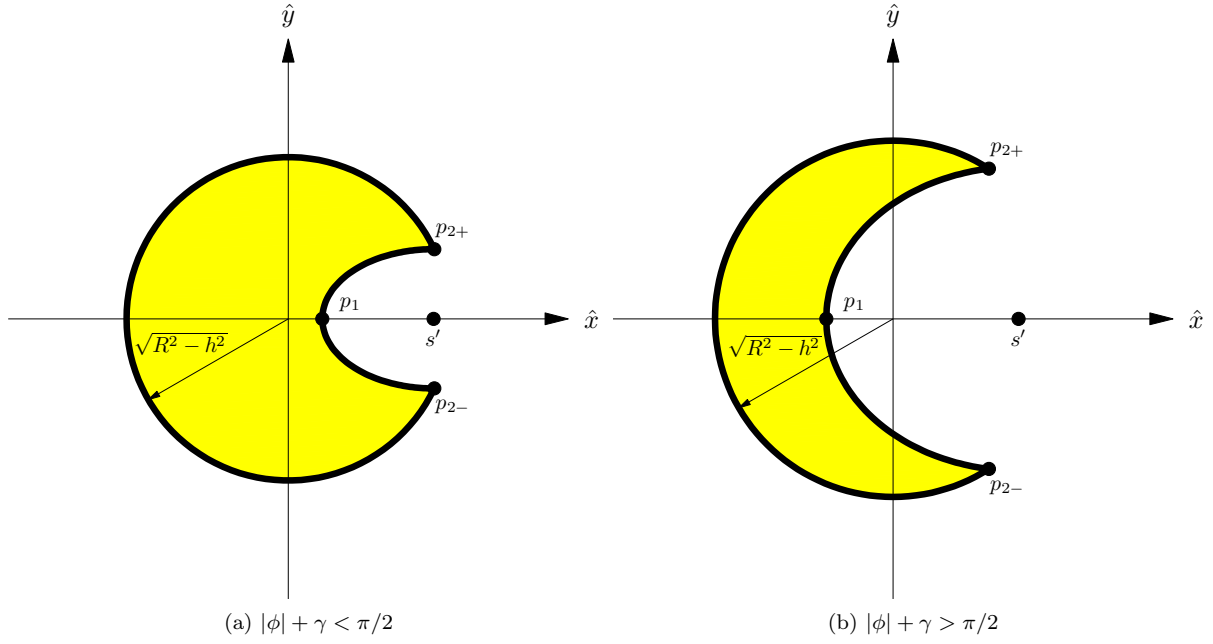
67

(a) $|\phi| + \gamma < \pi/2$

(b) $|\phi| + \gamma > \pi/2$

Figure 65: Case C2B

First, the coordinates of the 'first' and 'third' points, p_1 and p_3, which are on either end of the major axis of the elliptical THC conic section, are determined by

$$
\begin{aligned}
x_{p_1} &= \frac{|h|}{\tan\left(|\phi| + \gamma\right)}, \\
x_{p_3} &= \frac{|h|}{\tan\left(|\phi| + \gamma\right)}.
\end{aligned}
\tag{101}
$$

It then follows that the elliptical parameters a, b, and x'_s may be determined by

$$
\begin{aligned}
a &= \frac{x_{p_3} - x_{p_1}}{2}, \\
b &= a\sqrt{1 - e^2},
\end{aligned}
\tag{102}
$$

$$
x'_s = \frac{x_{p_1} + x_{p_3}}{2}.
\tag{103}
$$

For a radius given by equation 92, an outer circle spans $0 \leq \psi \leq 2\pi$, while an internal elliptical hole region is defined by 91 over $0 \leq \psi \leq 2\pi$ centered on s'.

Case C2D: $0 \geq h$ **and** $h > -R$ The cutting plane lies below the lower intersection of the THC with the omni-directional sensor radius, leading to a disk-shaped sensor cross-section with radius $r_{\text{circular arc}}$.

Cutting plane positions leading to this case are shown in Figure 68. The associated cutting-plane cross-sections of the ATH coverage volumes in Figure 68 are shown in Figure 69.

6.1.9   Transformation from $\hat{x}\hat{y}\hat{z}$ to xyz

The cross-sections are derived in a Cartesian coordinate system ($\hat{x}\hat{y}\hat{z}$) such that the analysis plane is parallel to the $x - y$ plane in the general problem, the $\hat{z}$ axis is parallel to the z axis in the general problem, and the $\hat{x}$ axis points toward the Earth collinear with the projection of the satellite position vector into the $\hat{x} - \hat{y}$
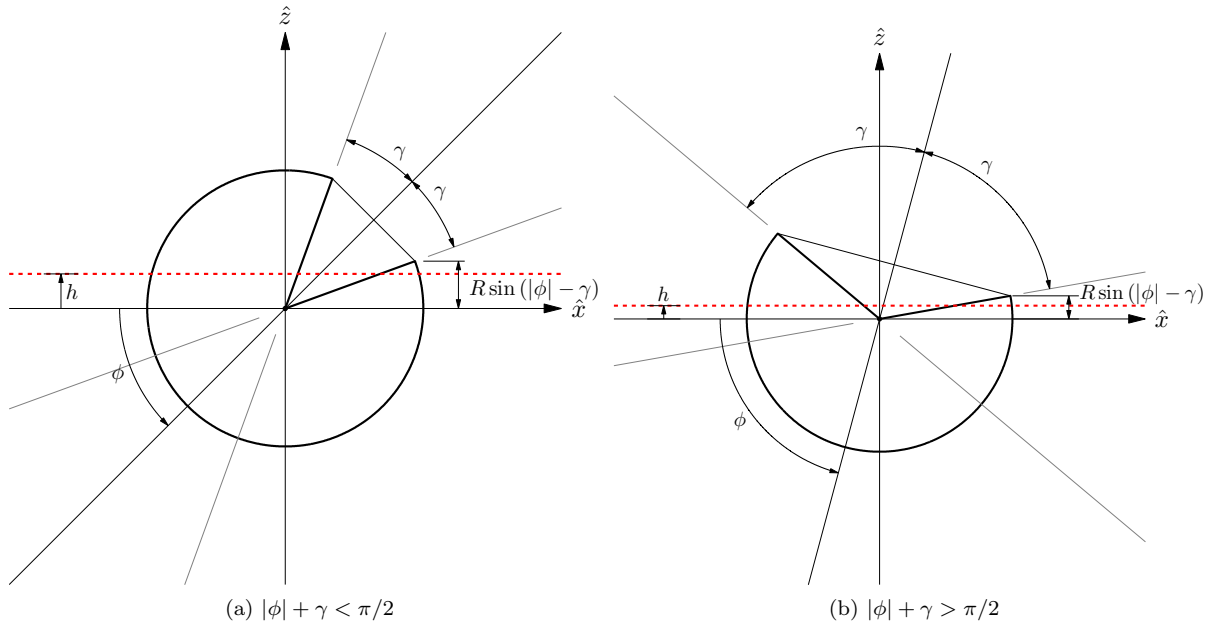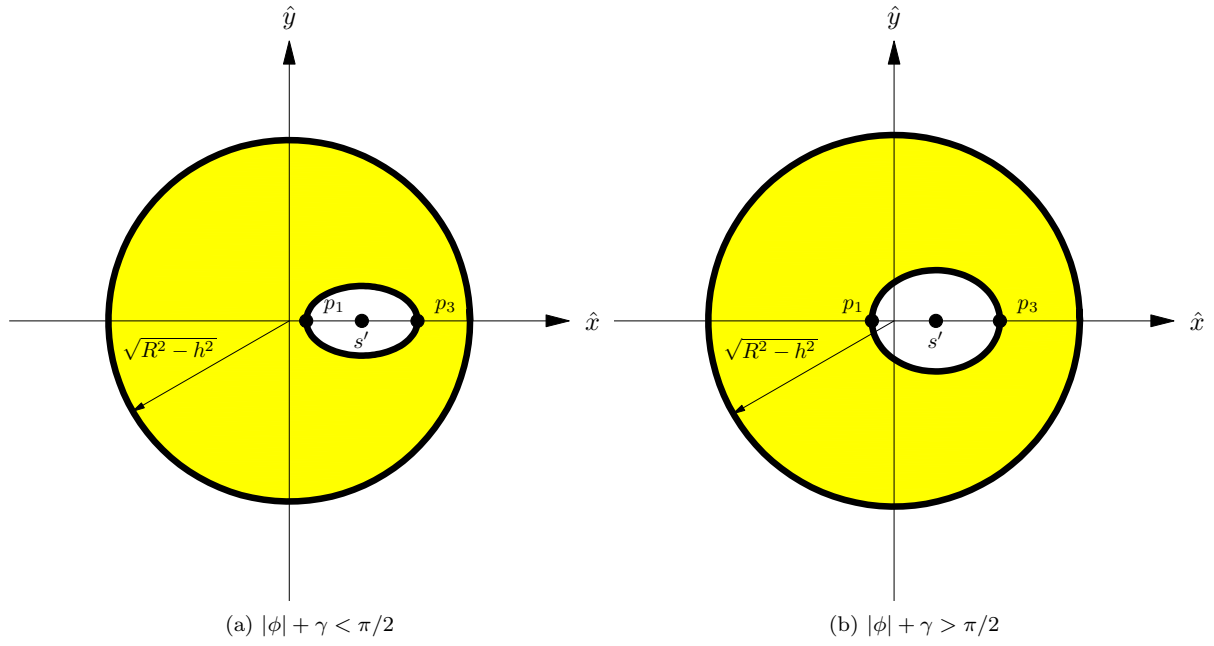
(a) $|\phi| + \gamma < \pi/2$

(b) $|\phi| + \gamma > \pi/2$

Figure 66: Case C2C

(a) $|\phi| + \gamma < \pi/2$

(b) $|\phi| + \gamma > \pi/2$

Figure 67: Case C2C

(a) $|\phi| + \gamma < \pi/2$

(b) $|\phi| + \gamma > \pi/2$

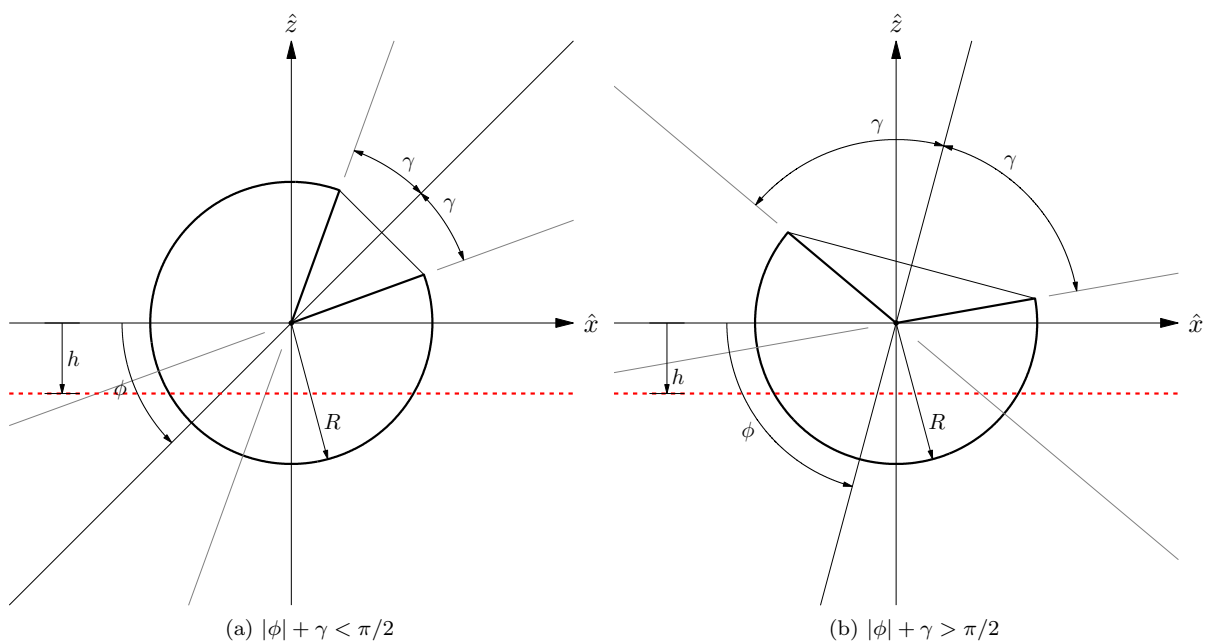Figure 68: Case C2D

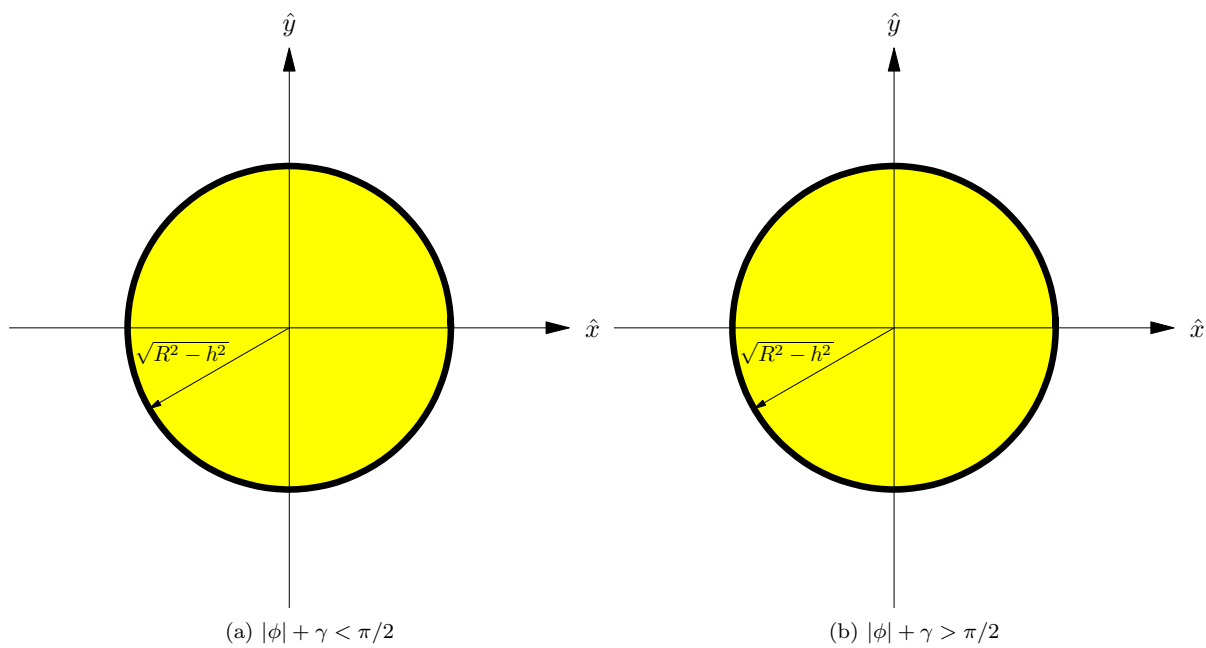(a) $|\phi| + \gamma < \pi/2$

(b) $|\phi| + \gamma > \pi/2$

Figure 69: Case C2D

plane. Transformation from the $\hat{x}\hat{y}\hat{z}$ frame to the xyz frame is accomplished by a single rotation about the $\hat{z}$ axis by $\theta + \pi$, where θ is the longitude of the satellite location in the xy plane (i.e. angle from the positive x axis), followed by a simple translation of coordinates from $(0, 0, 0)$ to $\mathbf{r}_{\text{sat}}$, where $\mathbf{r}_{\text{sat}}$ is the satellite position vector.

6.2 Target Cross-Section Generation

Target regions are typically geometrically less complex than an ATH sensor region which consists of a sphere and a missing cone region. Thus target region cross-sections are significantly more straightforward to compute in most cases.

6.2.1 Dual-Altitude Band Target Volume

The target region considered in the current study is a simple dual-altitude band target volume – a hollow sphere with an upper target radius of r_u, and a lower target radius of r_l, such that $r_t \leq r_l < r_u$. Figure 70 shows several cross-sections of a dual-altitude band target volume.

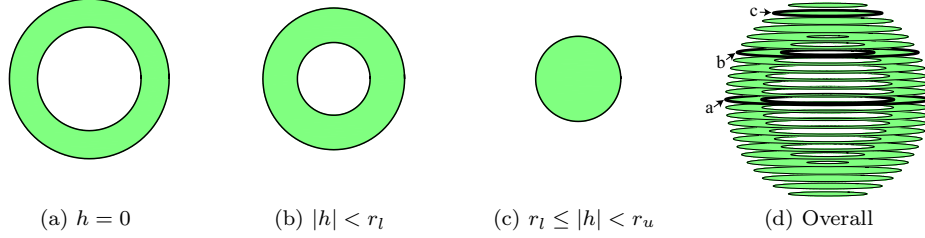(a) $h = 0$　　　(b) $|h| < r_l$　　　(c) $r_l \leq |h| < r_u$　　　(d) Overall

Figure 70: Offset cross-sections of a dual-altitude band target volume

Case A: $|h| < r_l$　The cutting plane intersects shells formed by both the outer and inner target radii, thus the cross-section is an annulus with an outer radius

$$r_{\mathrm{u}'} = \sqrt{r_u^2 - h^2}, \tag{104}$$

and an inner radius

$$r_{\mathrm{l}'} = \sqrt{r_l^2 - h^2}. \tag{105}$$

Case B: $r_l \leq |h| < r_u$　The cutting plane intersects only the shell formed by the outer target radius, thus the cross-section is a disk with radius

$$r_{\mathrm{u}'} = \sqrt{r_u^2 - h^2}. \tag{106}$$

Case C: $r_u \leq |h|$　The cutting plane does not intersect the target region at all, and thus no cross-section exists at this value of h.

6.2.2 Other Target Volume Types

Any target volume for which cross-section generation is straightforward may be implemented in an analysis with minimal effort. For instance, the dual-altitude band target volume case may be modified to consider lower and upper latitude limits. The resulting target volume would be toroidal in shape. Similarly, an Earth-fixed target volume may be defined incorporating latitude, longitude, and altitude bounds to describe a volume of space fixed above some geographic region.

7 Non-Planar Analysis Example Problems

The Examples presented in this section focus on analysis only at this time. The methods developed in the previous section are thus far only implemented in MATLAB, using the MATLAB/C version of the planar analysis algorithm. Thus, performance is insufficient for the optimization of any practical constellation in a reasonable amount of computer time executing on a single desktop computer. This issue will be alleviated in future work when the C/C++ implementation is parallelized and updated to analyze the volumetric case.

7.1 Example 7 – ATH Coverage by a Small Non-Coplanar Constellation

A constellation is considered with the properties shown in Table 13. The parameter h_{res} refers to the number of equally spaced offset planes in which cross-sectional coverage area is computed. These planes are distributed between on the interval $h \in [-(r_e + h_u), (r_e + h_u)]$.

Table 13: Example 7 – Parameters

Parameter	Description	Value
h_t	tangent height	100 km
h_l	lower target altitude	1000 km
h_u	upper target altitude	5000 km
k	number of orbital planes	3
n_i	satellites per plane	2
a_i	semi-major axis	10000 km
e_i	orbit eccentricity	0.25°
i_1	inclination of plane 1	0°
i_2	inclination of plane 2	45°
i_3	inclination of plane 3	90°
Ω_1	RAAN of plane 1	0°
Ω_2	RAAN of plane 2	120°
Ω_3	RAAN of plane 3	240°
ω_i	argument of periapsis of each orbit	0°
ΔM_i	spacing in mean anomaly	180°
M_{0_i}	mean anomaly of lead satellite at epoch	0°
R	omni-directional sensor range	5000 km
m	initial polygon resolution	50 PPC
h_{res}	offset plane resolution	100

The single and double ATH coverage provided by this constellation over 3 periods is shown in Figure 71. See accompanying video #4 for an animation of the constellation and coverage evolution.

The execution time of this analysis (at 500 time steps) in MATLAB is approximately 20 minutes in 64-bit Windows 7 on a 3.6GHz Intel Core i7 platform.

## 7.2 Example 8 – ATH Coverage by a Walker Star Constellation

The Walker Star constellation is a traditional satellite constellation for delivering BTH coverage. The Iridium satellite phone constellation is one operational example of a Walker Star. Idealized parameters for the Iridium constellation are shown in Table 14. The parameter h_{res} refers to the number of equally spaced offset planes in which cross-sectional coverage area is computed. These planes are distributed between on the interval $h \in [-(r_e + h_u), (r_e + h_u)]$.

The single and double ATH coverage provided by this constellation over 20 minutes is shown in Figure 72. See accompanying video #5 for an animation of the constellation and coverage evolution.

The origin of the Walker Star constellation is in the 'streets of coverage' approach, where satellite planes are spaced and phased such that continuous single BTH coverage is available at the equator where longitudinal
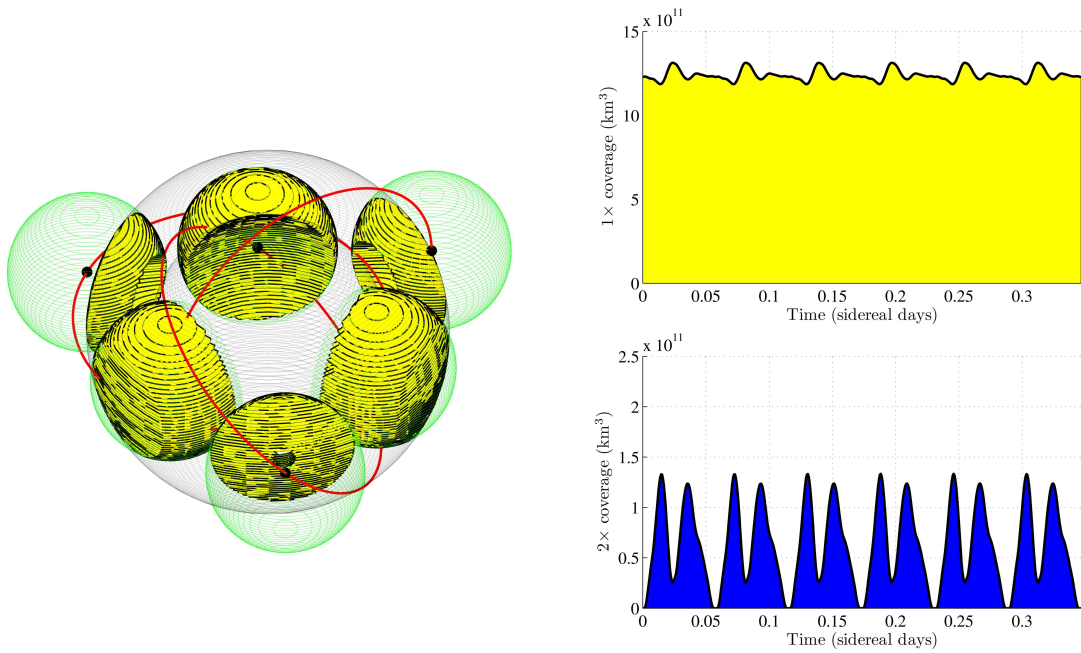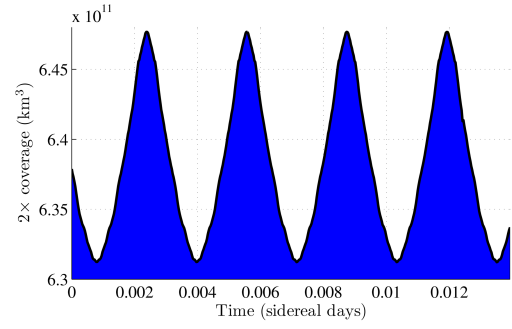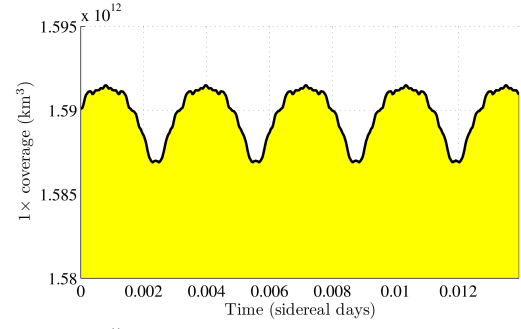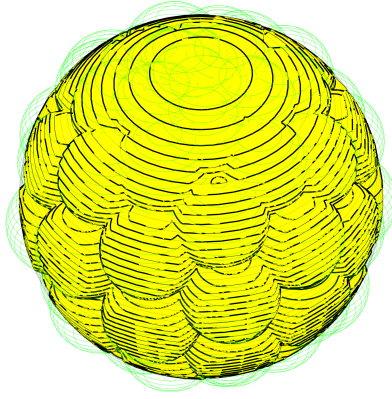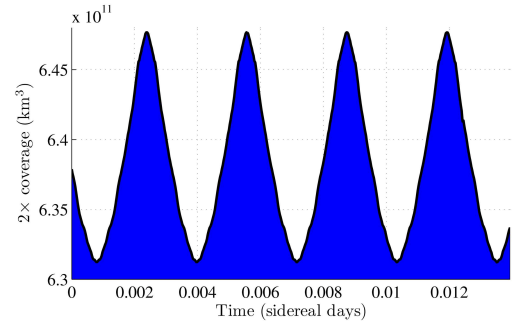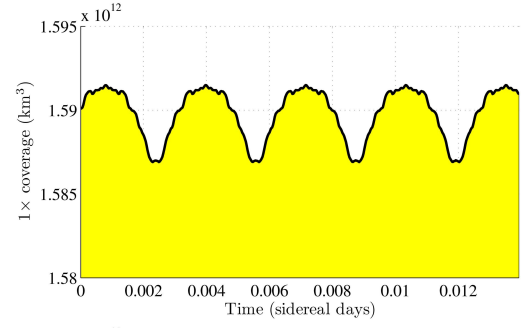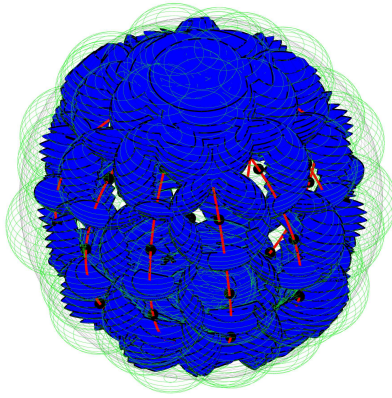
(a) 1× Coverage
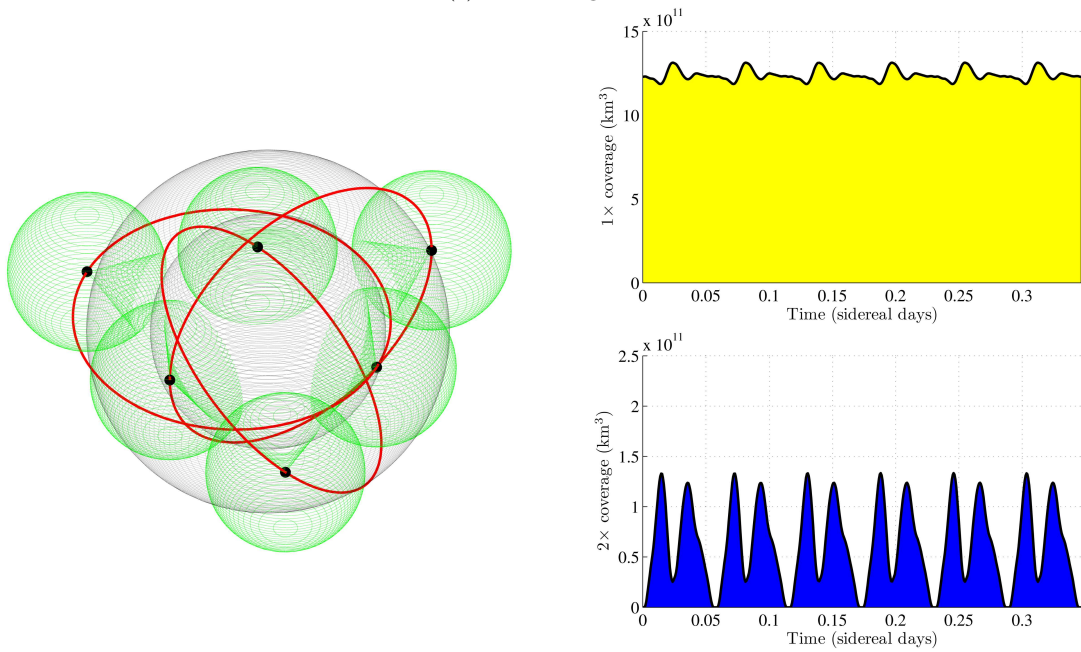
(b) 2× Coverage

Figure 71: Example 7 – Single and Double ATH Coverage (see accompanying video #4)

(a) 1× Coverage

(b) 2× Coverage

Figure 72: Example 8 – Single and Double ATH Coverage (see accompanying video #5)

Table 14: Example 8 – Parameters

Parameter	Description	Value
h_t	tangent height	100 km
h_l	lower target altitude	200 km
h_u	upper target altitude	2500 km
k	number of orbital planes	6
n_i	satellites per plane	11
h_i	satellite altitude	781 km
e_i	orbit eccentricity	0°
i_i	plane inclination	86.4°
Ω_1	RAAN of plane 1	0°
Ω_2	RAAN of plane 2	31.6°
Ω_3	RAAN of plane 3	63.2°
Ω_4	RAAN of plane 4	94.8°
Ω_5	RAAN of plane 5	126.4°
Ω_6	RAAN of plane 6	158°
ΔM_i	spacing in mean anomaly	32.73°
PO	phase offset b/w adjacent planes	18°
R	omni-directional sensor range	2500 km
m	initial polygon resolution	50 PPC
h_{res}	offset plane resolution	100

spacing of satellites is at a maximum. From this example it is clear to see that a volumetric analog of the 'streets of coverage' approach may be used to design constellations for ATH coverage under certain conditions. The definition of a 'street' would necessarily be amended to a three-dimensional analog of a 'street,' such that coverage throughout the altitude range is ensured at the equator in the final solution.

The execution time of this analysis (at 500 time steps) in MATLAB is approximately 60 minutes in 64-bit Windows 7 on a 3.6GHz Intel Core i7 platform.

7.3 Example 9 – ATH Coverage by a Walker Delta Constellation

The Walker Delta constellation is a traditional satellite constellation for delivering BTH coverage. The GlobalStar satellite phone constellation is one operational example of a Walker Delta. Idealized parameters for the GlobalStar constellation are shown in Table 15. The parameter h_{res} refers to the number of equally spaced offset planes in which cross-sectional coverage area is computed. These planes are distributed between on the interval $h \in [-(r_e + h_u), (r_e + h_u)]$.
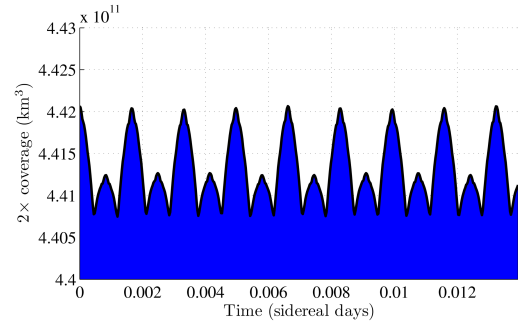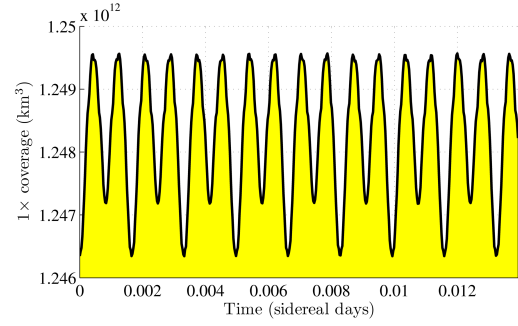
The single and double ATH coverage provided by this constellation over 20 minutes is shown in Figure 73. See accompanying video #6 for an animation of the constellation and coverage evolution.

Just as in the BTH case, this low altitude Walker Delta constellation provides no ATH coverage at the poles. Thus, a Walker Delta may only be suitable for ATH coverage of a target region limited to some latitude range centered at the equator.

The execution time of this analysis (at 500 time steps) in MATLAB is approximately 45 minutes in 64-bit Windows 7 on a 3.6GHz Intel Core i7 platform.
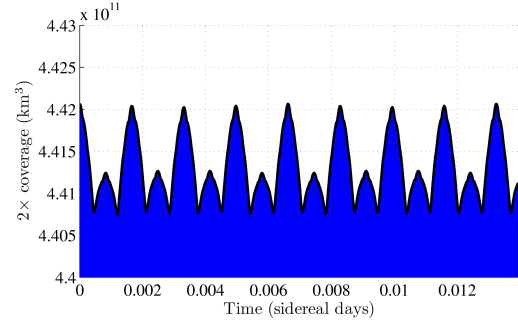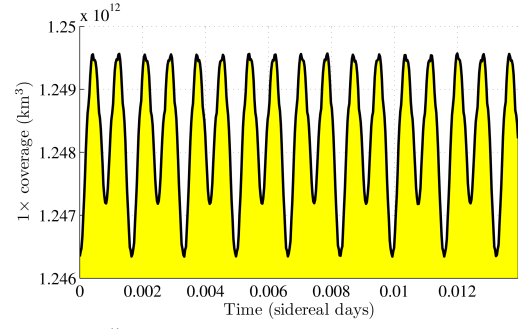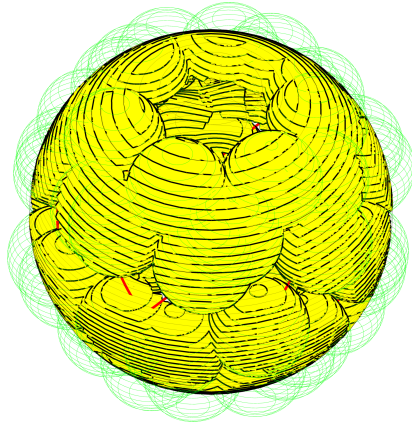
(a) 1× Coverage
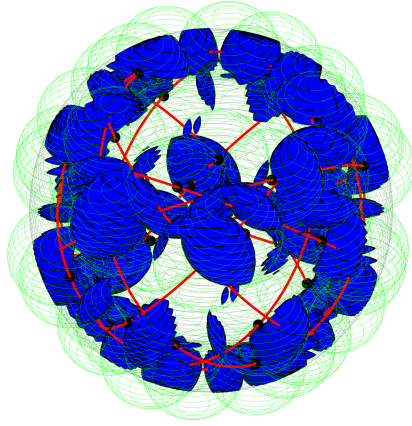
(b) 2× Coverage

Figure 73: Example 9 – Single and Double ATH Coverage (see accompanying video #6)

Table 15: Example 9 – Parameters

Parameter	Description	Value
h_t	tangent height	100 km
h_l	lower target altitude	200 km
h_u	upper target altitude	2500 km
k	number of orbital planes	8
n_i	satellites per plane	6
h_i	satellite altitude	1414 km
e_i	orbit eccentricity	0°
i_i	plane inclination	52.0°
Ω_1	RAAN of plane 1	0°
Ω_2	RAAN of plane 2	45°
Ω_3	RAAN of plane 3	90°
Ω_4	RAAN of plane 4	135°
Ω_5	RAAN of plane 5	180°
Ω_6	RAAN of plane 6	225°
Ω_7	RAAN of plane 7	270°
Ω_8	RAAN of plane 8	315°
ΔM_i	spacing in mean anomaly	60°
PO	phase offset b/w adjacent planes	7.5°
R	omni-directional sensor range	2500 km
m	initial polygon resolution	50 PPC
h_{res}	offset plane resolution	100

8 Conclusions

During the course of this effort, optimal constellation design for above-the-horizon coverage was explored. Initially, the analysis focused only on planar constellations. This facilitated some analytical studies that served as a basis for validation of a greater numerical process, later extended to address a simplified version of the three-dimensional problem. The work yielded two significant developments. First, a generalized numerical algorithm was designed, tested, and validated that can be used to address the design of planar constellations for optimal above-the-horizon coverage. The algorithm allows for the consideration of non-omnidirectional sensors and arbitrary sensor pointing. The product of this work served as a stepping stone to the second development, the extension to the non-coplanar (i.e. three-dimensional) case, where the satellites in the constellation exist in differing elliptical three-dimensional orbits. This latest aspect of the development was restricted to omni-directional sensors, for simplicity, but the overall process of computing the cost metric in the three-dimensional case was otherwise successfully demonstrated.

From a software development perspective, both the two- and three-dimensional cases were developed in Matlab, though the two-dimensional case also explored C/C++ as a means of increasing computational efficiency. Future studies may consider parallelization, via GPU's, of the overall cost metric calculation, which should offer significant performance improvements in any optimization process that depends on this cost metric. The nature of the problem lends itself well to parallel computing. With a high-performance computing implementation, various NLP and MINLP solvers may be wrapped around the new numerical volumetric ATH coverage model. Optimal constellation design may then be approached in a volumetric sense as readily as it was addressed in the planar case during the initial years of this award.

References

[1] Biria, A. D., *Analytical Approach to the Design of Optimal Satellite Constellations for Space-Based Space Situational Awareness*, Master's thesis, The University of Texas at Austin, December 2011, Advisor: Dr. Belinda Marchand.

[2] Biria, A. and Marchand, B., "Constellation Design for Space-Based Situational Awareness Applications: An Analytical Approach," *AAS/AIAA Astrodynamics Specialists Conference*, Girdwood, AK, August 2011, Paper No. AAS11-538.

[3] Takano, A. T., *Numerical Analysis and Design of Satellite Constellations for Above the Horizon Coverage*, Master's thesis, The University of Texas at Austin, December 2010, Advisor: Dr. Belinda Marchand.

[4] Takano, A. T. and Marchand, B. G., "Optimal Constellation Design for Space Based Situational Awareness Applications," *AIAA/AAS Astrodynamics Specialists Conference*, Girdwood, AK, August 2011, Paper No. AAS11-543.

[5] Marchand, B. G. and Kobel, C., "Above the Horizon Satellite Coverage with Dual-Altitude Band Constraints," *The Journal of Spacecraft and Rockets*, Vol. 46, No. 4, 2009, pp. 845–857.

[6] Beyer, W. H., editor, *CRC Standard Mathematical Tables*, CRC Press, 28th ed., 1987, pp. 123–124.

[7] Murta, A., "General Polygon Clipping Library," `http://www.cs.man.ac.uk/~toby/alan/software/`.

[8] The MathWorks, *Fmincon*, `http://www.mathworks.com/help/toolbox/optim/ug/fmincon.html`.

[9] Wertz, J. R. and Larson, W. J., editors, *Space Mission Analysis and Design*, chap. 20, Microcosm Press, 3rd ed., 2007.

[10] Gordon, K. J., "The Computation of Satellite Constellation Range Characteristics," *AIAA/AAS Astrodynamics Conference*, Scottsdale, AZ, August 1994, Paper No. AIAA-94-3704-CP.

[11] Powell, M., "A fast algorithm for nonlinearly constrained optimization calculations," *Numerical Analysis*, edited by G. Watson, Vol. 630 of *Lecture Notes in Mathematics*, Springer Berlin / Heidelberg, 1978, pp. 144–157.

[12] SciCepts Engineering, *ImageDIG*, `http://www.imagedig.com`.

[13] Kuhn, H. W. and Tucker, A. W., "Nonlinear programming," *Proceedings of the 2nd Berkeley Symposium*, University of California Press, 1951, pp. 481–492.

[14] Martin, D. H., "The essence of invexity," *Journal of Optimization Theory and Applications*, Vol. 47, 1985, pp. 65–76.

[15] Schlueter, M., Rckmann, J. J., and Gerdts, M., "Mixed Integer Distributed Ant Colony Optimization," `http://www.midaco-solver.com/index.html`.

[16] Schlueter, M., Egea, J. A., and Banga, J. R., "Extended ant colony optimization for non-convex mixed integer nonlinear programming," *Computers and Operations Research*, Vol. 36, No. 7, 2009, pp. 2217–2229.